UNIVERSITY OF CALIFORNIA,
IRVINE

Magneto-optical studies of novel condensed matter phases with Sagnac interferometry

DISSERTATION

submitted in partial satisfaction of the requirements
for the degree of

DOCTOR OF PHILOSOPHY

in Physics

by

Jingyuan Wang

Dissertation Committee:
Professor Jing Xia, Chair
Assistant Professor Javier Sanchez-Yamagishi
Assistant Professor Luis Jauregui

2023

TABLE OF CONTENTS

LIST OF FIGURES

ACKNOWLEDGEMENTS

First, I would like to thank my advisor Prof. Jing Xia for allowing me to work in his lab and teaching me how to conduct research. I also wanted to thank Prof. Javier Sanchez-Yamagishi and Prof. Luis Jauregui for providing useful career guidance, I will not be able to find an ideal postdoc position without their help. It is also a great pleasure to attend the joint weekly journal club of JDSY lab and Jauregui lab, I always feel refreshed and motivated to hear about interesting topics even though it is sometimes not directly related to my research, I will definitely miss this when I leave UCI.

Then I want to thank the Xlab members I worked with, Camron Farhang, Brian Casas, Alex Stern and Laura Yu, thank you for helping me with the lab work. Thank members of JDSY lab and Jauregui lab, Jinyu Liu, Andrew Barabas, Ian Sequeira, TJ and Drew for lending me equipment and helpful discussions. Thank Jiang Yao, Siyu Chen, and Likun Wang from Ho's lab for all kinds of help. I should also express my gratitude to the collaborators, thank Prof. Maeno and Prof. Yonezawa at Kyoto University for providing the nice Sr_2RuO_4 crystals and teaching me about this fascinating superconductor Prof. Maeno discovered 30 years ago; thank Prof. Xiaofeng Jin at Fudan University for the $NiBi_3$ crystals and Prof. Stephen Wilson for the CsV_3Sb_5 crystals. I would also like to thank Su Kong Chong and Peng Zhang for the nice collaboration on the CBST project.

Finally, thank my friends Hasitha Eranda, Tao Wang, Yalun Zhang and Hongzhen Chen for the chatting that are really entertaining and relaxing. Thank Laisi Chen for being with me through this longest and hardest journey of my life. Thank my parents for their unconditional love and support, I feel lucky to be your son.

VITA

Jingyuan Wang

2014-2016	Undergraduate Student Researcher, Nanjing University
2015	Undergraduate Student Researcher, UWA-China Research Training Program, University of Western Australia
2016	B.S. in Science, Nanjing University
2016-2017	Teaching Assistant, Department of Physics and Astronomy, University of California, Irvine
2017-2023	Research Assistant, Department of Physics and Astronomy, University of California, Irvine
2023	Ph.D. in Physics, University of California, Irvine,

ABSTRACT OF THE DISSERTATION

Magneto-optical studies of novel condensed matter phases with Sagnac interferometry

By

Jingyuan Wang

Doctor of Philosophy in Physics

University of California, Irvine, 2023

Jing Xia, Chair

According to Landau's theory of phase transition, a second-order phase transition is accompanied by spontaneous symmetry breaking characterized by an order parameter. This thesis focuses on using magneto-optical Kerr effect (MOKE) to characterize the time-reversal symmetry (TRS) breaking in novel phases of matters including unconventional superconductivity, charge density wave and quantum magnetism. Chapter 1 gives a brief theoretical introduction of MOKE, followed by description of Sagnac interferometry in Chapter 2. The rest of the thesis will focus on three projects involving high resolution MOKE measurements.

Bi/Ni bilayer is a unique system where unconventional superconductivity that breaks TRS arises at the interface between two non-superconducting elements. However, the origin of the superconductivity is under debate, the formation of superconducting $NiBi_3$ impurity has been observed in samples grown by certain methods and is believed to cause the observed TRS

breaking superconductivity. A test for the TRS breaking superconductivity in NiBi3 single crystal with high resolution MOKE measurements is presented in Chapter 3.

Sr_2RuO_4 is an unconventional superconductor with TRS breaking and unknown pairing symmetry, despite having been heavily studied for almost three decades. Recently studies on Sr_2RuO_4 under uniaxial strain provided new experimental evidence, including a split of the T_c and onset temperature of TRS breaking phase under strain observed in μSR measurements. A study to test such strain-induced double transition scenario by combining MOKE measurements with application of uniaxial strain is presented in Chapter 4.

Recently discovered Kagome metal CsV_3Sb_5 holds an unconventional charge density wave order below 94K and a superconducting ground state below 2.5K, providing an ideal playground to study intertwined orders. Evidence for TRS breaking has been found in its charge density wave phase by various experimental probes, which are believed to have connections to the long-sought loop current phase first proposed for cuprate superconductors. A comprehensive MOKE study on CsV_3Sb_5 to test the TRS breaking charge density wave phase is presented in Chapter 5.

Chapter 1

Magneto-optic Kerr effect

1.1 Introduction

Magneto-optic (MO) effects arise from the interaction between photon and electron spin through spin-orbit coupling, accompanied by change in the polarization state of the light. MO effects provide powerful tools for investigating the magnetic and electronic properties of materials, for their high sensitivity and non-destructive nature. The MO effect studied in this thesis is magneto-optic Kerr effect (MOKE), it occurs when linearly polarized light reflects off a magnetized medium, transforming the light into elliptical polarization with a rotation of its polarization axis. The transmission version of Kerr effect is Faraday effect. A schematic of Kerr effect and Faraday effect is shown in Fig. 1.1.

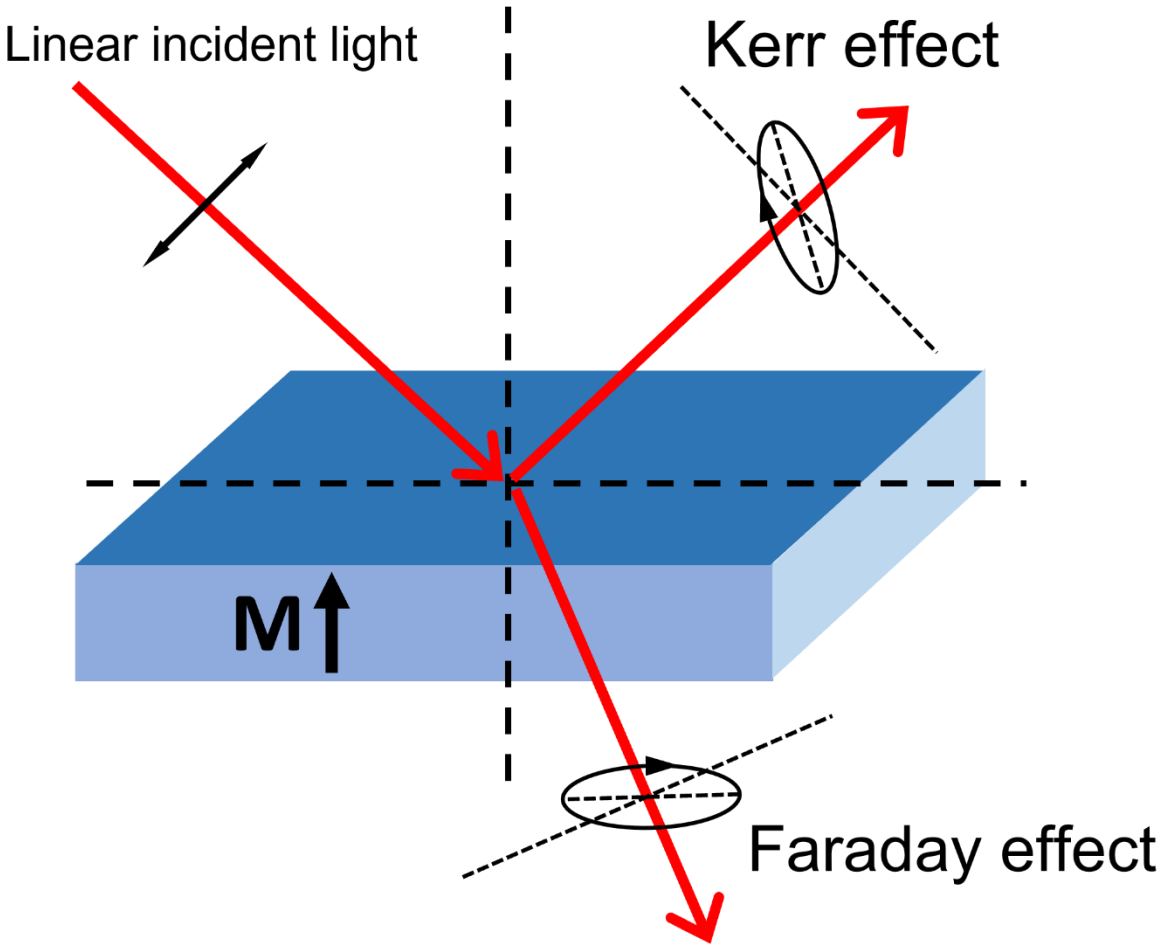

Fig. 1.1: Schematic showing the magneto-optic Kerr effect and Faraday effect.

The MOKE is due to the material's different response to left- and right-circular polarization of light. The two circularly polarized lights will experience different complex refractive index when interacting with the magnetic material and acquire different phase and absorption. A linearly polarized light is a superposition of two circularly polarized light with opposite chirality and equal intensity, when these two circular polarized lights interact with the sample, they acquire different phase shift and intensity and give an elliptically polarized light with polarization rotation when they are recombined.

There are three types of Kerr effect that are classified based on the relative angle between the plane of incidence and magnetic moment in the material. As shown in Fig. 1.2, when the magnetic moment is perpendicular to the sample surface, it couples to the electric field component of the incident light that is parallel to the sample surface and gives the polar Kerr effect. When the moment is parallel to the sample surface and in the plane of incidence, the effect is longitudinal; when the moment is perpendicular to the plane of incidence, a transverse Kerr effect will occur. In this thesis the polar Kerr effect at normal incidence is measured, as shown in Fig. 1.3. In principle all three types of Kerr effect can be measured, with different geometry of the optics and properly chosen polarization modes to maximize the sensitivity of the measurement [1].

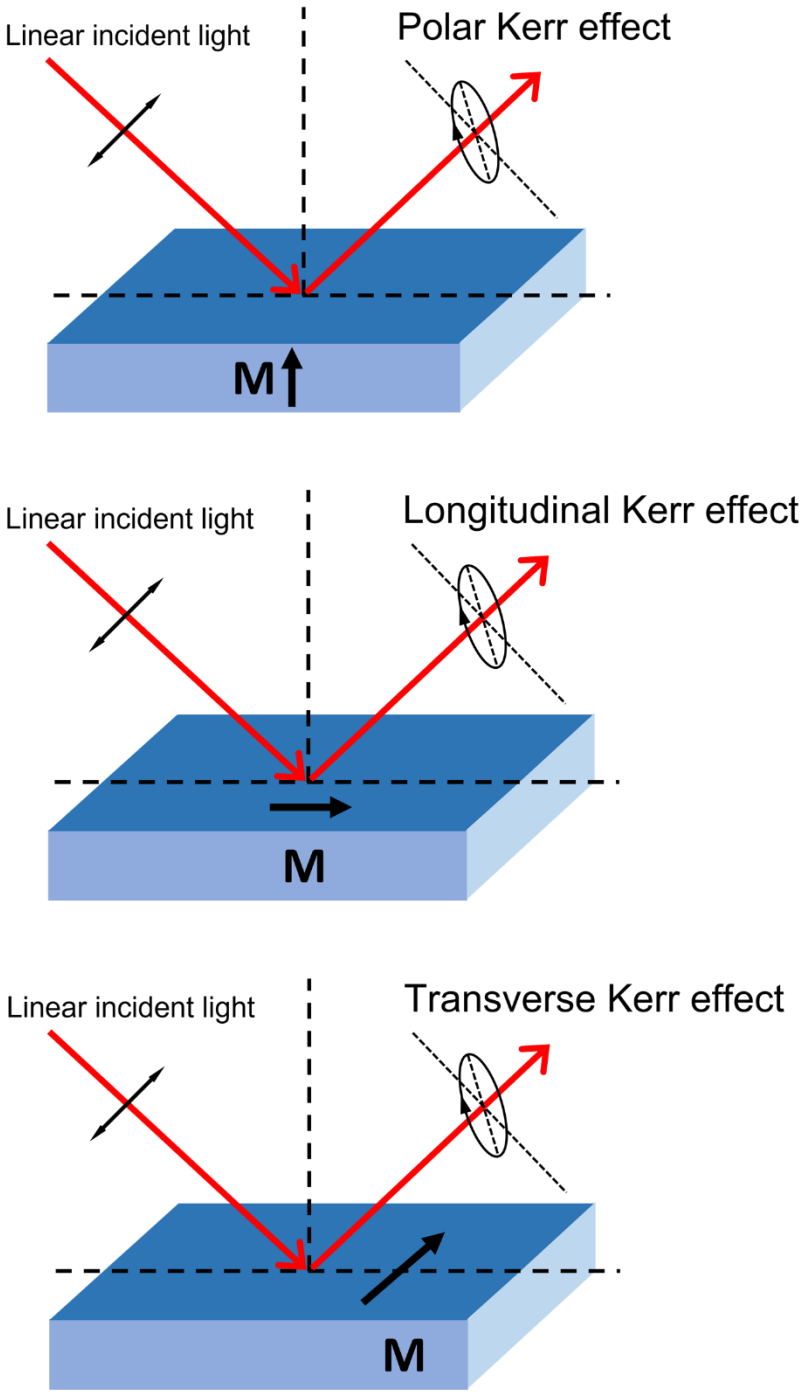

Fig. 1.2: Schematics for different types of Kerr effect. Top: polar Kerr effect. Middle: Longitudinal Kerr effect. Bottom: Transverse Kerr effect.

Consider the case of magnetic moment being along the z axis, the origin of the Kerr effect is the antisymmetric off diagonal components $-\varepsilon_{xy} = \varepsilon_{yx}$ of the dielectric tensor, which only happens when time-reversal symmetry (TRS) is broken in the system. Higher order effects such as gyrotropy can also induce a finite Kerr rotation in a TRS symmetric system with inversion symmetry breaking, but it is beyond the scope of this thesis so I will not talk about it but rather focus on the first order Kerr effect related to TRS breaking (TRSB). The dielectric tensor for a TRSB material with no linear birefringence can be written as:

$$\varepsilon_{ij} = \begin{bmatrix} \varepsilon_{xx} & \varepsilon_{xy} & 0 \\ -\varepsilon_{xy} & \varepsilon_{xx} & 0 \\ 0 & 0 & \varepsilon_{zz} \end{bmatrix}$$

Plug this into Fresnel's equation:

$$\varepsilon_{ij} E_j = n^2 (E_i - \delta_{iz} E_z)$$

Where $\vec{E} = (E_x, E_y, 0)$ at normal incidence, and n is the complex refractive index, one can find solution for n:

$$n_{\pm}{}^2 = \varepsilon_{xx} \pm i\varepsilon_{xy}$$

And the corresponding eigen modes of light are,

$$E_y = \pm i E_x$$

Which represents circular polarization. The Kerr rotation θ_k is half of the phase difference $\Delta\varphi$ induced between the two circular polarizations, which can be calculated using the refractive index for the two types of circularly polarized light.

Linear birefringence also rotates polarization of light, in the case where the principal axis is in the sample surface and the material is purely birefringent, as shown in Fig. 1.3, the dielectric constant is in the form:

$$\varepsilon_{ij} = \begin{bmatrix} \varepsilon_{xx} & 0 & 0 \\ 0 & \varepsilon_{yy} & 0 \\ 0 & 0 & \varepsilon_{zz} \end{bmatrix}$$

Doing the same calculations, one would get:

$$n_x{}^2 = \sqrt{\varepsilon_{xx}},\ n_y{}^2 = \sqrt{\varepsilon_{yy}}$$

And the eigen modes of light are linear polarization:

$$E_y = 0, E_x = 0$$

When the principal axis is not in the surface plane, there will be off-diagonal element in the dielectric tensor, but it is symmetric, $\varepsilon_{xy} = \varepsilon_{yx}$. We can always transform the dielectric tensor into a diagonal one by choosing a different coordinate system and the situation is reduced to the one discussion here.

We shall see in the next chapter that this polarization rotation will not be picked up by our setup, because the refractive index in the circular basis is the same for the two polarizations:

$$n_+ = n_-$$

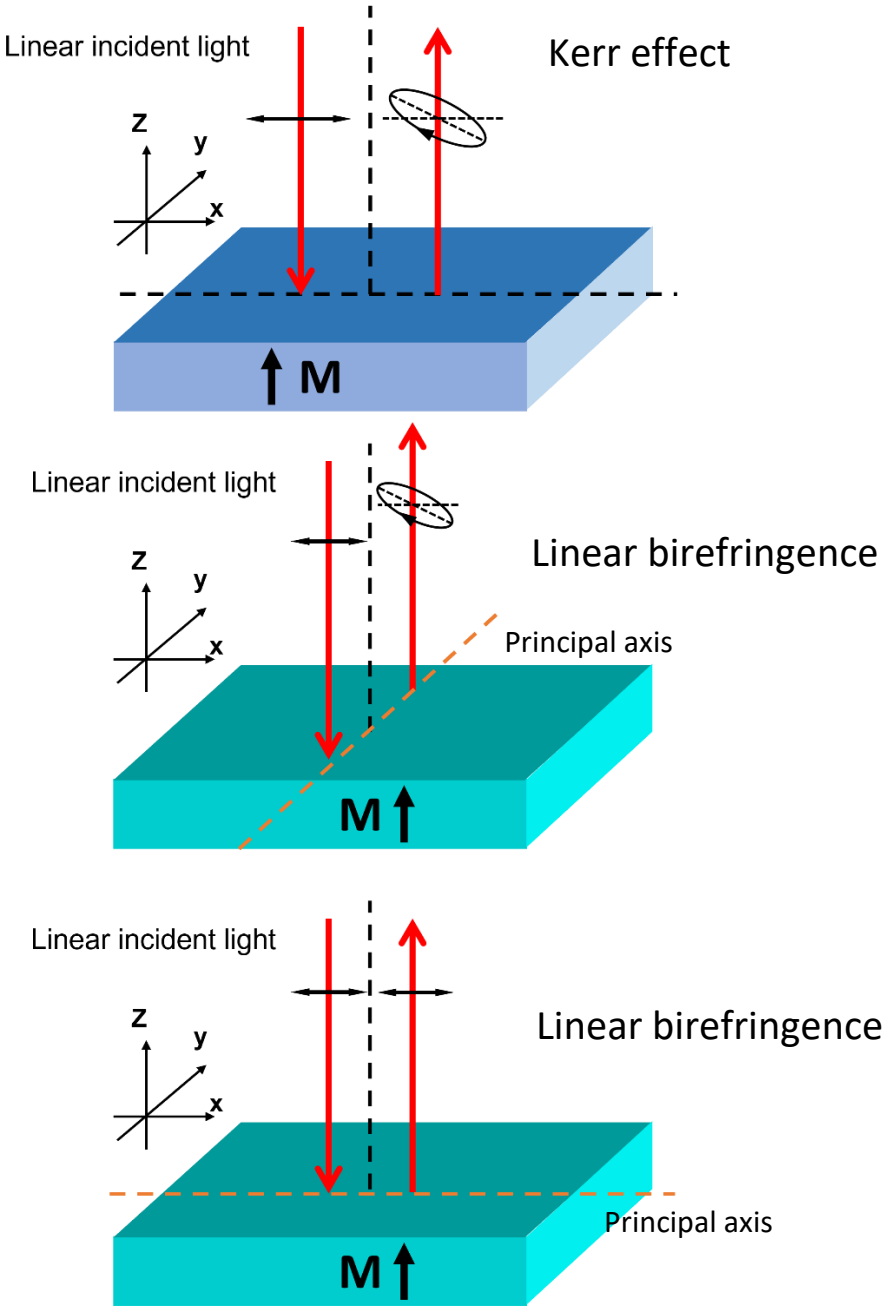

Fig. 1.3: Schematics of Kerr effect and linear birefringence at normal incidence. Top: Polar Kerr effect, polarization rotation is isotropic despite of direction of incidence polarization. Middle: Linear birefringence, an anisotropic polarization rotation is induced when incident polarization is not along principal axis. Bottom: Linear birefringence, no polarization rotation is caused when incident light is polarized along the principal axis.

1.2 Microscopic theory of Kerr effect

1.2.1 Classical treatment

We have now established that the Kerr rotation comes from the anti-symmetric off diagonal term in the dielectric tensor, in this section I will review shortly the microscopic origin of such off diagonal terms.

In the classical treatment of a material in external field magnetic field H along the z axis, the electrons are in harmonic bond states subject to an oscillating electric field along x axis $E_x = Ee^{-i\omega t}$ provided by the incident light. The equation of motion of the electron would be:

$$m\ddot{\boldsymbol{r}} + \gamma m\dot{\boldsymbol{r}} + m{\omega_0}^2\boldsymbol{r} = -eEe^{-i\omega t}\hat{\boldsymbol{x}} - m\omega_c\dot{\boldsymbol{r}} \times \hat{\boldsymbol{z}}$$

Where m is mass of electron, ω_0 is the frequency of electron's bound state, ω_c is the cyclotron frequency. Once the $\boldsymbol{r}(t)$ is solved, the conductivity matrix can be calculated using the Ohms law:

$$\boldsymbol{J} = -ne\dot{\boldsymbol{r}} = \sigma\boldsymbol{E}$$

A non-zero off diagonal term is caused by the last term in the equation of motion which couples the motions in the x and y directions. The dielectric tensor can be calculated using conductivity matrix by the relation:

$$\varepsilon = 1 - \frac{4\pi i}{\omega}\sigma$$

And the off-diagonal element would be:

$$\varepsilon_{xy} = -\frac{4\pi ne^2}{m}\frac{i\omega\omega_c}{({\omega_0}^2 - \omega^2 - i\omega\gamma)^2 - \omega^2{\omega_c}^2}$$

This treatment roughly agrees with the Faraday and Kerr effect observed in diamagnetic materials in an external magnetic field. However, it cannot explain the huge Faraday and Kerr effects observed in ferromagnetic materials, where the classical treatment requires an internal Weiss field in the order of 100-1000 T to generate such an effect [2]. A quantum mechanical theory is needed to explain the effects of ferromagnets.

1.2.2 Quantum mechanical treatment for ferromagnets

Weiss field in ferromagnets is a hypothetical field proposed to explain the interaction between spins, now we know that it is Heisenberg's exchange interaction that aligns the spins in a ferromagnet, and Weiss field does not exist. Exchange interaction exists in the spin channel and does not couple to the orbital motion of electrons, which determines the material's response to light, thus exchange interaction cannot be used to explain the anomalous Kerr effect in ferromagnetic systems.

The key to connect magnetic moment of an electron to its orbital motion is spin-orbit coupling, which results from the coupling of electron's magnetic moment to the magnetic field electron feels as it moves in an electric field. When a spin-orbit coupling term $\frac{1}{2m^2c^2}(\nabla V(\boldsymbol{r}) \times \boldsymbol{p}) \cdot \boldsymbol{s}$ is added to the Hamiltonian [3], the effect of ferromagnetism naturally arises in the dielectric function. In a nonmagnetic material in zero external field, although the spin-orbit coupled term still exists in the Hamiltonian, the net effect is zero because spin-up and spin-down states are equally occupied. In a ferromagnet or diamagnet in external field, the spin-orbit coupling effect manifests itself due to the uneven population of electron spins. Further calculations are made with the modification of wavefunction due to spin-orbit coupling included and give correct order of magnitude in the difference between dielectric constant of two circular polarizations [4,5].

Chapter 2

Sagnac interferometer

2.1 Introduction

Sagnac interferometer is invented by French physicist Georges Sagnac, as a tool to test the existence of aether. A schematic of a Sagnac typical Sagnac interferometer is shown in Fig. 2.1. The key feature of a Sagnac interferometer is the loop, where two counter-propagating light beams travel along the same path but in opposite directions. These two light beams form a time-reversal counterpart when their polarization states are properly chosen and can be used to test for time reversal symmetry (TRS) breaking effects.

The Sagnac interferometer itself is reciprocal, meaning that when direction of light propagation is reversed, no change will be introduced to the system. However, when a non-reciprocal effect is introduced into the Sagnac loop, a non-reciprocal phase shift will be induced between the two counter propagating beams and an interference pattern can be observed at the detector. There are a few major sources of non-reciprocal phase shifts:

1. Time-dependent perturbation located not at the middle of the Sagnac loop. Obviously because the time for the two light beams to arrive at the perturbation point is different, the time-dependent perturbation they feel is different.
2. The Sagnac effect. A phase shift is induced between the two light beams when the Sagnac loop is rotating, because the light path for the two beams to travel is different due to spinning. The phase shift can be estimated by equation:

$$\Delta\varphi = \frac{8\pi}{\lambda c}\boldsymbol{\omega} \cdot \boldsymbol{A}$$

Where λ is the wavelength of light, $\boldsymbol{\omega}$ is the angular velocity and $\boldsymbol{A}$ is the area of the loop. For a sensitive Sagnac interferometer, earth rotation will introduce significant background signal due to the non-zero loop area $\boldsymbol{A}$.

3. Magneto-optic effects. MO effects such as Faraday effect is non-reciprocal, unlike for birefringent materials where the polarization rotation can be cancelled by sending the light back through the material again, when a light beam propagates through a magnetic material twice along opposite directions, the Faraday rotation is not zero but doubled. The magnetic moment in the sample breaks time reversal symmetry and thus the direction of Faraday rotation only depends on the direction of magnetic moment but not the direction of light propagation. For the Kerr effect, the non-reciprocal phase shift on the circular basis is twice of the Kerr rotation.

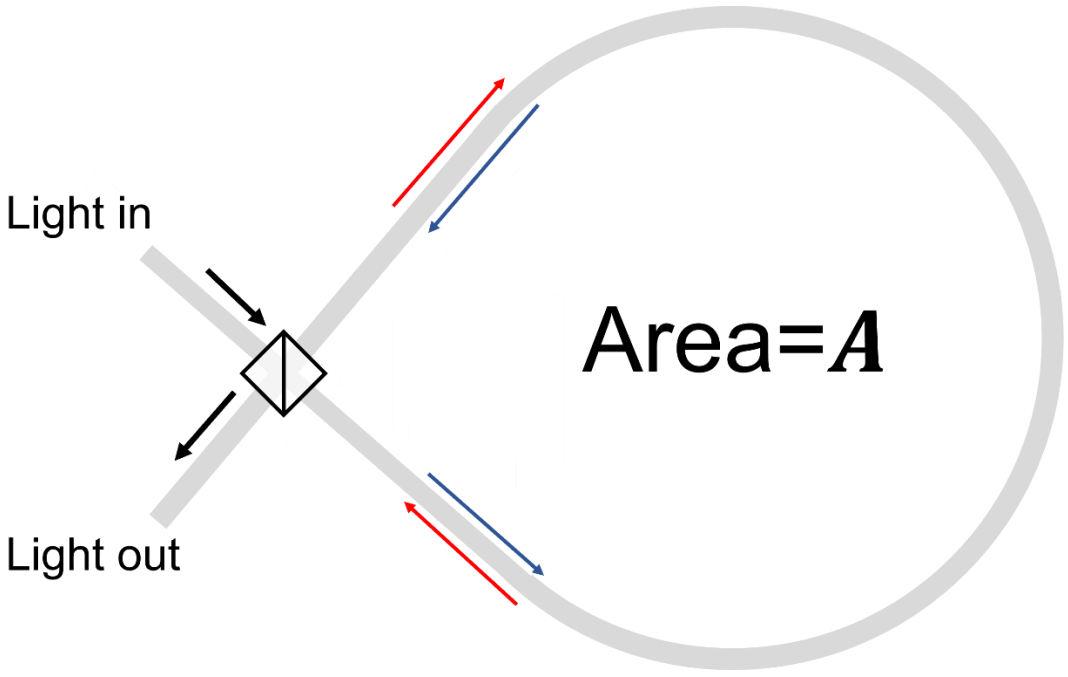

Fig. 2.1: Schematic of a Sagnac interferometer with loop area $\boldsymbol{A}$

2.2 Loopless Sagnac interferometer

The reciprocal nature of Sagnac interferometer makes it an ideal tool to study MO effects, its selective sensitivity towards non-reciprocal effects and the natural rejection of reciprocal effects allows a distinction between the source of polarization rotation. In our lab a loopless Sagnac interferometer is constructed to conduct high precision MOKE measurements, this design was first made in Kapitulnik lab at Stanford University by Jing Xia [6].

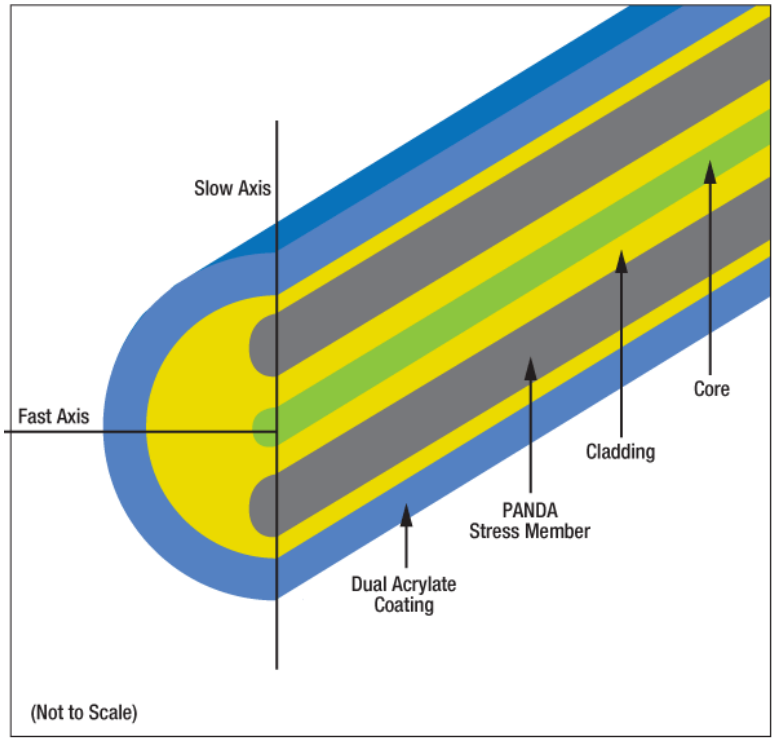

Fig 2.2: Schematic of Thorlabs polarization maintaining fiber,

https://www.thorlabs.com/newgrouppage9.cfm?objectgroup_id=1596

In the former version of the Sagnac interferometer [7,8], the Sagnac loop is kept, and two light beams propagate in the loop fiber in opposite directions. Such design gives a sensitivity of 3 μrad but the earth rotation prevents the further improvement of the sensitivity. To overcome this, the

Sagnac loop is collapsed into a single polarization maintaining (PM) fiber and zero loop area is achieved. Shown in Fig. 2.2, the PM fiber has a core with strong induced birefringence, which allows two orthogonal linearly polarized light propagating along the fast and slow axis of the core independently and maintain their polarization state. By replacing the Sagnac loop fiber with a single PM fiber, a loopless Sagnac interferometer is constructed, as shown in Fig. 2.3. In this loopless Sagnac interferometer, light from a 1550-nm broadband source is polarized and guided into a PM fiber, the polarization of light is then rotated by 45˚ by a half-wave plate (HWP) before it enters an electro-optic modulator (EOM) operating at frequency ω_m. The EOM splits the light into two orthogonal beams with linear polarization and adds time-dependent phase shifts to both beams. After passing the EOM, the two light beams are launched into the fast and slow axis, respectively, of a 10-meter-long PM fiber that is fed into a Quantum Design PPMS cryostat and guided to the optics mounted on a piezo bimorph scanner with submicron step size in both horizontal directions. The two beams are focused onto the sample surface by an aspheric lens after existing PM fiber and converted into left- and right-circularly polarized light respectively by a quarter-wave plate before reaching sample surface. A non-reciprocal phase shift between the two beams that is twice the size of Kerr rotation is picked up upon reflection from sample surface. The quarter wave-plate converts the reflected beams back into linear polarizations with a 90˚ rotation of polarization axis and thus swap their back-propagating axis in the PM fiber. Therefore, once the light beams pass the EOM again on their back-propagating trip, the two beams have experienced the exact same light path but in opposite directions, they will interfere and be guided by a PM circulator to an ac-coupled photodetector, Kerr signal can be determined by lock-in detection of signal at ω_m and $2\omega_m$.

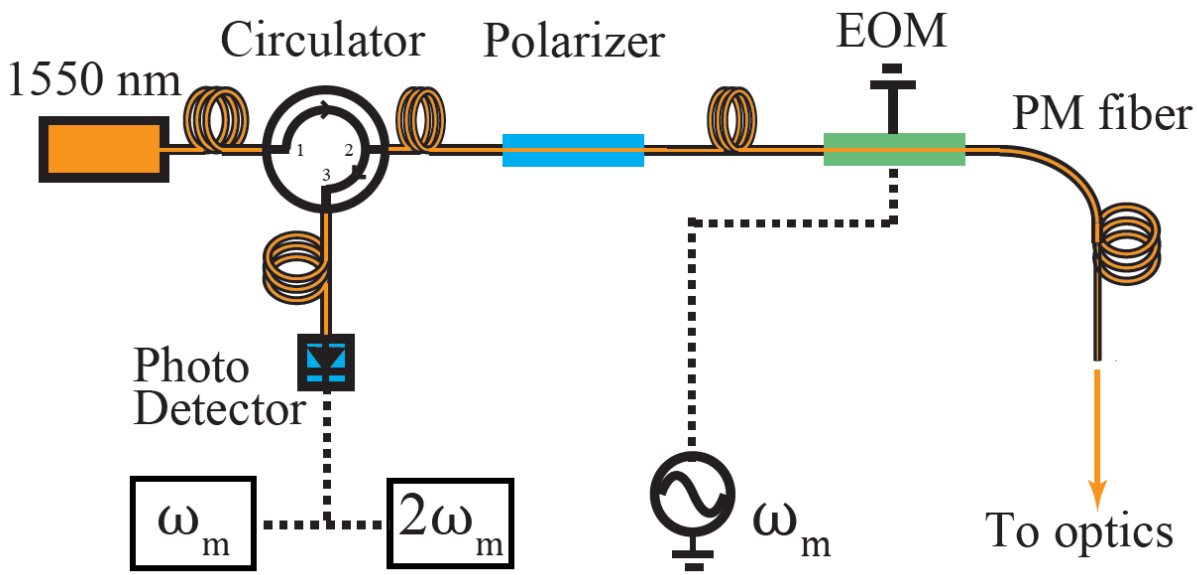

Fig. 2.3: Schematic of the loopless Sagnac interferometer

2.3 Phase modulation and Kerr signal calculation

As mentioned in the previous section, an EOM is used to add time-dependent phase modulation to the light beams, such time-dependent modulation enables lock-in detection of the signal and bias the system to the dark fringe for a better resolution. The EOM also introduces a large phase difference between the two light beams due to its strong linear birefringence, combined with the short coherence length due to the use of broad band light source, the two beams are not coherent when they leave the EOM and cross talk between them are greatly suppressed. The modulation frequency ω_m and modulation depth need to be carefully chosen to ensure the best performance of the Sagnac interferometer.

Consider a time dependent sinusoidal phase difference $\varphi_m(t) = \phi_m \sin(\omega_m t)$ is applied to the two light beams, where ϕ_m is the modulation depth and ω_m is the modulation frequency. The

light beams are modulated twice by the EOM, the time delay τ between these two modulations is the time for the light to travel in the 'Sagnac loop'. As a result, the total phase difference between the light beams is $\Phi = \phi_m(\sin(\omega_m(t+\tau)) - \sin(\omega_m t)) + \varphi_{nr}$, where φ_{nr} is the non-reciprocal phase shift induced by Kerr effect. Due to this phase difference, the light power at the detector is:

$$P(t) = \frac{1}{2}P_0(1 + cos\Phi)$$

Assuming the light power of two beams are equally $\frac{1}{2}P_0$. The time dependent light power contains harmonics of modulation frequency ω_m that can be picked up using lock-in detections. When the modulation frequency is chosen to be the odd multiple of $\frac{\pi}{\tau}$, the AC amplitude of the power is maximized, and the equation can be greatly simplified. Take $\omega_m\tau = \pi$, the expression for $P(t)$ is reduced to:

$$P(t) = \frac{1}{2}P_0(1 + \cos(-2\phi_m \sin(\omega_m t) + \varphi_{nr}))$$

Assume φ_{nr} is small and use Jacobi-Anger expansion:

$$\cos(z\sin\theta) = J_0(z) + 2\sum_{n=1}^{+\infty} J_{2n}(z)\cos(2n\theta)$$

$$\sin(z\sin\theta) = 2\sum_{n=1}^{+\infty} J_{2n-1}(z)\sin[(2n-1)\theta]$$

The Power of light is expanded into series of harmonics of the modulation frequency:

$$2P(t)/P_0 = 1 + J_0(2\phi_m) + 2J_1(2\phi_m)\sin(\omega_m t)\sin(\varphi_{nr})$$

$$+2J_2(2\phi_m)\cos(2\omega_m t)\cos(2\varphi_{nr}) + \cdots$$

The odd harmonics are proportional to $\sin(\varphi_{nr}) \cdot P_0$ and even harmonics are proportional to $\cos(\varphi_{nr}) \cdot P_0$. Two lock-in operating at ω_m and $2\omega_m$ are used to detect the first (I_ω) and second harmonics ($I_{2\omega}$) of the signal, the non-reciprocal phase shift can be calculated using:

$$\varphi_{nr} = \arctan\left[\frac{I_\omega J_2(2\phi_m)}{I_{2\omega} J_1(2\phi_m)}\right]$$

Choosing $2\phi_m = 1.84$ to maximize $J_1(2\phi_m)$, to get a maximized first harmonics signal, the expression for non-reciprocal phase shift can be further reduced to:

$$\varphi_{nr} = 0.54\ \frac{I_\omega}{I_{2\omega}}$$

Most sources of error such as the residual amplitude modulation due to the imperfect EOM will be 90° out of phase with the real signal, thus the modulation frequency, modulation depth and the phase on the lock-in amplifier should be carefully calibrated to obtain the ideal performance. The modulation frequency ω_m can be calibrated by finding the perfect $2\omega_m$. Firstly, one should roughly estimate the modulation frequency ω_0 based on the length of the fiber and the speed of light, then set the modulation frequency to $2\omega_0$. At the perfect $2\omega_m$, the second harmonic signal should go to zero, because the two modulations cancel each other out and there will be no AC component of the light power. To find the perfect $2\omega_m$, one can sweep the modulation frequency around $2\omega_0$ and find the frequency that gives the lowest second harmonic signal, ω_m is then just half of that frequency. Fig. 2.4 shows a frequency scan near the doubled ideal modulation frequency, where a clear minimum is visible whose frequency is exactly $2\omega_m$.

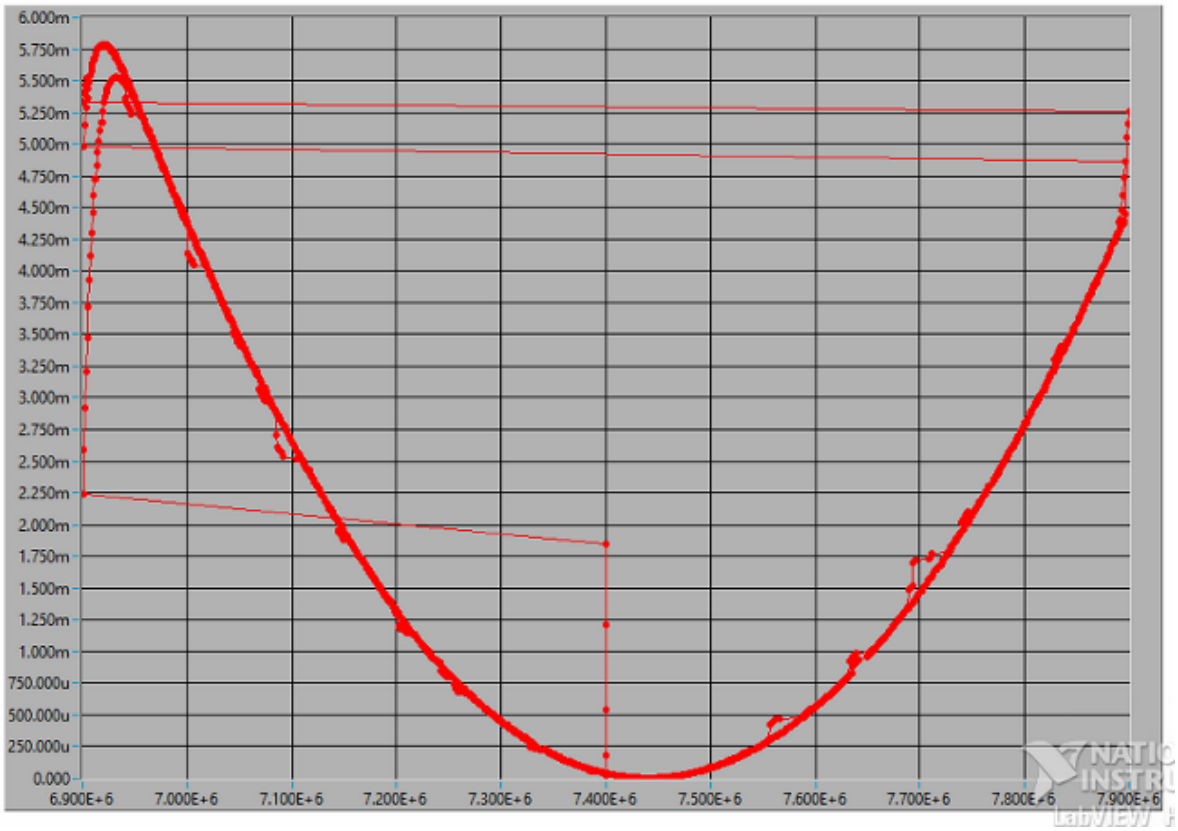

Fig. 2.4: Frequency dependence of second harmonic signal near doubled ideal modulation frequency, the minimum in second harmonic signal indicates the frequency is exactly $2\omega_m$. X axis is modulation frequency, Y axis is second harmonic signal in the unit of Volts.

Once the modulation frequency is calibrated, the modulation depth and phase of lock-in amplifier can be found by measuring a magnetic sample with known Kerr rotation. The modulation depth can be simply set by changing the amplitude of the function generator until the first harmonics signal is maximized. The phase of lock-in can be set by maximizing the in-phase component of the first harmonics signal while the light is focused on a magnetic sample. Finer adjustment can take the advantage of the fact that errors are out of phase from the true signal, thus when measuring a non-magnetic sample such as silver mirror, the correct phase should give

the most clean and stable signal. Small variations of the phase angle can be made to the data of a long-term measurement on a silver mirror, then the phase angle that gives the least noisy data can be set as the correct phase. Fig. 2.5 shows the in-phase component of the first harmonic signal for a 9-hour long measurement on a silver mirror, each curve is extracted from the same data but with a 1.8° difference in phase setting with respect to its neighbor. The yellow and orange data at the top represent the in-phase component near the perfect phase angle, which is flat and drift-free, while other curves with slightly wrong phases drift because the out of phase error leaks into the in-phase component.

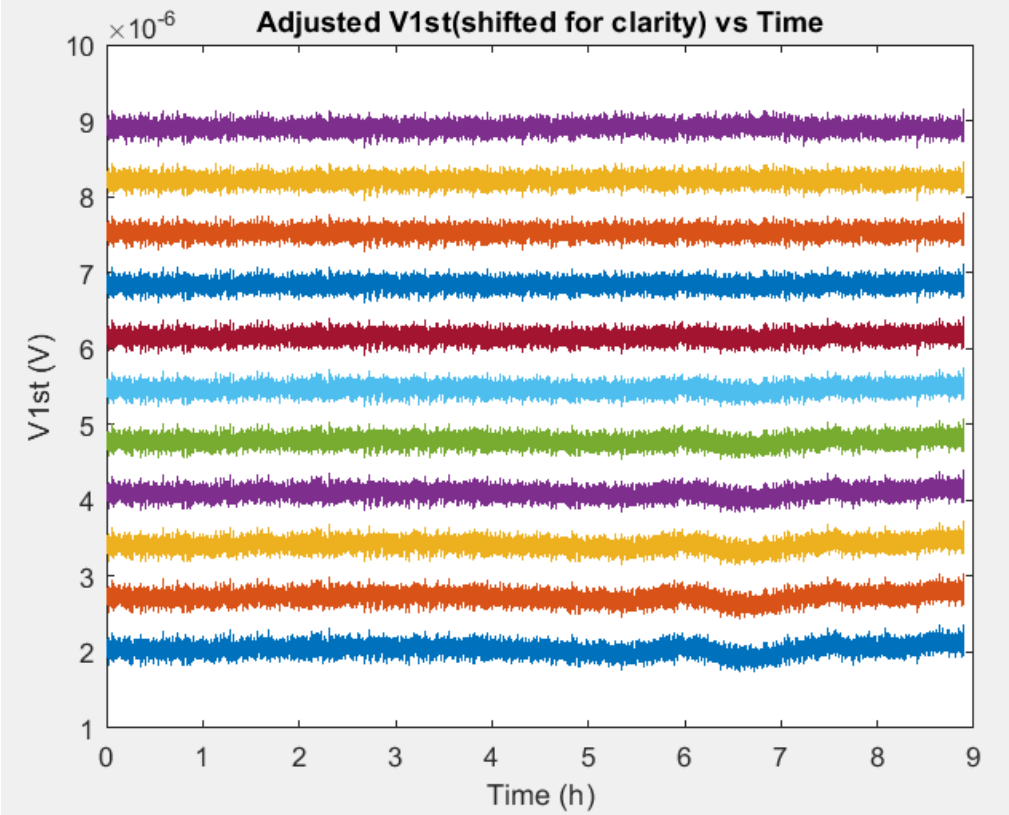

Fig. 2.5: In-phase component of the first harmonic signal of a 9-hour measurement on a silver mirror, with slightly different phase angle between each curve. 1.8° is added to the phase angle between each curve, from bottom to top. The yellow and orange curves at the top represent the in-phase component at the perfect phase setting, while the curves at the bottom with wrong phases are not stable, a small portion of the noisy out-of-phase component leaks into the in-phase component due to the wrong phase.

2.4 Interpretation of the non-reciprocal phase shift

The measured value has been called ‘non-reciprocal phase shift’ in this chapter, in the case where there the sample hosts only Kerr effect or linear birefringence, the measured phase shift is exact zero for linear birefringence only case, and directly represents twice of the Kerr rotation in the Kerr effect only case:

$$\theta_k = \frac{1}{2}\varphi_{nr} = 0.27\ \frac{I_\omega}{I_{2\omega}}$$

When the sample has both Kerr effect and linear birefringence, the situation will be complicated. Linear birefringence will scatter light from one circular polarization to another, causing additional coherent light path in the system and additional contribution to the non-reciprocal phase shift. As a result, the phase shift is proportional to Kerr rotation but modulated by a factor depending on the birefringence of the sample. If the sample has a temperature dependent linear birefringence, the measured phase shift can also be temperature dependent even if the Kerr effect is temperature independent.

Chapter 3

$NiBi_3$

3.1 Introduction

Bi/Ni bilayer is one of the intriguing candidates for triplet p-wave superconductors that are attracting lots of attention due to its potential for quantum computing applications [9]. When Bi thin film is deposited on thin ferromagnetic Ni layer, the bilayer system becomes superconducting around 4K [10], with thickness dependence of T_c on both Bi and Ni layer. Coexistence of superconducting gap and ferromagnetism was observed in the Ni layer by tunneling spectroscopy [11]. The pairing mechanism of the superconductivity in the bilayer systems grown by molecular beam epitaxy (MBE) is still under debate. Andreev reflection spectroscopy shows no suppression of the differential conductance in the superconducting gap with injection of spin polarized current, suggesting the spin-triplet pairing of the order parameter. Polar magneto-optic Kerr effect (MOKE) [12] and superconducting quantum interference device (SQUID) measurements [13] show evidence for time reversal symmetry breaking (TRSB) and formation of chiral domains, the superconductivity is believed to be on the Bi surface away from the Bi/Ni interface, mediated by magnetic fluctuations induce by Ni layer, and holds a $d_{xy} \pm$ i$d_{x^2-y^2}$ nature due to the symmetry requirements of the system. Time-domain THz spectroscopy [14] detected a nodeless bulk superconductivity in the entire Bi layer, which is interpreted as a sign of chiral p-wave like pairing. In addition, more complications are added to this puzzle due to the discovery of formation of a superconducting compound $NiBi_3$ in the Bi/Ni

bilayer system. $NiBi_3$ is shown to be a type-II s-wave superconductor with Tc around 4K [15,16], it was first detected by X-ray diffraction (XRD) in the thermally evaporated Bi/Ni bilayer films [17] and assigned as the reason for observed superconductivity in such system. Later studies on both pulse-laser deposited (PLD) [18] and sputter deposited [19] Bi/Ni bilayers show no superconductivity in the samples without the presence of $NiBi_3$ impurity. Although the growing conditions are different from the heavily studied MBE samples, concerns have been raised about the origin of superconductivity in the Bi/Ni bilayer. It has been proposed recently that bulk superconductivity in the Bi layer near Bi/Ni interface due to $NiBi_3$ impurities, combined with strong spin-orbit coupling provided by Bi layer and external magnetic field provided by Ni layer, can induce p±ip like superconductivity on the Bi surface away from Bi/Ni interface due to proximity effect [20]. More interestingly, coexistence of ferromagnetism and superconductivity induced by high surface fraction is found in $NiBi_3$ nanoparticles by SQUID measurement [21]; surface induced magnetic fluctuations in single crystal $NiBi_3$ are also observed by electron spin resonance (ESR) measurements under 160K [22]. These studies suggest TRSB observed in Bi/Ni bilayer systems may come from the ferromagnetic order in $NiBi_3$ impurity, likely caused by surface related effects. However, direct evidence for surface related magnetic order in superconducting $NiBi_3$ is still missing. Thus, to fully understand the superconducting phase of $NiBi_3$, and to gain deeper insight in the origin of superconductivity of Bi/Ni bilayer system, we perform MOKE measurements using a Sagnac interferometer on $NiBi_3$ single crystals.

3.2 Experimental setup

$NiBi_3$ is a type-II superconductor that becomes superconducting below 4K, its upper critical field is about 0.3T. To fully quench superconductivity and study the Kerr contribution from trapped

vortices, and to test for possible surface induced ferromagnetism detected by SQUID measurements in $NiBi_3$ nanoparticles with a saturation field over 0.7T, we need an experimental platform that allows Sagnac measurements down to half T_c (<2K) and high magnetic field (>1T), our old setups using Janis cryostats and home-made superconducting solenoid or permanent magnet for magnetic field do not meet these requirements. In addition to temperature and field requirements, scanning is also needed for this project, because $NiBi_3$ crystals are typically needle like and very small in size, they are also very soft and do not have flat surfaces to let you focus light onto them easily. Thus, a scanner also needed to be added to the new setup, making light focusing possible. Putting all these in mind, we constructed a PPMS insertion probe, it uses PPMS to control the temperature and provide magnetic field, enabling scanning Sagnac measurements down to 1.8K with magnetic field up to 9T.

The PPMS insertion probe used in this project is co-built by Camron Farhang and me. A schematic of this probe is presented in Fig. 3.1. The main body of the probe is made from a thin-walled carbon fiber tube for its high mechanical strength and relatively low thermal conductivity. Six home-made contact baffles (Fig. 3.2) are installed throughout the whole length of the tube to thermally anchor the tube to the inner wall of PPMS sample chamber and shield the black-body radiation from the room temperature top piece of the probe. These six contact baffles are essential for the probe to allow the sample stage to stabilize at the base temperature of PPMS (1.8K). During the test we found if the thermal anchoring of the tube to PPMS inner wall is not good enough, the heat load into sample stage will be larger than the cooling power of PPMS at 1.8K and the sample stage can never stay stable at 1.8K. In such case the PPMS will be stuck into thermal cycles where it enters pot-ops mode to obtain higher cooling power, temporarily

cooling the sample stage to 1.8K, then quickly run out of liquid helium in the pot and warm up to about 8K. A typical thermal cycle is shown in Fig. 3.3.

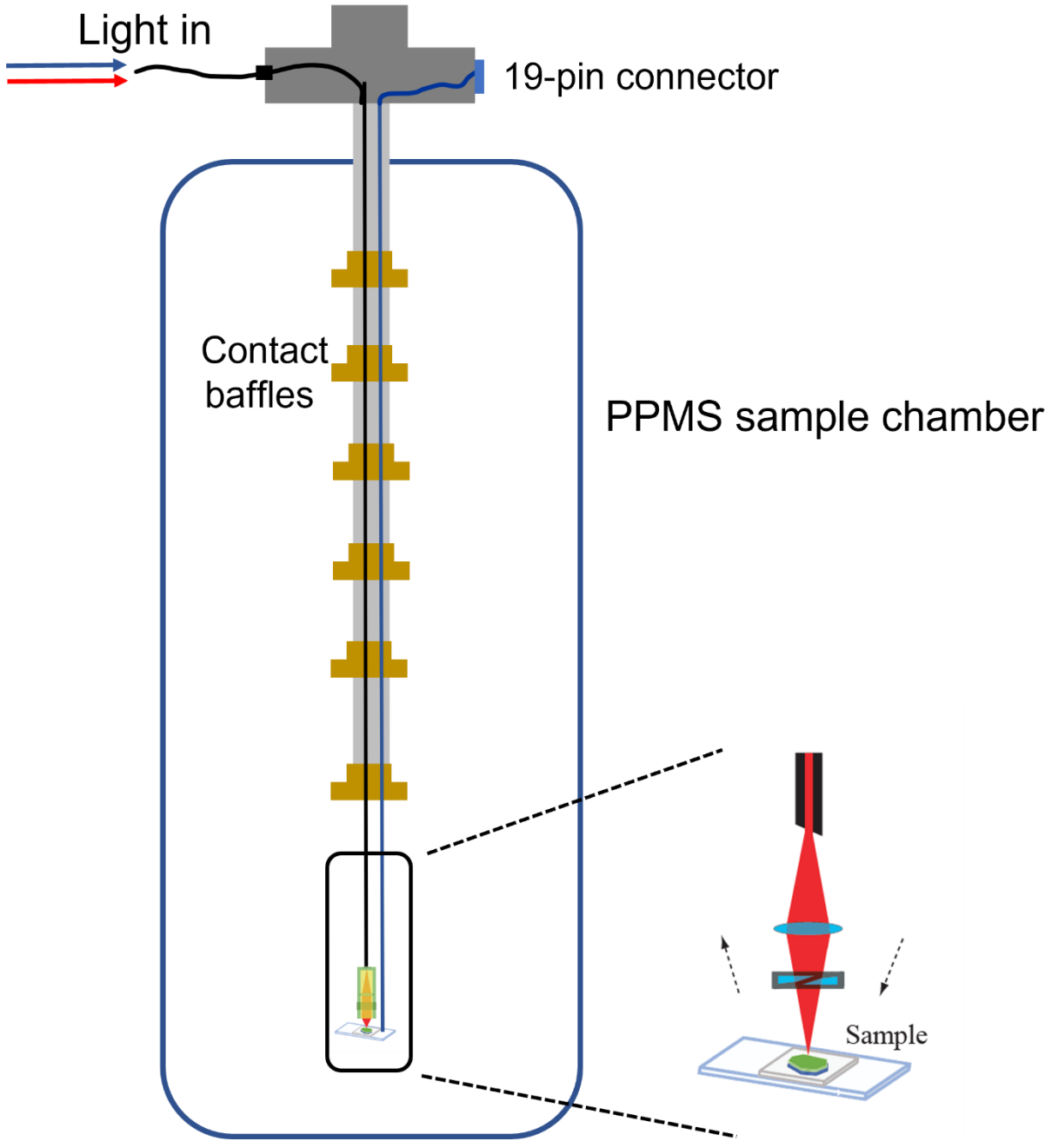

Fig. 3.1: Schematic of the PPMS probe

Fig. 3.2: Home-made contact baffles that are crucial to reduce the heat load into PPMS sample chamber. They work as both contact baffles between the probe and the PPMS sample chamber, and radiation shields to reduce thermal radiation from the top.

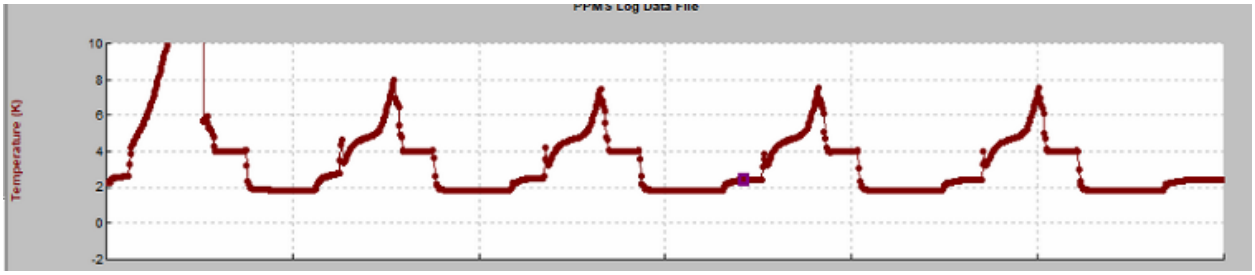

Fig. 3.3: Thermal cycle of PPMS when the heat load overpowers the cooling power.

The PM fiber is fed into PPMS through the probe by a home-made Teflon ferrule squeezed into a Swagelok fitting by replacing the front and back ferrule set. The bare PM fiber is threaded through the small hole in the ferrule and polished at both ends during the fabrication, the ferrule is then squeezed tight into the Swagelok fitting by the nut piece and seals around the PM fiber. With such feedthrough the PPMS is still able to reach its base pressure 0.1mTorr when HiVac mode is turned on.

The optics, including the cold end of the fiber, lens and wave plates are mounted in a small optics tube, the tube is connected to a home-made cryogenic piezo biomorph scanner, enabling the scanning by moving the optics tube and thus the light spot. A schematic and a picture of the bimorph scanner is shown in Fig. 3.4, with ~1.5 inch long piezo, the scan range at 300K is 300 μm, while for 1.8K it is suppressed to a few tens of microns, which is still enough for our measurements. Fig. 3.5 shows a microscope picture and a Kerr image taken by the scanner of a ferromagnetic Cr-doped $(Bi,Sb)_2Te_3$ van der Waals heterostructure [23], demonstrating the range and spatial resolution of our scanning MOKE microscopy at 1.8K.

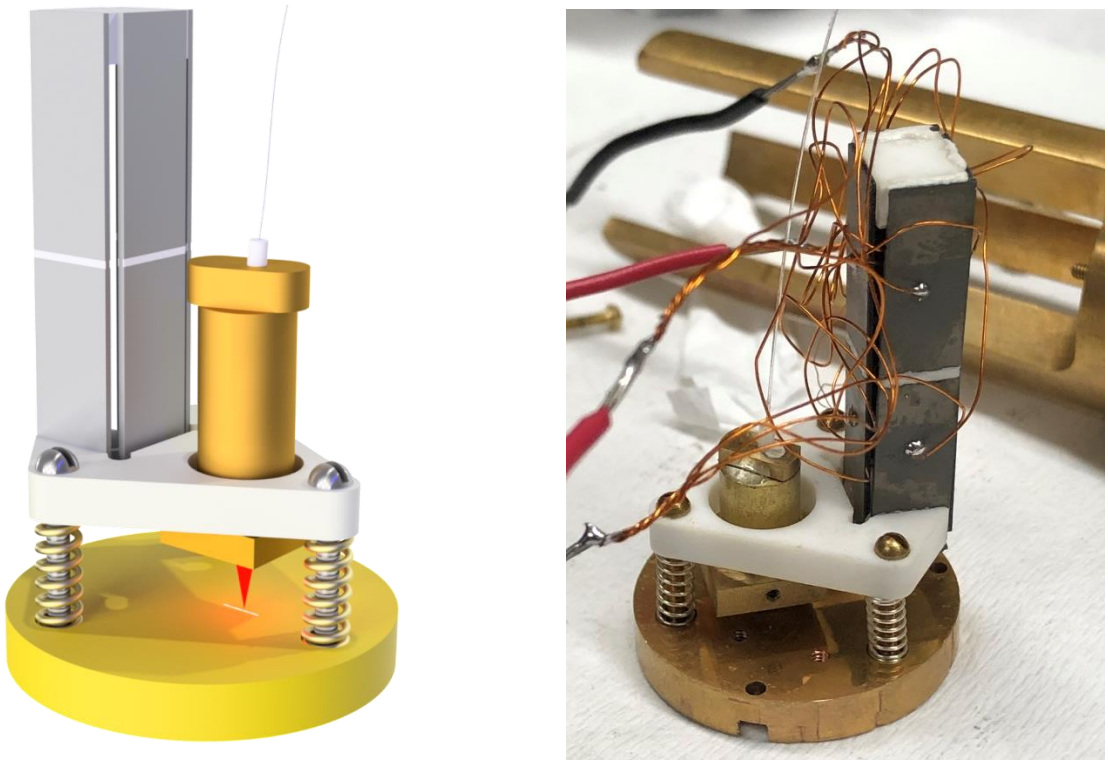

Fig. 3.4: Schematic and picture of the bimorph scanner

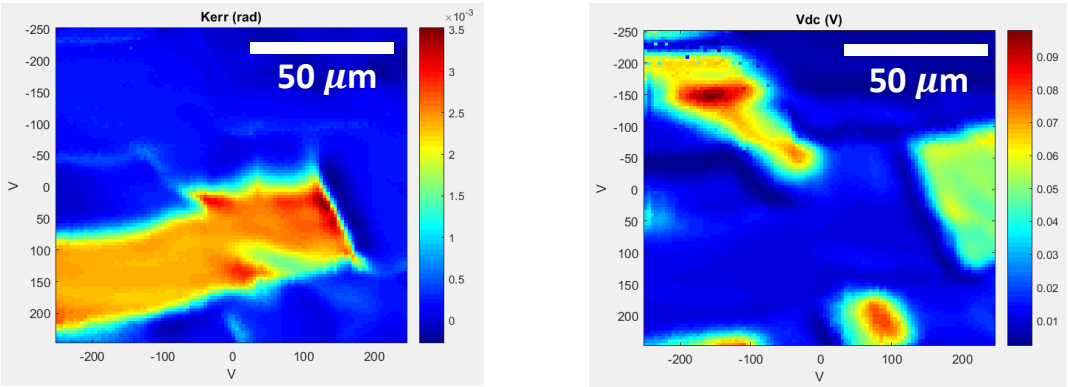

Fig. 3.5: Scan image of Kerr signal (left) and DC reflected power (right) of a ferromagnetic Cr-doped $(Bi,Sb)_2Te_3$ van der Waals heterostructure, at 1.8K. The width of the Hall-bar shaped device is about 30 μm.

3.3 Sample mounting

Needlelike $NiBi_3$ single crystals were grown from self-flux method [22] with b axis along the longest dimension, typical size of such single crystal is ~3 mm × 0.2 mm × 0.2 mm. Fig. 3.6 shows a picture of one $NiBi_3$ crystal used in this study. The as-grown crystal surfaces are smooth, reflective but curvy, making it difficult to focus to and obtain good reflection from the surfaces. To overcome this difficulty, crystal is glued to a polished silver film by Apiezon N grease with an orientation that the surface of measurement is roughly parallel to the silver film, as indicated by Fig. 3.7. The silver film is mounted to sample stage and serves as a mirror substrate with good reflection, light is first focused to the silver film at the location closely next to the glued crystal, a scan image is then taken near the point of focus. The crystal surface shows up in the scan image as a less reflective area because it is at a different height than the substrate, the silver film is then carefully moved based on the scan image so that the crystal surface is now under the focused light. Final adjustment for the tripod is then made to obtain good reflection from crystal surface before it is loaded into the PPMS.

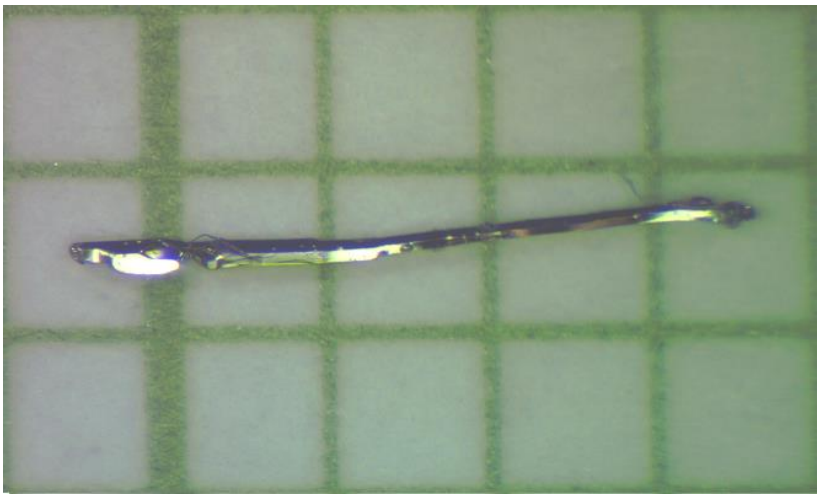

Fig. 3.6: A $NiBi_3$ crystal used in this study, it is needle shaped with shiny but curvy surfaces.

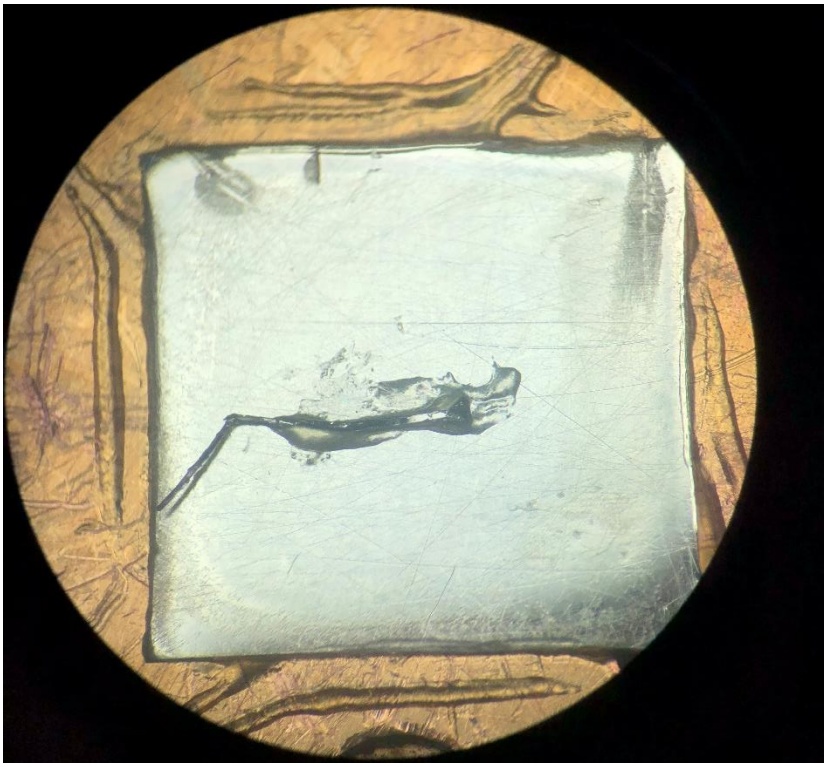

Fig. 3.7: $NiBi_3$ crystal mounted on a polished silver plate, the silver plate serves as a mirror to help locate the mounted crystal.

3.4 Results and discussion

MOKE measurements are performed on two side surfaces of the crystal, namely Surface 1 and Surface 2. Surface 1 and Surface 2 are both parallel to b axis of the crystals and almost perpendicular to each other, as illustrated in Fig. 3.6.

Fig. 3.8 shows 1.8K scan images of reflected DC light power (P_0) from both Surface 1 and Surface 2, significant inhomogeneity in light reflection from crystal surfaces due to their curvy shape can be clearly seen in both images. Flat regions with uniform high reflection ~5μW marked by the black boxes are chosen areas of MOKE measurements, by focusing light on such reflective and uniform regions using the scanner, we increase the signal stability and reduce the error originated from significant light power change in the temperature dependent measurements caused by motion of light spot due to thermal contraction.

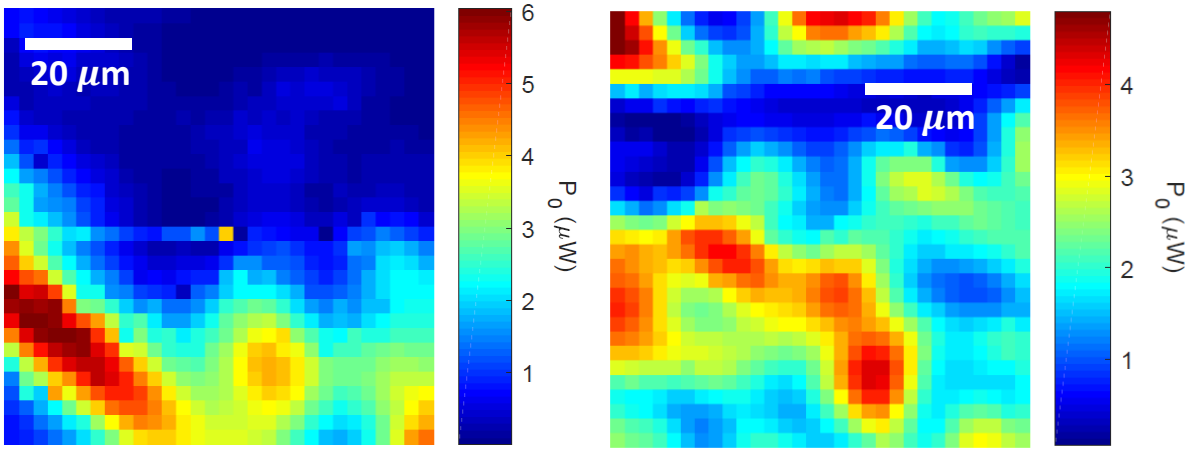

Fig. 3.8: Scan image of surface 1 (left) and surface 2 (right), the color scale indicates the reflected DC power.

To test for possible spontaneous TRSB in the superconducting phase of $NiBi_3$, we measured the Kerr signal during zero field warmup (ZFW) at fixed locations on Surface 1 and Surface 2, after cooling sample under zero and ±0.01T magnetic field to 1.8K. The ZFW Kerr signal after zero field cooling are presented as green curves in Fig. 3.9, no spontaneous Kerr signal is detected at both surfaces across T_c with 20 nrad uncertainty. When a TRSB superconductor is cooled under zero magnetic field, the Kerr signal measured across T_c usually has random sign and magnitude compared to field cooled cases. This can be explained by the formation of random domains of opposite chirality because their energies are degenerated in zero field. When a small magnetic field is applied during cooling, degeneracy is lifted and domains are aligned, giving a repeatable onset of Kerr signal across T_c in both magnitude and sign, this is usually referred as the field training effect. We thus perform small field (±0.01T) trained ZFW measurements to further test the TRSB in $NiBi_3$, the results are summarized in Fig. 3.9 as red and blue curves. Again, no spontaneous Kerr signal is observed across T_c with 20 nrad uncertainty. The polar-MOKE setup used in our measurements is only sensitive to magnetic moments perpendicular to the measured plane, thus we can conclude that there are no magnetic moments perpendicular to either Surface 1 or Surface 2 in the superconducting phase, to some upper limit. Given that Surface 1 and Surface 2 are almost perpendicular to each other, we can extend our conclusion to that there are no magnetic moments perpendicular to the b axis. Some may argue that there can still be magnetic moments along the b axis, and this can be the origin of the Kerr signal observed in Bi/Ni bilayer system across T_c. However, as reported in [19], $NiBi_3$ layer formed in Bi/Ni bilayer prefers an orientation toward (203), a crystalline surface parallel to the b axis, any magnetic moment along the b axis will be in plane and will not contribute to the Kerr signal detected in Bi/Ni bilayer due to the polar Kerr setup. In comparison, a 120 nrad onset of Kerr signal was

clearly observed across T_c=4.1K in the MBE grown Bi/Ni bilayer with the same Sagnac interferometer, we therefore rule out the TRSB superconductivity in sputtered and PLD grown Bi/Ni bilayer where the $NiBi_3$ is responsible for the superconductivity.

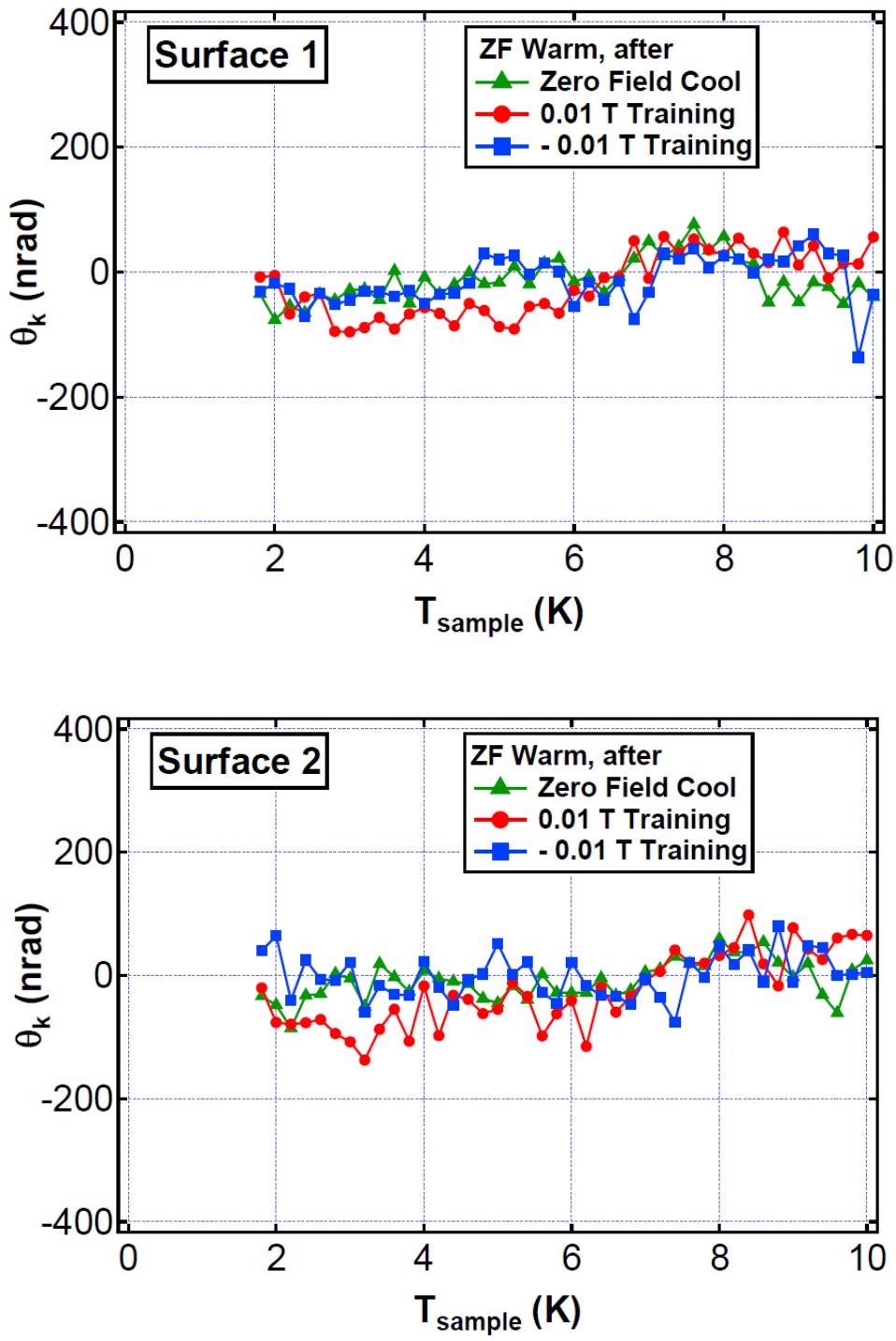

Fig. 3.9: Zero field/0.01T trained zero-field warmup data, no onset of Kerr signal observed in any case, with 20 nrad uncertainties.

We now turn to the test of possible ferromagnetism in $NiBi_3$ due to either the surface effects [21] or impurities [24]. Fig. 3.10 shows the temperature dependence of specific heat (Cp) near Tc, measured in PPMS using its heat capacity option. Inset shows the T^2 dependence of Cp/T, a kink is visible at 4K that represents a sudden change in electrical contribution, indicating the superconducting transition. A small anomaly in specific heat around 2.2K was reported in [24], which was claimed to have magnetic origin and was assigned to amorphous Ni impurities in the crushed power samples. Such anomaly is not visible in our measurement, proving the high purity of our single crystals. In addition, unlike the bulk SQUID magnetometry performed in [21], surface MOKE measurement probes an optical volume of ~ 0.1 μm^2, making it less susceptible to impurities.

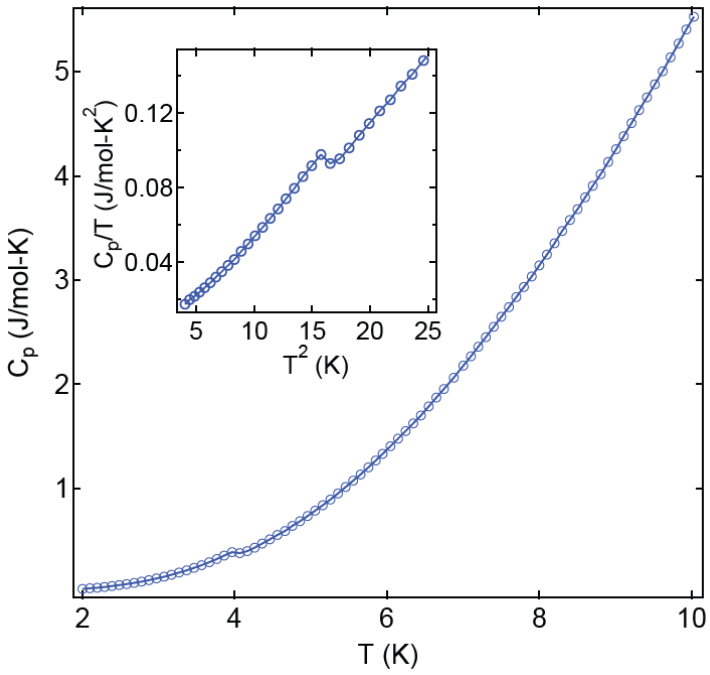

Fig. 3.10: Temperature dependence of heat capacity, a kink at 4K indicates the superconducting transition, no anomaly at around 2.2K is observed.

Magnetic hysteresis measurements are performed up to 1T at temperatures above (yellow, 10K) and below (blue, 1.8K) T_c, as presented in Fig. 3.11. Same linear field dependence of the Kerr signals is observed because they are dominated by the background of Faraday effect from the low temperature objective lens, which is 2 mm above the crystal and thus subjects to the same magnetic field as the crystal. Within an uncertainty of 5 μrad, which is higher than the zero-field case due to the fluctuation in lens contribution induced by magnetic field noise, we see no observable ferromagnetic hysteresis for both temperatures. In comparison to other measurements on ferromagnetic films using the same Sagnac interferometer, θ_K~130 μrad is measured in 2 nm Ni thin films [12] and θ_K ~500 μrad in 4 nm $SrRuO_3$ film [25], putting a strong constraint on the possible ferromagnetism in $NiBi_3$.

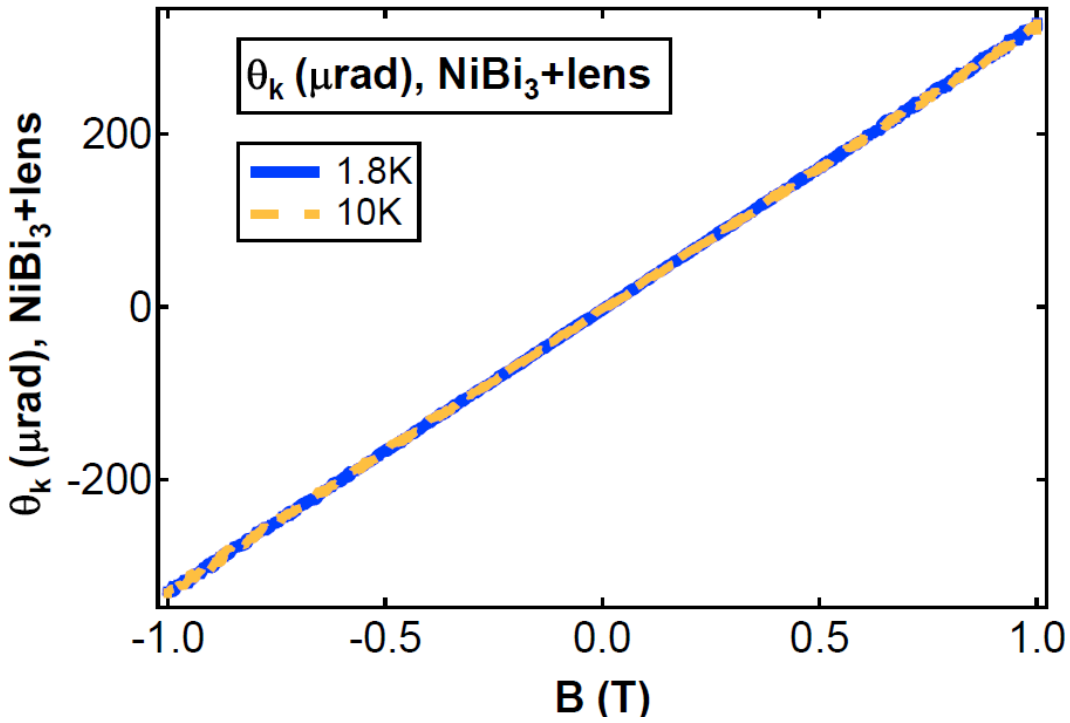

Fig. 3.11 Magnetic hysteresis measured at 1.8K and 10K, no obvious difference is observed, the measurements are dominated by the background contribution from the cryo-optics.

Finally, we take ZFW measurements with high training field to measure the remnant Kerr signal as a more stringent test for ferromagnetism. $NiBi_3$ is a type-II superconductor with lower critical field $H_{c1}(T=0)=0.012T$ and upper critical field $H_{c2}(T=0)=0.35T$ [16]. When $H_{c1}<B<H_{c2}$, vortices are formed to allow magnetic field to penetrate through the crystal, their contribution to Kerr signal is linear to B but is not observable in the data presented in Fig. 3.11 due to the large background. When magnetic field is turned off at 1.8K, a small fraction of the vortices will be trapped at pinning sites and contribute to the Kerr signal with an exponential dependence on $(T-T_c)$. Fig. 3.12 shows the ZFW Kerr signal after ±1T training for both surfaces, clear onset of Kerr signal ~ 200 nrad is observed in both measurements. Since such remnant Kerr signal is not

observed in the low field trained data, it must be the contribution from trapped vortices. The low field trained data thus showed no sign of ferromagnetism across T_c with 20 nrad uncertainty, four orders of magnitude smaller than the value measured from the ferromagnetic Ni and $SrRuO_3$ thin films, strongly indicating the absence of ferromagnetism on the surface of $NiBi_3$ single crystal. We conclude that the reported magnetic signal in $NiBi_3$ nanoparticles is not due to surface effects but some other origin and is likely unrelated to Bi/Ni bilayers.

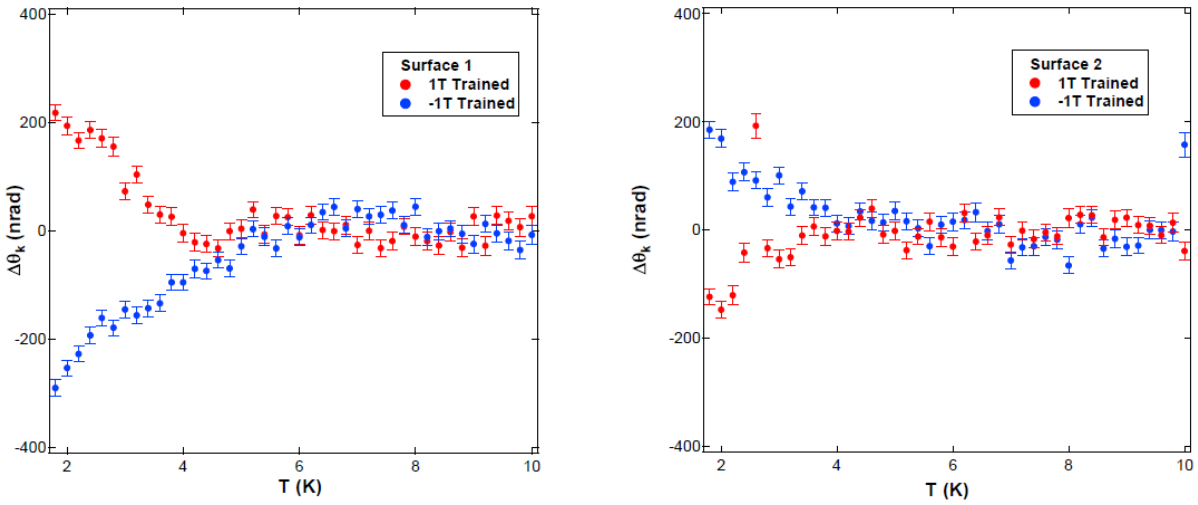

Fig. 3.12: +/-1T trained zero-field warmup measurements, onset of Kerr signal at T_c is caused by contributions from trapped vortices.

3.4 Conclusion

In conclusion, we have performed high-resolution surface magneto-optic Kerr effect measurements using a Sagnac interferometer on single-crystal $NiBi_3$ and find no sign of any spontaneous Kerr signal except for contributions from trapped vortices. This strongly indicates the absence of TRSB in $NiBi_3$, whether due to TRSB in the superconducting state or any coexisting ferromagnetism, and we conclude that the superconductivity found in non-epitaxial Bi/Ni is distinctively different from that in epitaxial Bi/Ni.

Chapter 4

Sr_2RuO_4 and Sr_2RuO_4-Ru eutectic phase

Sr_2RuO_4 is an unconventional superconductor that has been studied heavily since its discovery in 1994 [26], however its pairing mechanism is still unclear today after 30 years of experimental and theoretical effort. In this section I will discuss my MOKE study on Sr_2RuO_4, by applying uniaxial strain to single crystals and testing TRSB in the Sr_2RuO_4-Ru eutectic phase.

4.1 Introduction

4.1.1 Sr_2RuO_4

Superconductivity is one of the most intriguing ground states in condensed matter systems. In the BCS theory, electrons come into pairs below the transition temperature, known as the Cooper pairs, through an effective attractive interaction caused by electron-phonon interaction. Electrons in a Cooper pair have opposite spin, forming an odd parity (anti-symmetric) singlet state for the spin part of wavefunction. Since electrons are fermions, the orbital part of the Cooper pair wavefunction must be even parity (symmetric) to maintain the odd parity of the total wavefunction. The orbital wavefunction can be labeled by its orbital angular momentum L, which takes integer number 0, 1, 2, etc., where states with even L are even parity states and odd L for odd parity states. Using the notations adopted to describe atomic orbitals, the different orbital momentum states are called s-wave (L=0), p-wave (L=1), d-wave (L=2) states, etc. In the BCS theory the orbital momentum of Cooper pairs is chosen to be zero, representing an s-wave

singlet pairing. It is worth noting that in the presence of spin orbit coupling, which is the case for Sr_2RuO_4 and most unconventional superconductors, spin is no longer a good quantum number, the terms 'singlet' and 'triplet' could be misleading, while the even/odd parity language remains valid, so in the following context I will use the even/odd parity language.

BCS theory is a very successful microscopic theory of superconductivity, it naturally explains many properties observed from superconducting elements and alloys. According to BCS theory, an isotropic gap Δ opens at the Fermi surface below transition temperature T_c, its magnitude grows when temperature is further lowered below T_c following equation $\Delta(T) = \Delta_0\sqrt{1 - T/T_c}$, where $\Delta_0 = 1.76k_BT_c$ [27] is the gap value at 0 K. This agrees with the phenomenological Ginzburg-Landau theory on superconductivity where an order parameter with temperature dependence $\sqrt{1 - T/T_c}$ emerges below T_c, if we assume the modulus of the complex order parameter is proportional to the magnitude of gap, which is indeed the case. The opening of superconducting gap gives an exponential temperature dependence of the thermal conductivity and relaxation rate in NMR measurements, which agrees well with experiments.

The scenario described above, a phonon mediated, isotropic s-wave singlet pairing superconductivity is now usually referred to as 'conventional superconductivity', while any other types of superconductivity with different pairing mechanisms, gap symmetries or both, are called unconventional superconductivity. One famous example is the family of high T_c cuprate superconductors [28], they are antiferromagnetic Mott insulators due to strong electronic correlations in the undoped regime, and become superconducting when additional carriers (electron or hole) are introduced into the system through doping. It is shown by experiments [29,30] that electron-phonon interaction has little contribution to the superconductivity of cuprates, its d-wave [31] pairing is mediated by antiferromagnetic

fluctuations, the antiferromagnetic fluctuation plays a similar role as electron-phonon interaction in the BCS theory. Other important examples include iron-based superconductors and heavy fermion superconductors where spin-fluctuation is believed to be the reason for superconductivity.

Sr_2RuO_4 is the first layer perovskite superconductor that does not contain copper, unlike the high-T_c cuprate superconductors, it has a relatively low T_c 1.5K. Soon after its discovery it was confirmed as an unconventional superconductor based on the strong suppression on its superconducting transition temperature by the non-magnetic impurity [32], which violates the Anderson's theorem [33] that states s-wave superconductivity is not sensitive to standard elastic impurity scattering. More importantly, various experimental evidence for the parity of pairing has been reported, most of them point to an odd parity.

A major difference between the even parity ('spin-singlet') and odd parity ('spin-triplet') pairing is the competition between superconducting condensation energy and spin polarization energy. In an even parity superconductor, superconducting condensation requires electron spins to be anti-aligned in the Cooper pair, this causes an immediate drop in electron spin susceptibility (Pauli susceptibility) when the material enters superconducting phase, because the superconducting condensation removes electrons with opposite spins near the Fermi energy and eliminates their contribution to Pauli susceptibility through Zeeman splitting in the presence of magnetic field. In the case of odd parity pairing, however, electrons have equal spin in a Cooper and such reduction in spin susceptibility will not occur. Another effect related to this energy competition is the Pauli limiting of upper critical field. In a normal superconductor, superconductivity is quenched by external field when the energy cost of generating screen current to expel external field exceeds the energy gain of maintaining the superconducting phase,

such limit on upper critical field is called orbital limiting. In the case of a strongly type-II superconductor that allows effective flux penetration so that the superconductivity can be maintained at high field, Pauli limiting can be dominant and causes a smaller upper critical field than in the orbital limiting scenario for an even parity superconductor. The Pauli limiting is the situation that in a strong magnetic field, when the energy lowering caused by Zeeman splitting of free electrons surpasses the energy gain of them forming Cooper pairs, the system will transit into normal state to lower the total energy and thus superconductivity is destroyed. Similar to the case of spin susceptibility, Pauli limiting does not happen to odd parity superconductors since the spins are aligned in Cooper so there is no mechanism to save energy in external field. A signature of Pauli limited upper critical field is that the upper critical field H_c roughly follows equation: $\frac{1}{2}\chi_P {H_c}^2 = \frac{1}{2}N(0)\Delta^2$, where χ_P is the Pauli susceptibility, $N(0)$ is the density of states at Fermi energy and Δ is the superconducting gap. By converting the parameters into T_c, this equation indicates that in a Pauli limited superconductor, the upper critical field should be the same order as transition temperature T_c, in the unit of Tesla and Kelvin.

The spin susceptibility in the superconducting phase of Sr_2RuO_4 has been measured by nuclear magnetic resonance (NMR) Knight shift [34] and polarized neutron scattering (PNS) [35], both methods detected no reduction in the spin-susceptibility across T_c, which was interpreted as direct evidence for spin-triplet pairing. The odd parity pairing was further supported by phase sensitive measurements [36,37]. However, the upper critical field in the ab plane is confirmed to be strongly Pauli limited [38,39], and the transition is proved to be first order, a signature only for Pauli limiting. This obvious discrepancy caused some problems in the interpretation of the pairing symmetry, it was believed that Sr_2RuO_4 may have some strange limiting mechanism on its in plane upper critical field since the evidence for odd parity from other experiments are so

strong. Two commonly used probe to test TRS in unconventional superconductors, Muon spin rotation (μSR) [40] and MOKE [25] both found evidence for TRSB in the superconducting phase, combined with the odd parity paring, a chiral p-wave order parameter $p_x \pm ip_y$ was proposed. Despite the additional contradictory results such as the failure in searching for edge magnetic field induced by edge current for $p_x \pm ip_y$ state [41–44] and the absence of splitting in transition temperatures of the two degenerated order parameter under symmetry breaking induced by in-plane magnetic field or uniaxial strain [45–47], it was generally accepted that Sr_2RuO_4 is a topological p-wave superconductor [48,49] that supports Majorana bound states at vortices [50] and is a promising candidate to realize quantum computing.

Dramatically, the chiral p-wave picture has been overturned recently. In 2019, 25 years after the discovery of Sr_2RuO_4, a group from UCLA carefully repeated the NMR Knight shift measurements [51] with lower pulse energy and observed reduction of the Knight shift below the transition temperature, putting strong constraint on the possible order parameter and exclude the long-established chiral p-wave picture. The authors have demonstrated that the instantaneous heating on the sample from large pulse energy will keep the sample temperature above T_c and thus prevent the measurement from picking up any information in the superconducting phase, causing the false negative results from previous NMR studies. This result is quickly repeated and confirmed by other groups [52]. Motivated by this discovery, PNS experiment is also repeated with lower applied magnetic field, a similar reduction in spin susceptibility is observed in the new study [53]. Now it seems that odd parity is not possible, although the phase sensitive measurements are still strong evidence for odd parity, maybe it's a good time now to repeat them to test the validity.

At the time of writing, the debate on the order parameter of Sr_2RuO_4 is still ongoing. In addition to all the experimental evidence mentioned above, recently ultrasound spectroscopy measurements [54,55] indicate a two-component order parameter, adding strong constraint on the order parameter. Currently three possible order parameters are proposed, $d_{xy} \pm i d_{yz}$ [56], $d+ig$ [57] and $d+is$ [58], they are all two-component, break TRS and hold even parity. The first order parameter is a chiral d-wave order while the latter two represent a mixer of d-wave and g(s)-wave order parameter, the T_c for the d-wave and g(s)-wave states are accidentally equal, due to the fine tuning of the parameters of the system. Each of the proposed orders explain most of the experimental results, but are contradictory to some of the other experiments, so there is no widely accepted theory at this point.

The motivation to perform MOKE measurement on Sr_2RuO_4 under uniaxial strain is mainly due the report of μSR measurements under strain [56], a split in T_c and onset temperature of TRSB T_{TRSB} was reported, while the T_{TRSB} is suppressed only slightly to between 1.4K and 1.5K, the T_c is greatly enhanced to over 3K under strain. This result, combined with another publication of the same group of authors that reports the absence of splitting in T_c and T_{TRSB} under hydrostatic pressure [59], suggests the accidental degenerated order scenarios are not possible, thus supports the chiral d-wave order. Since MOKE and μSR gave similar results on Sr_2RuO_4 single crystal, it is natural to measure MOKE under uniaxial strain to confirm the findings made by μSR.

4.1.2 Sr_2RuO_4-Ru eutectic phase

Although it is now well established that Sr_2RuO_4 is a spin-singlet superconductor as mentioned in the previous section, there is still hope [60] to realize spin-triplet superconductivity in a related system, the Sr_2RuO_4-Ru eutectic phase. When the crystal growth of Sr_2RuO_4 is controlled by

certain manner, Ru metal can be included in the crystal in the form of thin plates with a typical width of 1 μm and length and depth of 1-10 μm, the separation between these Ru microparticles is also typically 10 μm, as shown in Fig. 4.1. It was found that this eutectic system shows a broad superconducting transition with an enhanced T_c as high as over 3K, thus the eutectic phase is sometimes referred to as the 3K-phase of Sr_2RuO_4. The enhanced superconductivity only happens in a small filamentary region near the Sr_2RuO_4-Ru boundary, with a characteristic width in the order of coherence length of Sr_2RuO_4, which is only ~100 nm. The origin of this T_c enhancement is ascribed to the strain at the Sr_2RuO_4-Ru interface, since 3K-phase has the same upper limit of T_c (~3.5K) compared to the case of Sr_2RuO_4 under uniaxial strain, and it shows similar hysteretic behavior in the low temperature in plane upper critical field [61] that is also observed in the uniaxial strain measurements. Tunneling measurements on the 3K-phase found an onset of zero-bias conductance peak (ZBCP) below 3K [62,63], suggesting the formation of Andreev bound states in the system and thus point to a second phase transition below 3K into a TRSB superconducting phase. It is natural to think that an onset of Kerr signal may be observed in 3K-phase system when this second transition happens, and since the transition temperature is 2.4K, it can be reached using the PPMS setup without any additional modification, the only experimental difficulty is the spatial resolution, since the 3K-phase region is really narrow and below the diffraction limit at the wavelength of our measurement.

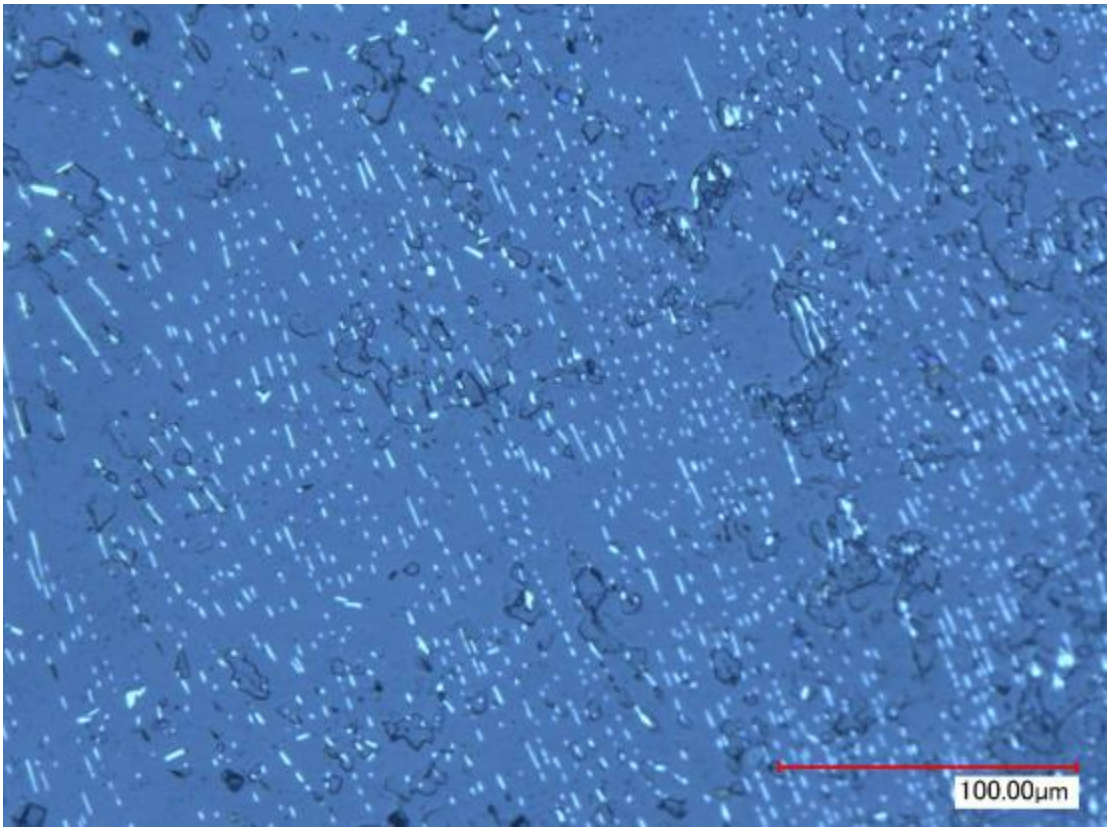

Fig. 4.1: Microscopic picture of 3K-phase Sr_2RuO_4, white stripes are the Ru microinclusions.

4.2 Experimental setup

4.2.1 Adiabatic demagnetization refrigerator

To reach the 1.5K T_c of Sr_2RuO_4, the PPMS probe mentioned in the previous chapter needs to be modified for the uniaxial strain project, the solution is to add an adiabatic demagnetization refrigerator (ADR) unit to the probe, this unit is a standard PPMS accessory that allows a one-shot cooling to 200 mK, the unit will then experience an uncontrolled free warmup to 1.8K in 4 hours.

The cooling of ADR uses the magnetic disorder entropy of paramagnetic salt. At zero magnetic field, the magnetic moments in the paramagnetic salt point to random directions, representing a fully disordered state with zero magnetization. When an external field is applied, the magnetic moments will be aligned, at least partially, towards the direction of external field. The entropy of the system is thus lowered in external field at a fixed temperature, Fig. 4.2 shows the entropy vs temperature curve of the salt at B=0 and B=B_{ext}, B_{ext} represents some finite external field value. During the refrigeration process, the salt is precooled to some low temperature by a precooling cryostat, in our case the PPMS, shown as point A in Fig. 4.2. Magnetic field is then turned on to perform an isothermal magnetization of the salt, the heat of magnetization will be absorbed by the precooling bath, and the salt is now in a state labeled as point B in Fig. 4.2. The next step will be the demagnetization and cooling, the salt will first be thermally isolated from the precooling bath, then the external field will be turned off, in this adiabatic process the temperature of the salt will decrease to its zero-field value, shown as point C. Finally, the salt will warm up along the curve for B=0 back to point A, the cooling power of the process is marked by the shaded area.

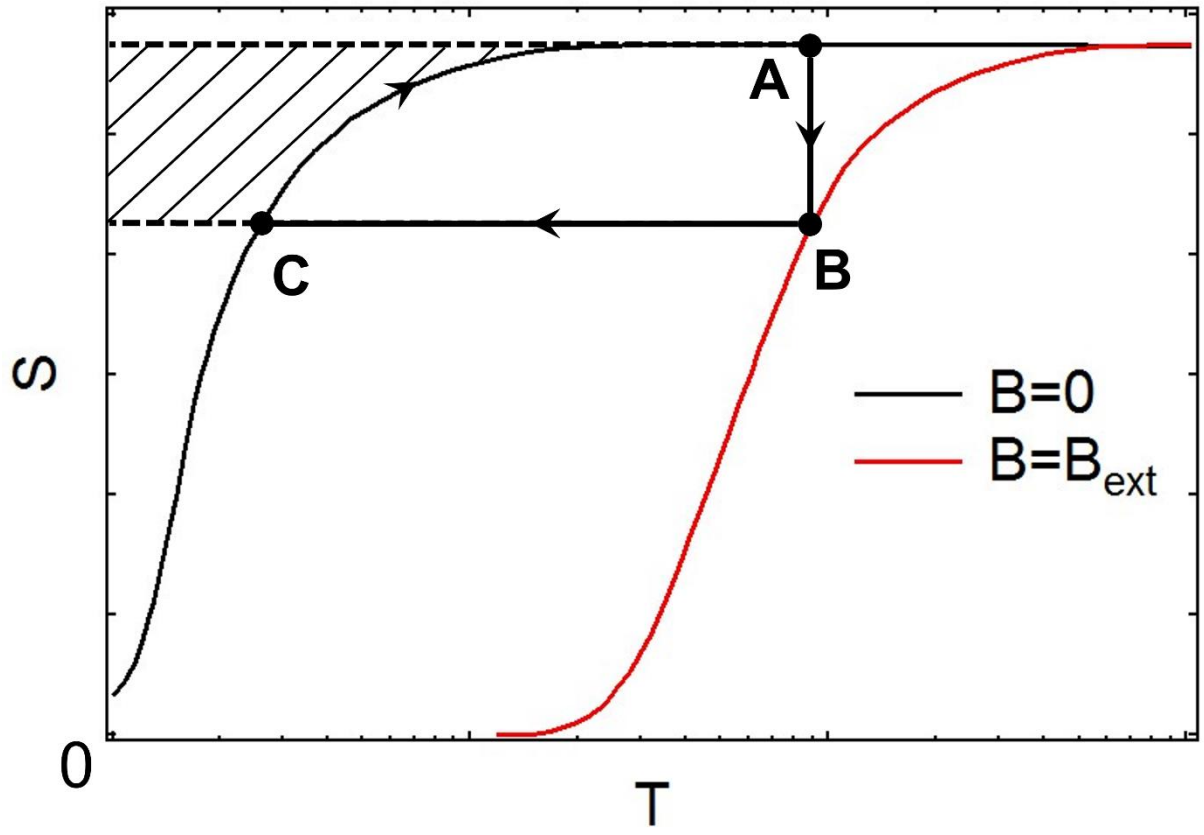

Fig. 4.2: Phase diagram of paramagnetic salt, the cooling process of demagnetization is shown by the points and arrows.

In the PPMS ADR unit, container of the paramagnetic salt is connected to the bottom puck by a thin carbon fiber rod with poor thermal conductivity, as shown in Fig. 4.3. The container is thermally connected to a sample stage on its top, providing cooling to the mounted sample. In the standard operation of PPMS ADR unit, the ADR unit is first precooled to 10K, then 9T field is turned on, since the salt is thermally disconnected to the PPMS cold finger, which is directly connected to the bottom puck, the cooling of the salt is almost purely provided through the helium vapor in the PPMS sample chamber. Once the magnetization is finished, PPMS will turn on high vacuum mode to remove all the helium gas in the sample chamber, thus thermally isolating the paramagnetic salt and sample from PPMS. The field is then turned off (or turned down to desired value for a measurement in magnetic field) after cooling the system to 1.8K to cool the sample and ADR unit to ~200mK, the system will warm up to 2K in the next 4 hours. We found in the test that the sample warms up quickly above 0.9K, as shown in Fig. 4.4, leaving only a few minutes of measurement time for the temperature range 1K-2K, which is the range we care about the most. This warmup behavior can be greatly improved if we demagnetize the ADR unit at 4K instead of 1.8K and cool the probe to 1.8K under high vacuum mode before starting the demagnetization. By following this process, the warmup curve of the sample becomes an s-shaped smooth curve between 0.2K and 2K, giving about 2 hours of measurement time for 1K-2K, shown in Fig. 4.4 lower panel.

Fig. 4.3: Picture of the ADR unit sitting on a PPMS user bridge, the paramagnetic salt is in the stainless-steel container, container is connected to the bottom puck through the carbon fiber rod.

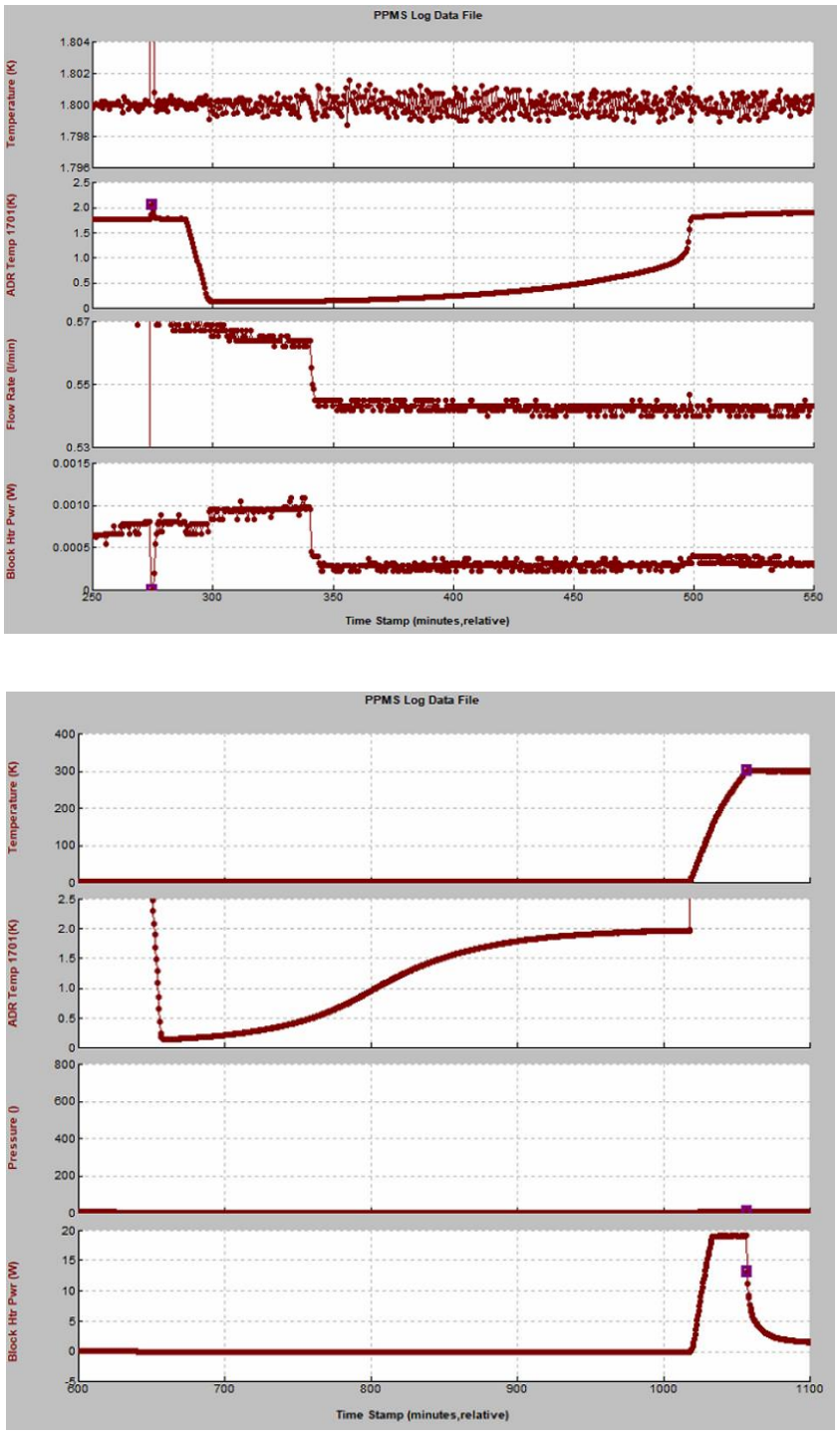

Fig 4.4: ADR unit free warmup curve, demagnetize at 1.8K (top) and 4K (bottom). When demagnetize at 4K, the warmup curve is s-shaped and smooth, giving enough time between 1K and 2K.

4.2.2 Uniaxial strain cell

A homemade uniaxial strain cell was mounted on the sample stage to provide strain, as shown in Fig. 4.5. The design of the strain cell is straightforward, titanium frames are combined by three piezo actuators through stycast 2850FT epoxy, opposite voltages are applied to the outer and inner piezo so that they apply the same type (compressive/tensile) of uniaxial strain to the sample. We use PI piezo actuator P-885.10 for this strain cell, which operates at -20V to 120V with a total travel range around 8 μm at room temperature. At 2K, the motion of the piezo is greatly reduced, but this can be overcome by applying larger voltage to drive the piezo to its max extension. Based on our test results, -120V to 600V is safe to use at 2K, the total travel range is comparable to the room temperature value. Details on the design of the strain cell can be found in many literatures [64], at the time of writing, uniaxial strain cell is commercially available from Razorbill Instruments, although it will still not be useful for this project because the space is very limited in the ADR probe, a homemade strain cell is still needed. One major difference of the strain cell we use in this project compared to standard design (even for our own design for previous projects) is that the removable sample holder is removed. This design saves space in the z direction and potentially gives a higher transfer ratio of the displacement to the sample, enabling higher strain value, and reduces the risk of sample breaking by causing less bending of the crystal when it is compressed. This approach obviously causes serious problem when the old sample needs to be removed and a new sample is mounted, since the strain project was terminated during the stage of early testing and not many crystals have been tested, sample removing did not cause too much trouble for this project, but it is not recommended for any other serious project.

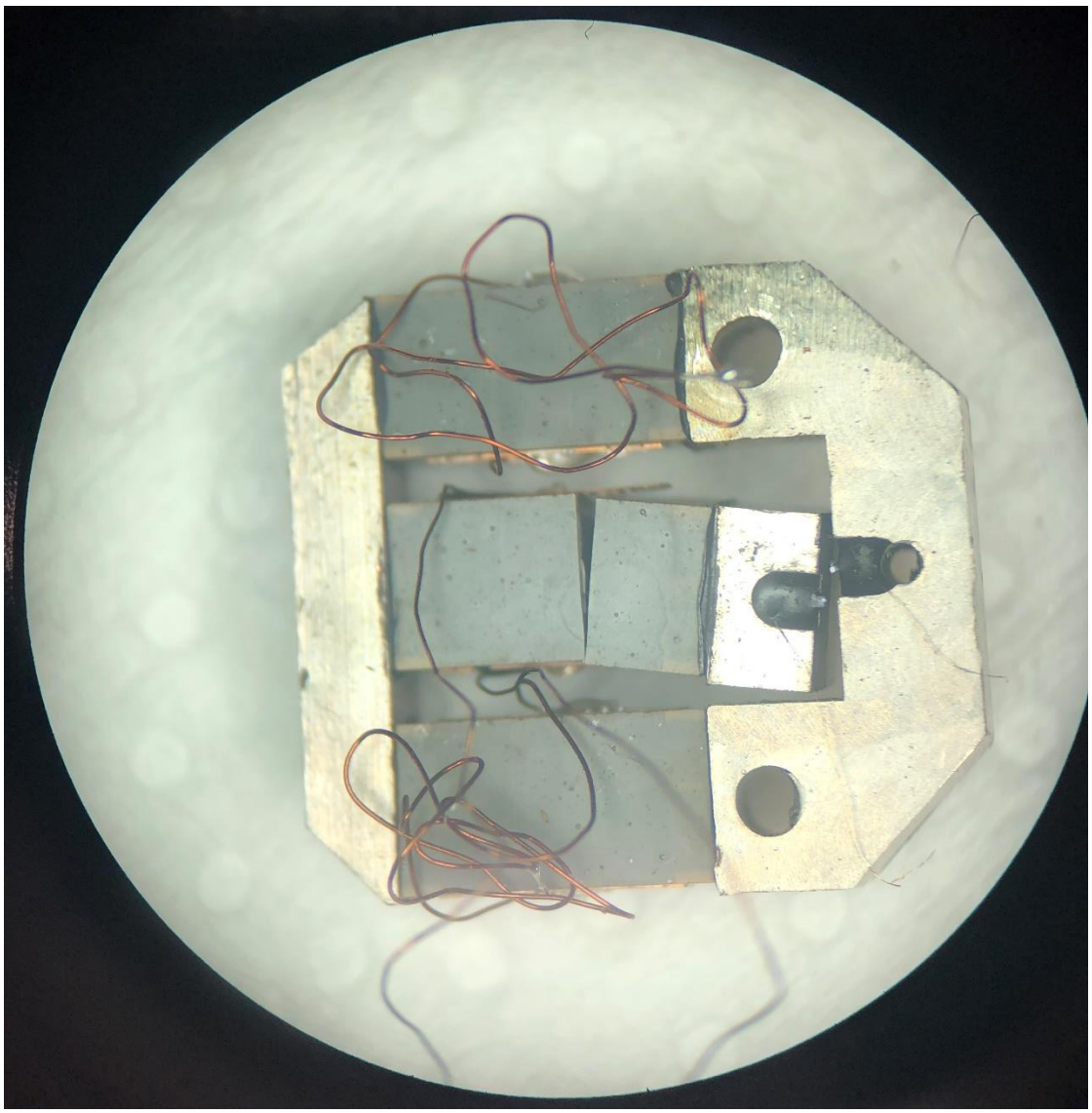

Fig. 4.5: Picture of the strain cell, with middle piezo broken.

4.2.3 AC susceptometer

To measure the T_c of Sr_2RuO_4 under strain simultaneously with the MOKE measurement, we measure AC susceptibility using a small homemade susceptometer. The susceptometer is essentially one wire coil nesting in another, the coils are made from very thin copper wires with insulating coating, and the wires are glued together by stycast 1266 epoxy. During the measurement, a small AC current is applied to one of the coils, the driving coil, to generate a small AC magnetic field to the sample. The other coil, which is the pick-up coil, will sense the AC magnetic field generated by the sample and generate an induced AC voltage proportional to the susceptibility of the sample. There will be a background from the AC field generated by driving coil due to the non-zero mutual inductance between the coils, but we are looking for a sudden jump in the signal caused by superconducting transition, so this background is not very important. The top surface of the crystal is measured by Sagnac and needs to stay clean and open to light, and the susceptometer needs to be as close as possible to the crystal to maintain high sensitivity due to the small area of pick-up coil, so the susceptometer is put under the crystal inside the sample gap, touching the bottom of sample, a small droplet of GE varnish is used to glue the susceptometer to the titanium frame of the strain cell, maintaining its position at low temperature when strain is applied, as shown in Fig. 4.6.

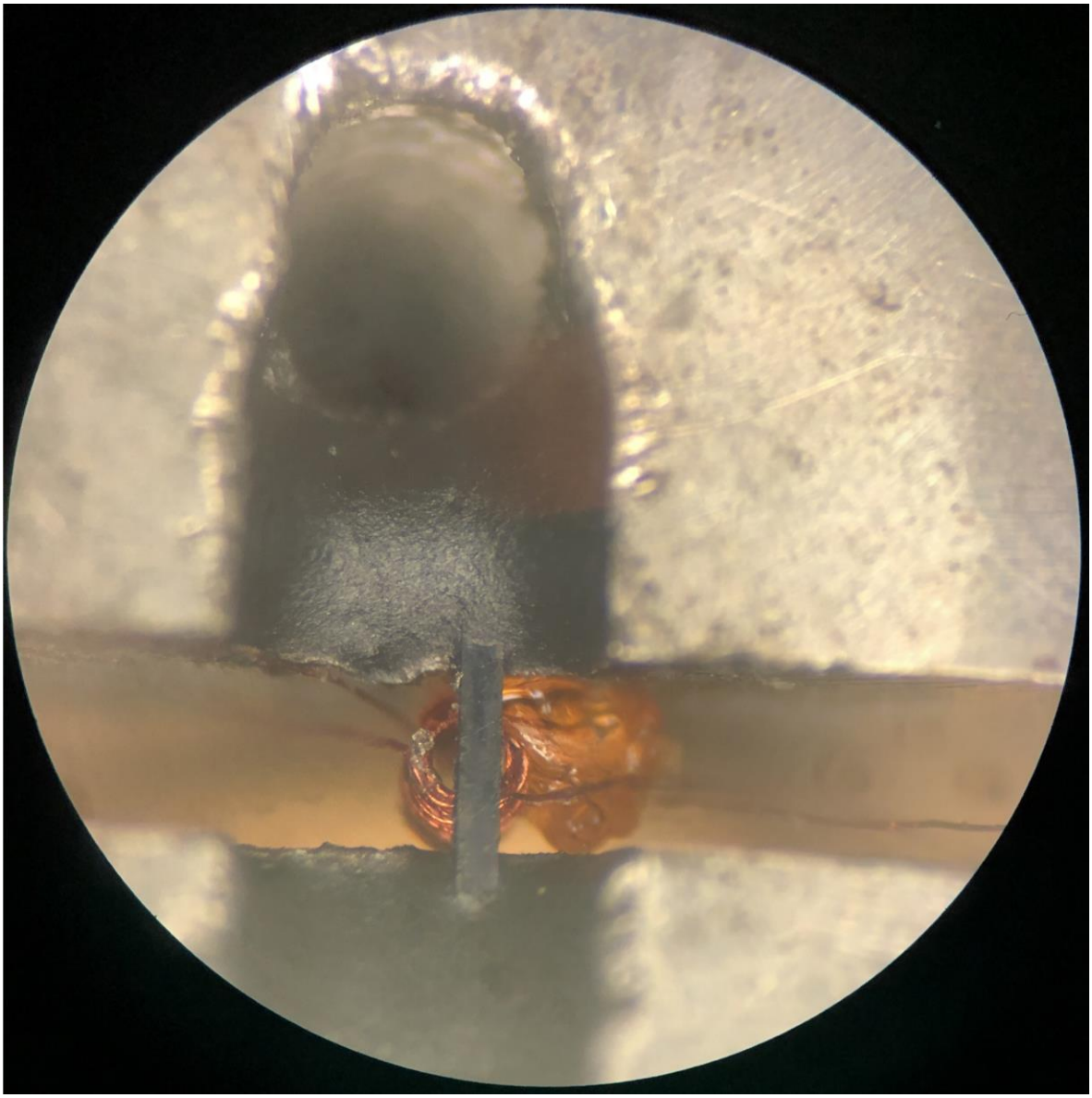

Fig. 4.6: Picture of a Sr_2RuO_4 crystal mounted in strain cell, with susceptometer mounted under it. A drop of GE Varnish is used to glue the susceptometer to the strain cell to maintain its position. The gap width is about 0.7 mm.

In the AC susceptibility measurements, there is a real component and an imaginary component, measured by the in-phase and out-of-phase component of the AC voltage induced on the pick-up coil. The real component represents the DC susceptibility of the sample, or more precisely the slope of the M(H) curve of the material, at an external DC field H. The out-of-phase component of the AC susceptibility is associated with dissipative process in the material, in the case of a type-II superconductor near its transition temperature, energy dissipation is caused by the movement of vortices induced by external AC magnetic field. When temperature is further lowered below T_c, lower critical field is larger than the small AC magnetic field applied by the driving coil and no vortex will be induced, thus the energy dissipation will be reduced to zero. As a result, there will be a peak in the out-of-phase component of the AC susceptibility centered at the transition temperature, and a sharp drop in the in-phase component representing the onset of Meissner effect in the superconducting phase, both can be used as an indicator of the transition temperature.

Fig. 4.7 shows an AC susceptibility measurement taken on a thin Sr_2RuO_4 crystal mounted in the strain cell, with no strain applied. A strong superconducting transition is observed at about 0.3K, which is the transition of titanium frame of the strain cell; a weaker transition (mostly visible in the in-phase component) is the signal from Sr_2RuO_4 crystal, the crystal is very thin and narrow, so the signal is a lot weaker than the titanium, although the susceptometer is directly mounted to the bottom surface of the crystal. A measurement on a free-standing crystal with higher driving current is shown in Fig. 4.8; transition at 1.4K can be clearly observed in both components. The value of out-of-phase component is unbalanced at temperatures above and below the transition, indicating part of the in-phase component is mixed into the out-of-phase component, because the phase setting on lock-in amplifier is not properly calibrated. However, since both in-phase and

out-of-phase components are recorded, a rotation of the phase angle can always be added later during the data analysis to get the perfect looking figure.

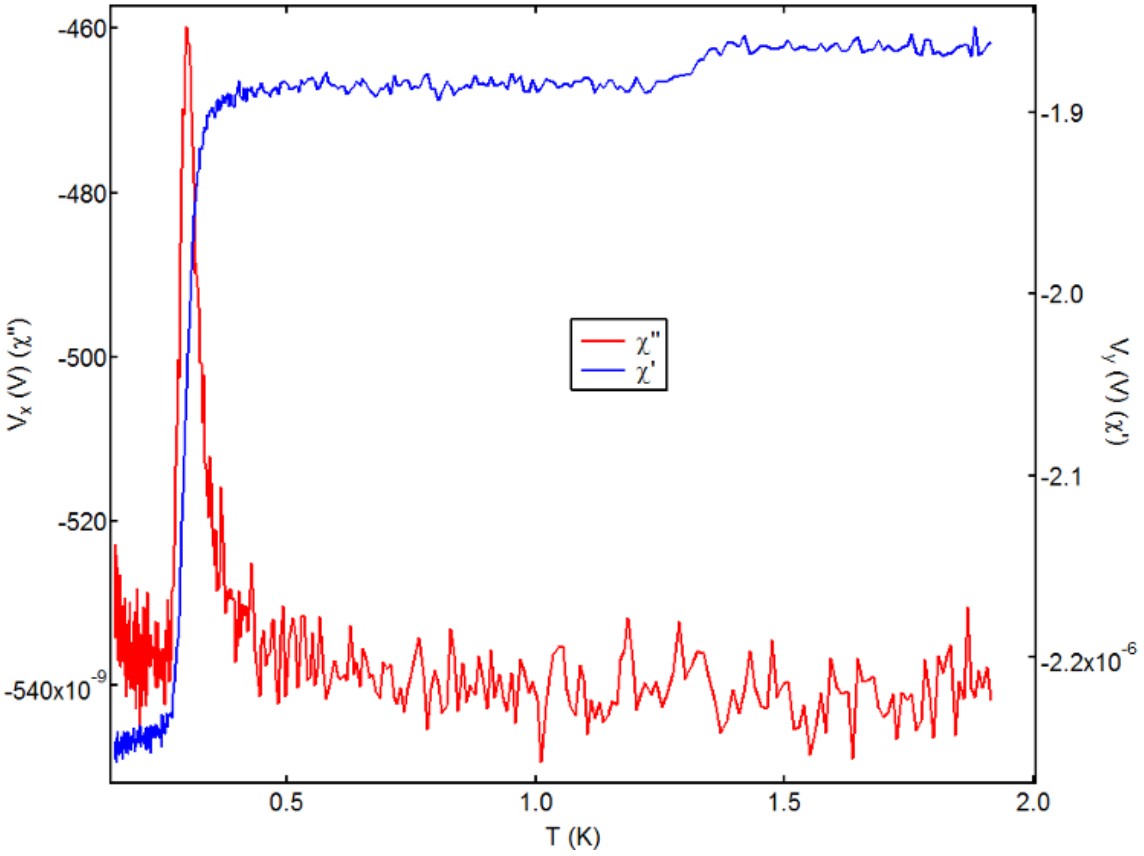

Fig. 4.7: AC susceptibility measured from a Sr_2RuO_4 crystal mounted in the strain cell, with cooling provided by the ADR unit. Strong transition at 0.3K is due to the surrounding titanium frame of the strain cell, transition of Sr_2RuO_4 can be observed in the in-phase component (blue).

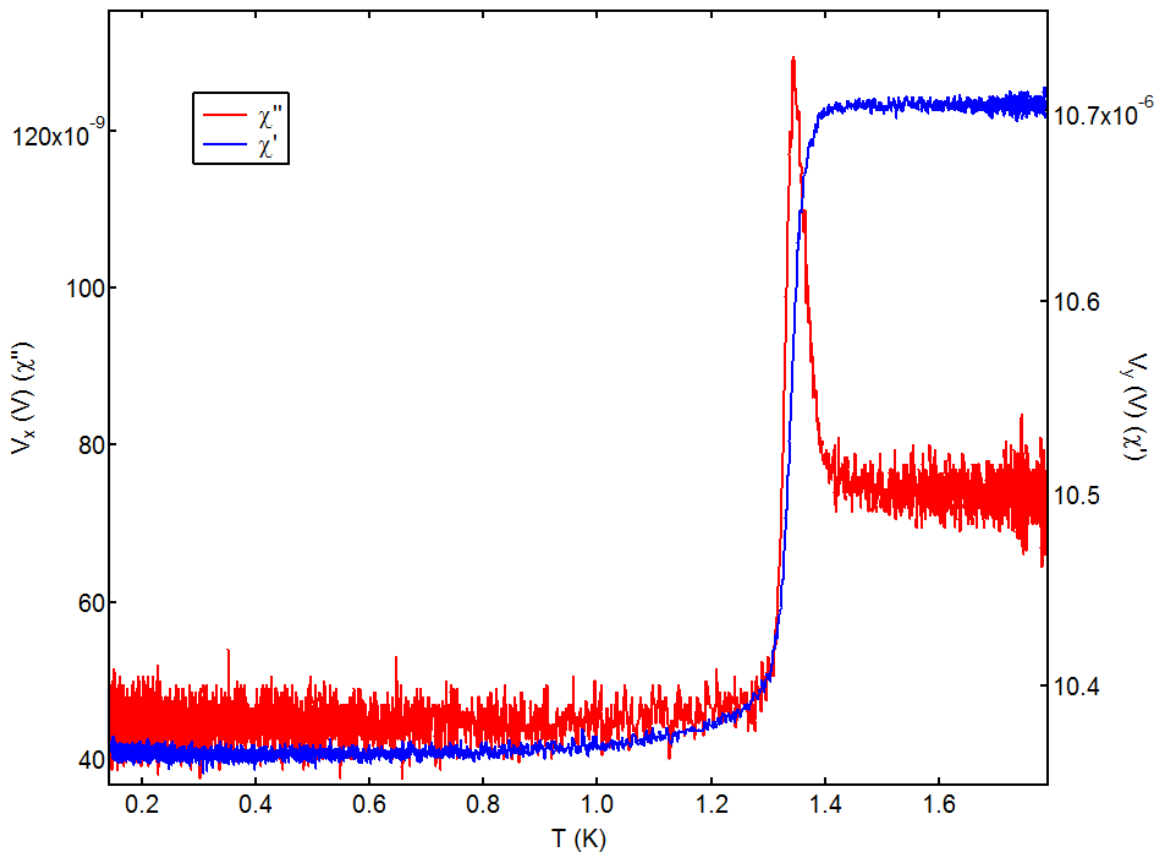

Fig. 4.8: AC susceptibility measured from a free-standing Sr_2RuO_4 crystal with higher driving current to enhance the signal intensity, with cooling provided by the ADR unit. Clear transition of Sr_2RuO_4 can be observed in both components. The difference in the out-of-phase component value well above and below transition is caused by the non-ideal setting of the phase angle of the lock-in amplifier, which can be corrected in the data analysis.

4.3 Experimental results

4.3.1 Sr_2RuO_4 under uniaxial strain

To achieve high enough strain to push the system beyond the Lifshitz transition, where the T_c reaches the maximum value 3.5K at 0.6% strain [45], thin plate-like samples are needed. In the most successful run, a crystal that is 0.3 mm wide and 0.05 mm thick was strained to near the Lifshitz transition with 450V applied to the middle piezo to compress the crystal. The two outer piezo are not activated to simpler the test since they do not provide as much displacement as the middle piezo because they are under negative voltage. The strain dependent in-phase component of AC susceptibility measurements is summarized in Fig. 4.9, demonstrating the evolution of enhanced superconducting phase. When strain value is increased, a broader transition is observed from the crystal, suggesting a strain induced inhomogeneous phase, agreeing with observations from other strain studies [46]. It is reported that the strain in the crystal has the maximum gradient at the two ends of the crystal, where it is connected to the epoxy; and a relative uniformly strained region can be realized in the middle of the crystal. Since our susceptometer covers about one half of the exposed area of the crystal centered at the middle of crystal, measured AC susceptibility represents an average of phases under different strain value, thus a broadened transition is expected when the strain value is approaching the peak value. When strain value is further increased, the transition is expected to become narrow again, due to the rapid decrease in T_c at higher strain. At applied voltage 425V and 450V, the onsets of superconducting temperature are both around 3.5K, the transition is broader for 425V compared to 450V, which indicates that at 450V, the majority of the crystal is strained over the Lifshiz

transition. The full voltage that can be applied at 2K is 600V, so this test is successful to show that the strain setup will allow us the study the full strain phase diagram of Sr_2RuO_4.

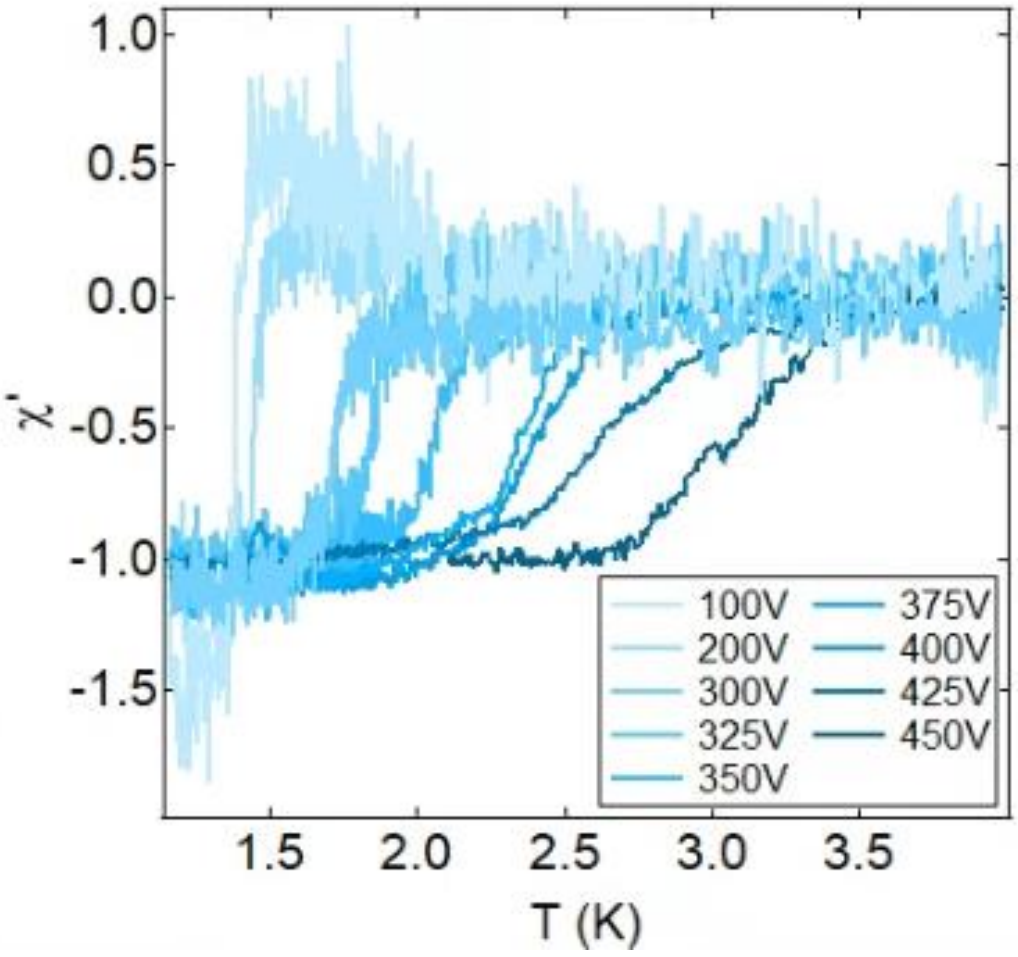

Fig. 4.9: AC susceptibility measured from strained Sr_2RuO_4 crystal at different strain value (labeled as voltage applied to piezo), with cooling provided by the ADR unit. Enhanced T_c along with broadened superconducting transitions are observed with increasing strain. Both 425V and 450V measurements give onset of transition at 3.5K, while the 450V measurement shows a narrower transition compared to 425V, indicating the system is strained across the Lifshitz transition.

After the successful tests of the cooling performance and strain ability of the full experimental setup, the last step is performing Sagnac measurements on the strain crystal. However, the heating effect from the laser is proved to be too strong for the ADR unit, a small power as small as 5 μW will heat up the whole unit in about 10 minutes, preventing any high precision measurements which usually requires hours of data averaging. To overcome the heating problem, the whole setup will need to be migrated into a dilution fridge, which does not require much creative work but is time-consuming. Hopefully this work will be finished in the future and help solve the mystery of Sr_2RuO_4.

4.3.2 Sr_2RuO_4-Ru eutectic phase

As described in the previous sections, the filamentary 3K phase of Sr_2RuO_4 is still a candidate for chiral triplet superconductor, the TRSB chiral order will emerge as a second phase transition inside the superconducting phase, indicated by an onset of zero bias conductance peak in the tunneling measurements, with a transition temperature around 2.4K. To test the theoretical picture of such chiral TRSB phase, MOKE measurements are performed using the PPMS 2K probe with piezo bimorph scanner described in the previous chapter. Scanning is needed for this measurement to make sure the light spot lands on the interface between Ru micro inclusion and bulk Sr_2RuO_4 crystal, where the enhancement of T_c happens.

According to theoretical predictions, the TRSB vector of the 3K-phase is likely pointing towards the z direction of the crystal. If this is the case, an onset of spontaneous Kerr signal should be resolved when the light incidents perpendicularly to the [001] surface (ab plane), and no such signal should be observed throughout the whole temperature range when light incidents to a

surface that is perpendicular to the ab plane, such as ac plane. Inspired by this, two 3K-phase samples are prepared, one has a polished ab plane and ac plane for the other one. Their microscopic pictures are shown in Fig. 4.10, both show smooth polished surfaces with nice Ru inclusions.

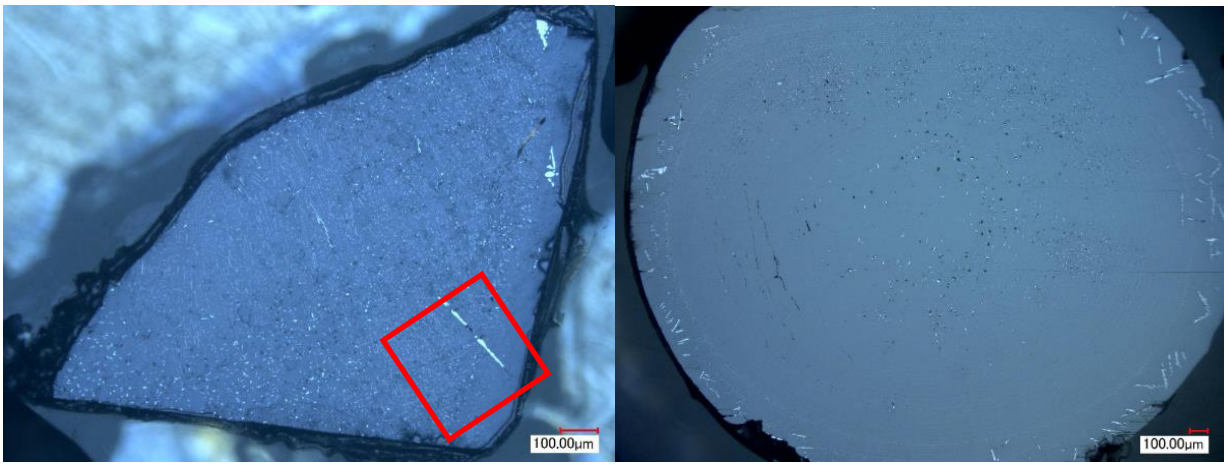

Fig. 4.10: Microscopic pictures of the two 3K-phase samples, with polished ab plane (left) and ac plane (right), small white spots are the Ru inclusions. The red box in the left picture indicates the area of scan shown in the next figure.

Location of the measurement is obviously very important for this project, to verify the location of the light spot, a room temperature scan is performed before cooling the sample. At room temperature the scanner has a large scan range of about 0.3 mm × 0.3 mm, the P_0 image of ab polished sample is shown in Fig 4.11, the X and Y axis are voltages applied to X and Y piezo, with a conversion rate of ~1V=1μm at room temperature. By comparing the scan image to the picture taken by microscope, the location of the light spot can be identified, marked by the red

box in Fig. 4.10 left panel. There is a significant difference in the ability to distinguish Ru from Sr_2RuO_4 between the optical microscope and Sagnac scanner. In the Fig. 4.11 lower panel, a microscopic picture with higher magnification taken on the area marked by the black box in the top panel is shown, many small Ru inclusions can be seen in this area, but such signature is not observed in the scan image taken by Sagnac interferometer. On the other hand, the very large Ru stripe is resolved in the scan image as low reflection stripes. This big difference in reflected power between the Sr_2RuO_4 and Ru cannot be explained by the difference in their optical reflection. At 1550 nm, the reflection of Sr_2RuO_4 is 0.8 [65], the value for Ru is 0.7 [66], this small difference cannot account for the 90% difference observed in the scan image, so we attribute the extremely low reflection from the big Ru stripe to the tilting of its surface orientation from the Sr_2RuO_4 surface, which could be introduced during the polishing. The absence of the small Ru micro inclusion in the scan image is likely due to the limit of spatial resolution, the lens used in this setup gives a light spot size in the order of 1 μm, making it hard to resolve those 1 μm wide small Ru inclusions. Due to this limited spatial resolution, we choose to measure the Sr_2RuO_4-Ru boundary at the big Ru stripe.

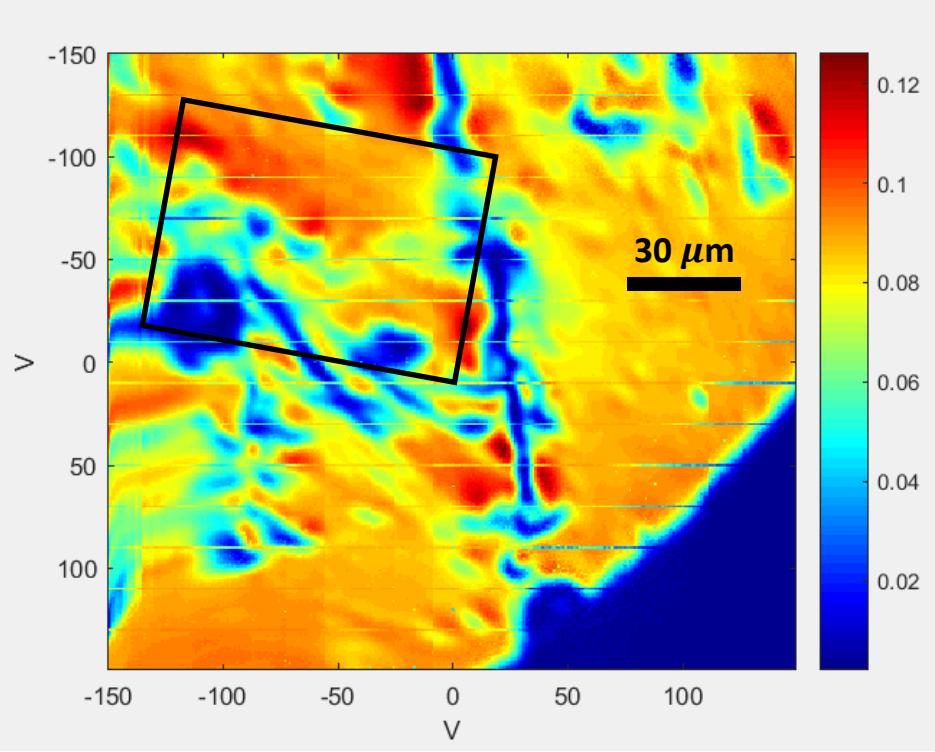

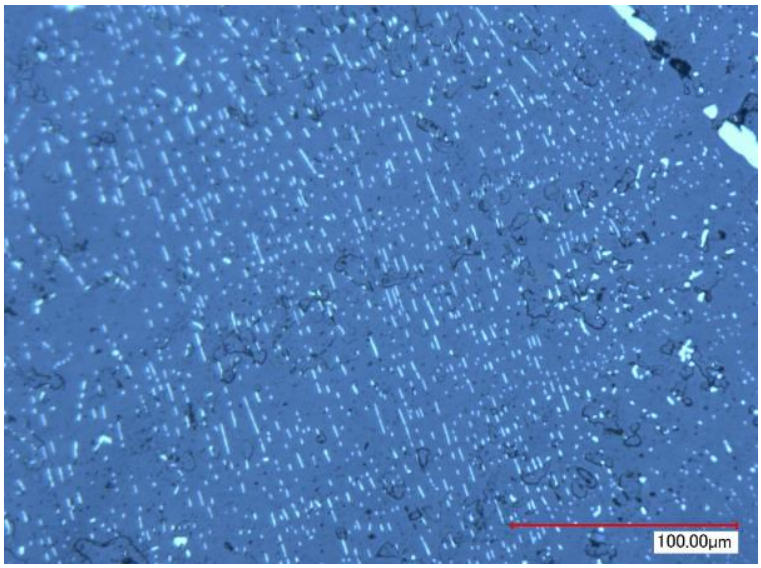

Fig. 4.11: Scan image (top) of the ab polished sample taken at room temperature, color scale indicates the DC power of the reflected light (P_0) at the measured spot. A picture taken by microscope showing an area marked by the black box in the top panel, showing many Ru inclusions in the area.

A scan image at 1.8K is shown in Fig. 4.12, the point of measurement is indicated by the black circle. Sample is cooled to base under +/-0.01T, then warmed up in zero field for the measurements. At the time of this project, the Sagnac system was noisy due to the construction activities in the building, so long-time averaged measurements are used. The field trained sample is warmed up from 1.8K to 3.3K in six steps with a separation of 0.3K between each step. A 2-hour measurement is taken at each temperature step to generate a single data point in the Kerr vs T figure. With such a long average time, most measurements are still noisy with the signal drifting randomly in the order of 100 nrad. Sr_2RuO_4 single crystal gives ~ 60 nrad Kerr signal in its superconducting phase, thus similar signal is expected from the 3K-phase superconductor, a background with 100 nrad drift is not ideal for this measurement, because the potentially 60 nrad onset will be combined with this 100 nrad random drift, distinguishing the real signal from the background is almost impossible. Nevertheless, we are still able to obtain two measurements that give the expected transition at 2.4K at the first glance, shown in Fig. 4.13. The top panel shows a zero-field warmup with +0.01T training field, an onset of Kerr signal at 2.4K is visible, the magnitude of this signal grows to 60 nrad at 1.8K. The lower panel is a zero-field trained zero-field warmup measurement, in this case the TRSB domains are expected to be randomly distributed, so the sign of the signal will be random, and its magnitude can be any value between zero to full value obtained in field trained measurements. Indeed, a -60 nrad onset of the signal starts at 2.4K if we ignore the 60 nrad ‘drift’ above 2.4K. This means that the light spot happens to land on a full TRSB domain with a negative signal, so the data looks like it is trained by negative field.

This looks promising at first glance, but we realized later that these two measurements cannot be evidence for a TRSB transition at 2.4K for several reasons. First, they are two measurements out

of more than ten others taken on the same spot, discarding the rest unwanted results will be cherry-picking. Second, as mentioned previously, the noisy apparatus does not give us the ability to distinguish true TRSB signal from background drift, a quieter measurement environment is needed. Third and most importantly, filamentary 3K-phase only exists at the Sr_2RuO_4-Ru boundary, with a characteristic width in the order coherence length (66nm) [67]. Even the few-micron-sized light spot lands right on top of a 3K-phase stripe, only a small portion of the light will reflect off from the 3K-phase region, while most of the light will still reflect from the surroundings of normal Sr_2RuO_4. Note that the separation between Ru stripes is typically 10 μm, so to cover multiple 3K-phase stripes with a single light spot is not possible. To obtain a 60 nrad signal, a pure 3K-phase superconductor needs to give a signal in the order of a few μrad, which is two orders of magnitude larger than the case for Sr_2RuO_4 and not very likely. In conclusion, a probe with high spatial resolution is needed to resolve the possible TRSB transition in the 3K-phase, and our result is not conclusive.

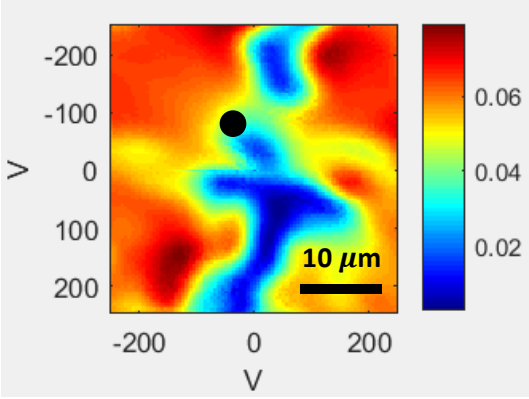

Fig. 4.12: Scan image at 1.8K, color scale represents the reflected DC power, point of measurement is indicated by the black circle.

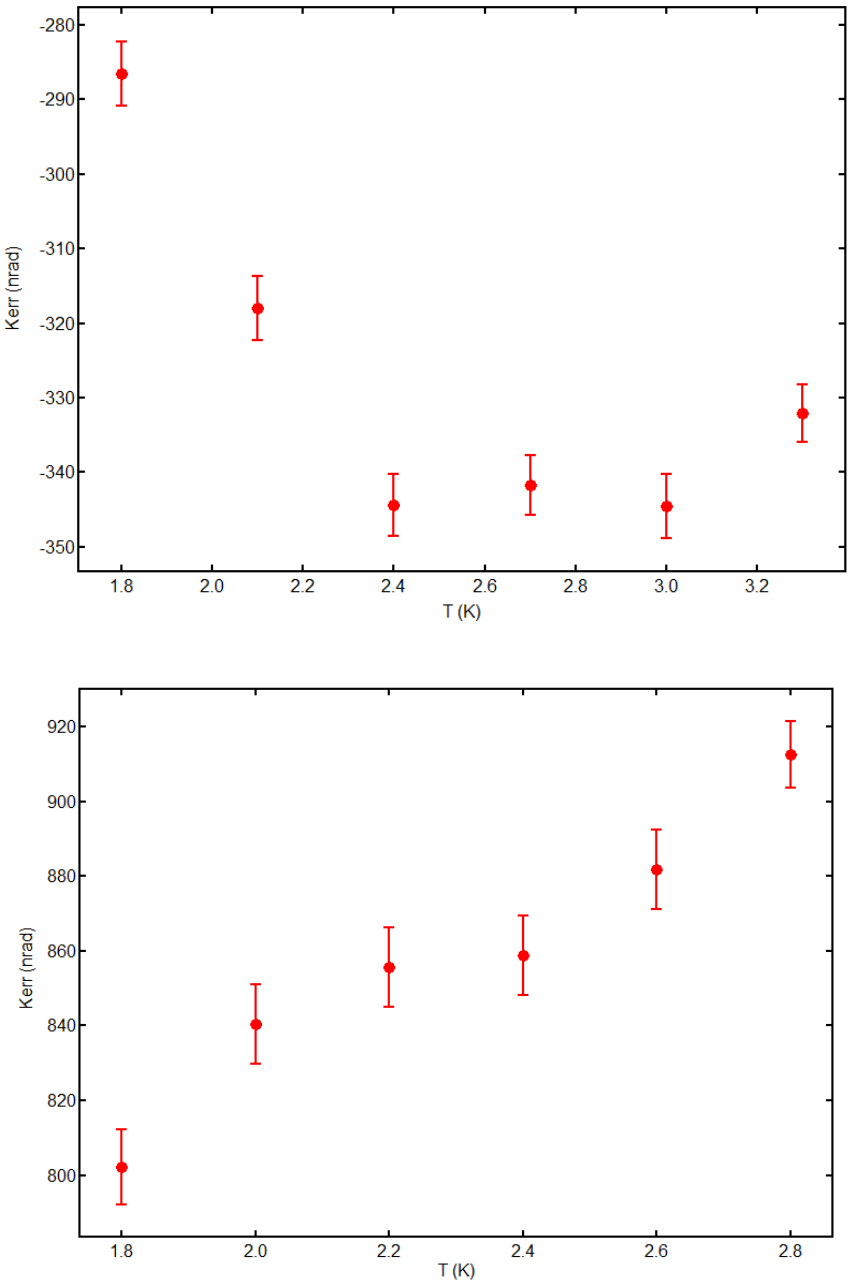

Fig. 4.13: Two measurements that show ‘transition-like’ signature at 2.4K. The top one is 0.01T trained, the bottom one is zero-field trained, both show onsets of 60 nrad signal. The interpretation of these two measurements is discussed in the main text.

4.4 Conclusion

In conclusion, MOKE measurements are performed on uniaxially strained Sr_2RuO_4 single crystal and 3K-phase Sr_2RuO_4. For strained Sr_2RuO_4, high resolution measurements cannot be achieved due to the short measurement time limited by the cooling method, a successful measurement can be carried out in the future in a dilution fridge where continuous cooling power is provided. For 3K-phase Sr_2RuO_4, the experimental results are not conclusive because the expected signal is extremely small, and it is beyond our resolution. Such a small expected signal is mainly due to the limited spatial resolution of our setup, if the spatial resolution is enhanced by using a lens with larger numerical aperture and light with shorter wavelength, the detection of the small expected Kerr signal from the 3K-phase Sr_2RuO_4 may be possible. A better way to characterize 3K-phase Sr_2RuO_4 would be using scanning probe microscopy such as STM or scanning near-field optical microscopy.

Unconventional superconductors are a group of fascinating materials that exhibit novel phenomena and constantly challenge the existing theory and refresh our understandings of physics. Among them, Sr_2RuO_4 stands as one of the most mysterious. After three decades of research, the debate on the physics in Sr_2RuO_4 is still ongoing and new discoveries [68] are still made from this old superconductor that was discovered in the year of my birth. Although no useful experimental results have been obtained during my 2.5-year studying on Sr_2RuO_4, I still consider it as a valuable experience that teaches me how to conduct research and more importantly, how messy (in a good way) the experimental results on a material can be. I hope one day the mystery of Sr_2RuO_4 will be solved and I will still be actively engaged in research when that day arrives.

Chapter 5

CsV_3Sb_5

5.1 Introduction

5.1.1 Charge density wave

In a normal metal, the charge distribution in real space is periodic, with the sample translational symmetry as the crystal lattice. This is because according to Bloch's theorem, the wavefunction of an electron in a periodic potential is Bloch function $\psi_k = e^{i\vec{k}\cdot\vec{r}}u(\vec{r})$, where $u(\vec{r})$ is a periodic function with the same periodicity as the crystal, and $e^{i\vec{k}\cdot\vec{r}}$ is just a phase factor depends on the crystal momentum $\vec{k}$. The charge distribution is the square of the modulus of the wavefunction, which stands for the possibility of finding an electron at location $\vec{r}$, multiplied by the electron charge e, so the charge distribution naturally inherits the periodicity of the lattice. In some metals, when temperature is lowered below a critical point, a spatial modulation of the charge density will happen, known as the charge density wave (CDW) transition. The modulation breaks the translational symmetry of the original charge distribution with a new periodicity that is larger than the old one. The redistribution of charge modifies the Coulomb potential felt by the ions in the lattice and causes a distortion of lattice structure when the ions move to their new lowest energy position. It is pointed out that at the transition temperature, charge modulation and lattice distortion happen simultaneously, so a distinction between charge density wave and lattice distortion is meaningless [69].

The driving mechanism for a charge density wave transition is complicated and shows a strong system dependence. The first attempt to explain charge density wave was made by Peierls when he was writing a textbook [70]. Peierls showed that for 1D atomic chain with one electron per lattice site, there is always an instability in the electronic band structure. The band structure of the 1D atomic chain with lattice constant a is shown in Fig. 5.1, the system is at half filling, so the Fermi surface locates at $k_F = \frac{\pi}{2a}$, the middle of the first Brillouin zone. If the atoms come into pairs and thus the lattice constant is doubled to $2a$, the size of the first Brillouin zone will be reduced to half and the Fermi wavevector is now at the Brillouin zone boundary, where an energy gap naturally opens after the lattice reconstruction and lowers the total energy of the electrons. Peierls proved that the energy gain here in the electronic band modification is always larger than the energy cost to reconstruct the lattice, thus for a 1D system there should always be a CDW transition accompanied with a metal-insulator transition. This is the so-called Peierls instability that describes an instability in the lattice structure caused by an instability in electronic band structure. The Peierls instability is essentially an effect of Fermi surface nesting. In one dimension, the Fermi surface is just two symmetric point in the Brillouin zone, there is always a 'nesting vector' that maps one Fermi surface to the other, the system can always lower its energy by modulating the lattice according to the Fourier transform of the nesting vector in real space to reduce the Brillouin zone size and put Fermi wavevector to the new Brillouin zone boundary. Such perfect nesting is only possible in one dimension, because the Fermi surface in 2D and 3D systems are closed loops/surfaces, a single vector cannot map one half of them to the other half. In the case that a large portion of the Fermi surface is nested by a single vector, or nesting between van Hoff singularities that host large density of states, a CDW transition can be driven in 2D or 3D systems accompanied by gap opening in the nested part of Fermi surface. To

determine the CDW transition temperature in the Peierls picture, one can look at the phonon dispersion of the system. The zero energy electronic excitations at the nesting vector will strongly screen lattice motion at this vector, causing a strong decrease in the phonon energy at the nesting vector. This temperature dependent phonon softening due to the Fermi surface nesting is known as the Kohn anomaly [71], when the phonon energy reaches zero, the CDW transition will occur.

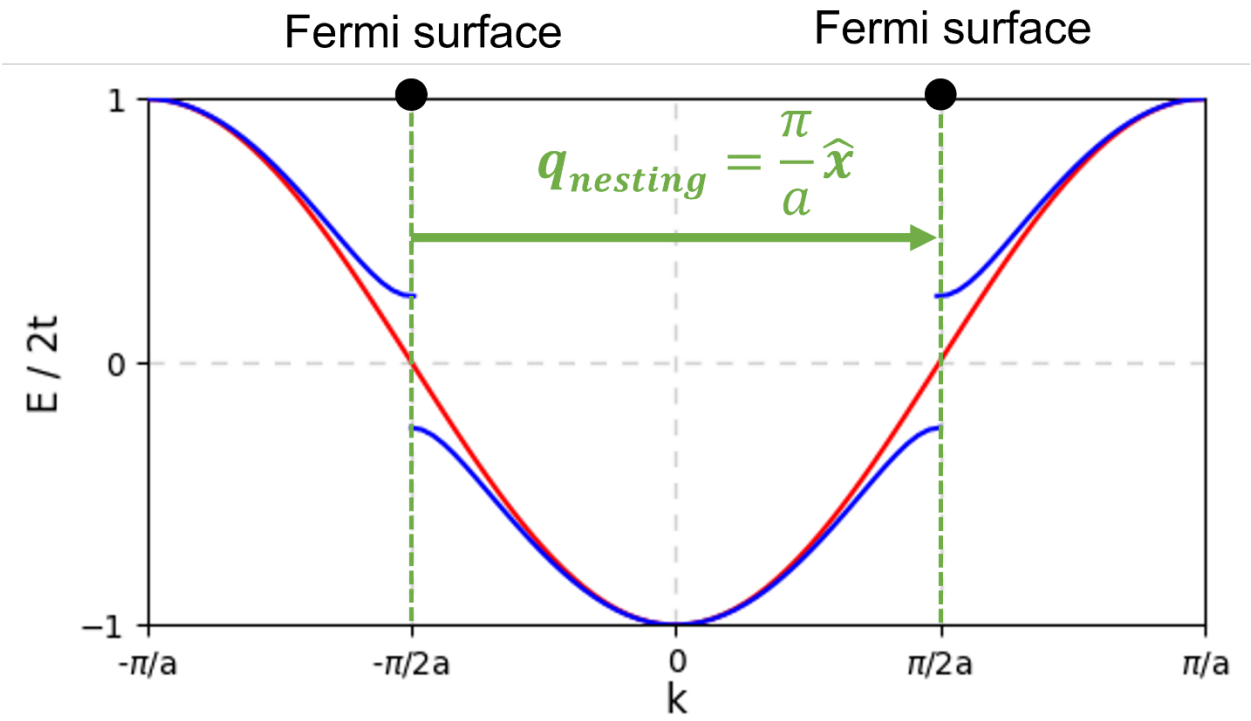

Fig. 5.1: The Peierls instability in 1D atomic chain. Red line indicates the band structure of a 1D atomic chain at half filling, the Fermi surface locates at $k = \pm\frac{\pi}{2a}$, the system is metallic. When atoms come into pairs, the Brillouin zone width is reduced to half and a gap is opened at the new Brillouin zone boundary which is also the Fermi surface, the CDW transition is thus accompanied by a metal-insulator-transition in the Peierls picture.

Another mechanism that can cause a CDW transition is the electron-phonon interaction, a strong wavevector dependent electron-phonon interaction can induce phonon mode softening at certain wavevector and causes the CDW transition. In such a case a metal-insulator transition is not necessary and there may not be an anomaly in the resistivity at the transition temperature. A well-established example of the electron-phonon interaction driven CDW is $NbSe_2$ [72,73].

While both the mechanisms mentioned involve electron-phonon interaction, it is natural to think about the effect of electron-electron interaction on the CDW transition. Indeed, there are some experimental evidence [74] to show that the CDW and charge ordering phase in high T_c cuprates are closely related to the antiferromagnetism and Coulomb interaction in those strongly correlated systems.

Both $NbSe_2$ and cuprates have a superconducting ground state at lower temperature, hinting a CDW phase may help and compete with the formation of a superconducting phase. Although lacking theoretical establishments, charge ordered phases are sometimes found above T_c in superconductors, and we shall see in the next section that the CDW phase in CsV_3Sb_5 is indeed intertwined with a superconducting ground state below 2K, making this newly discovered Kagome metal a very interesting playground to study complex phases.

5.1.2 CsV_3Sb_5

Kagome metals featuring elaborate lattice structures and rich varieties of quantum phenomena have stimulated intense experimental efforts to uncover novel phases of matter where strong correlation and topological orders intertwine, such as in the case of Chern topological magnet $TbMn_6Sn_6$ [75]. The recently discovered quasi-two-dimensional Kagome compound family AV_3Sb_5 (A=K, Rb and Cs) [76,77] is of great current interest due to its exhibition of charge

density wave [78–82] and pressure-tunable superconductivity [83–86]. Evidence for a TRSB order parameter in the CDW state has been reported in some of the μSR [87–89], STM [90,91], transport on strain-free micro crystal [92] and magneto-optic Kerr effect experiments [93–95]. The TRSB charge order may have connections with the long-sought loop currents that was originally proposed for cuprate superconductors [96]. AV_3Sb_5's rich phase diagrams originate from the ideal Kagome network governed by layers of vanadium and antimony intercalated by alkali metal ions that crystallize in the p6/mmm group: tight-binding models of such Kagome lattices have revealed a fascinating electronic band structure containing Dirac cones, flat bands, and Van Hove singularities [97], making AV_3Sb_5 an interesting platform with intertwined electronic instabilities for exotic correlated phases [98].

The driving mechanism of the CDW phase in CsV_3Sb_5 is still under debate. Theoretical calculations of the phonon dispersion found negative phonon energy at M point in the Brillouin zone, indicating phonon softening at this wavevector and a lattice instability [99]. The origin of this phonon softening is attributed to Fermi surface nesting, because the wavevector of the soft phonon mode at M point coincides with the nesting vector between van Hove singularities. By opening a gap at M point at the CDW transition, the density of states at Fermi level is lowered and the van Hove singularity is strongly suppressed. This picture quantitatively agrees with the fact that there is no metal-insulator transition but just a kink in the resistivity at the CDW transition [77], which indicates the Fermi surface is only partially gapped out. However, anomaly in the acoustic phonon dispersion at the CDW wavevector is not observed in X-ray diffraction, pointing to a unconventional CDW order mediated by electron-electron interaction [81]. ARPES [100] measurements provide a different insight into the origin of CDW in the sister compound KV_3Sb_5. A momentum-dependent gap opening is observed at transition temperature,

and possible Fermi surface nesting vectors based on the measured band structure do not agree with the CDW wavevector, weakening the role of Peierls instability in the formation of CDW. The measured band structure highly matches with the theoretical calculation that does not include any electronic correlation, suggesting very weak electron-electron interaction in the system and thus also does not support the electronic interaction driven CDW picture. The authors concluded that the CDW is likely to be induced by electron-phonon coupling, whose effect on the band structure is directly observed.

In this chapter I will describe our comprehensive MOKE study on CsV_3Sb_5, the one-sentence conclusion is that there is no onset of spontaneous Kerr signal at the CDW transition temperature, but this does not rule out the possible TRSB CDW phase that hosts a loop current.

The motivation of this project is mainly due to the contradictory experimental results in the MOKE measurements. The first report [93] of MOKE measurements on CsV_3Sb_5 used angle-dependent polarization rotation measurements to determine the Kerr rotation. This rather traditional method sends a linearly polarized light beam to the sample and measures the angle-dependent polarization rotation in the reflected light. When the polarization axis of the incident light changes, the polarization rotation in the reflected light also changes because there are two contributions to polarization rotation upon reflection. The first contribution is the Kerr effect which rotates the light by a constant angle that is only dependent on the sample's magnetic moment but independent of the polarization axis of the incident light. The second contribution is caused by linear birefringence that is anisotropic and depends on the relative angle between the polarization axis of the incident light and the principal axis of the crystal. The polarization rotation from birefringence has a period of π, it maximizes when the polarization of incident light is perpendicular to the principal axis and minimizes to zero when the incident light is

polarized along the principal axis. Thus, when the angle dependent polarization rotation is measured from a sample, the Kerr rotation can be extracted from the data as a constant term in the total polarization rotation that is independent of the angle. By doing so the authors observed an onset of spontaneous Kerr rotation at CDW transition in the zero field warmup measurements, the signal grows gradually in the CDW phase and reaches 45 μrad at 2K. Domains with different values of Kerr rotation are observed in the scan image, the Kerr rotation can be either positive or negative or close zero in different domains, and the domain boundaries are unaffected by thermal cycles. The authors also claim the sign of the Kerr rotation can be flipped by flipping the training field applied during cooldown. This result is repeated by another group [94], but in this report the Kerr rotation at low temperature is 450 μrad, 10 times larger than the first report. Both MOKE measurements using polarization rotation method used 800 nm light.

The first report of MOKE measurements using Sagnac interferometry is made by a group at Kyoto university [95]. They used the exact same setup as in our lab, using infrared light centered at 1550 nm. Similar results are claimed in the Kyoto paper, they observe an onset of spontaneous MOKE that grows to 2 μrad at base temperature, and the sign of the Kerr signal can be trained by external field. A strong sample dependence of their measurements is reported, only one out of three samples they measured showed a positive result, while the other two samples give no spontaneous Kerr effect. In contrast to the Kyoto result, a later paper by UCI and Stanford using the same method reported no sign of Kerr signal with an upper bound of 50 nrad. Since the experimental method used in these two reports are almost identical, sample dependence and small discrepancies in the experimental details are suspected to cause contradictory results. In the UCI and Stanford study the sample is provided by the UCSB group which discovered the

AV_3Sb_5 compound, while the Kyoto group used a sample from a different source. A few possible causes of the discrepancy are raised by the Kyoto group after communicating with us.

1. Sample needs to be trained in a high field to show a spontaneous Kerr signal in zero field warmups, in the first UCI and Stanford report the highest training field used was 0.34T, while for the Kyoto paper they went as high as 10T.
2. Sample needs to be cooled and warmed very slowly to avoid potential effect that kills the TRSB signature, we are suggested to use a thermal ramp rate no faster than 0.3K/min.
3. Sample dependence, the Kyoto group provided us with the only sample they had that gives a positive result to let us test it with our apparatus.

All these three assumptions have been tested, and the results will be presented and discussed in later sections.

5.2 Experimental setup

Two types of experimental setups are used in this project. For the measurements that require high field up to 9T, the setup is the PPMS insertion probe described in the previous two chapters. It is called cryo-optics setup in this chapter to be distinguished from the other setup used. For the low field measurements with higher Kerr resolution and scanning range, an older setup is used where the optics are put outside of a 2K cryostat, and light is focused through an optical window on the cryostat, this will be referred to as ‘ambient optics’ setup. The optics are mounted on a CONEX-AGP linear piezo translational stage that provides 27 mm range motion in the X and Y directions at any temperature. A picture of the setup is shown in Fig. 5.2.

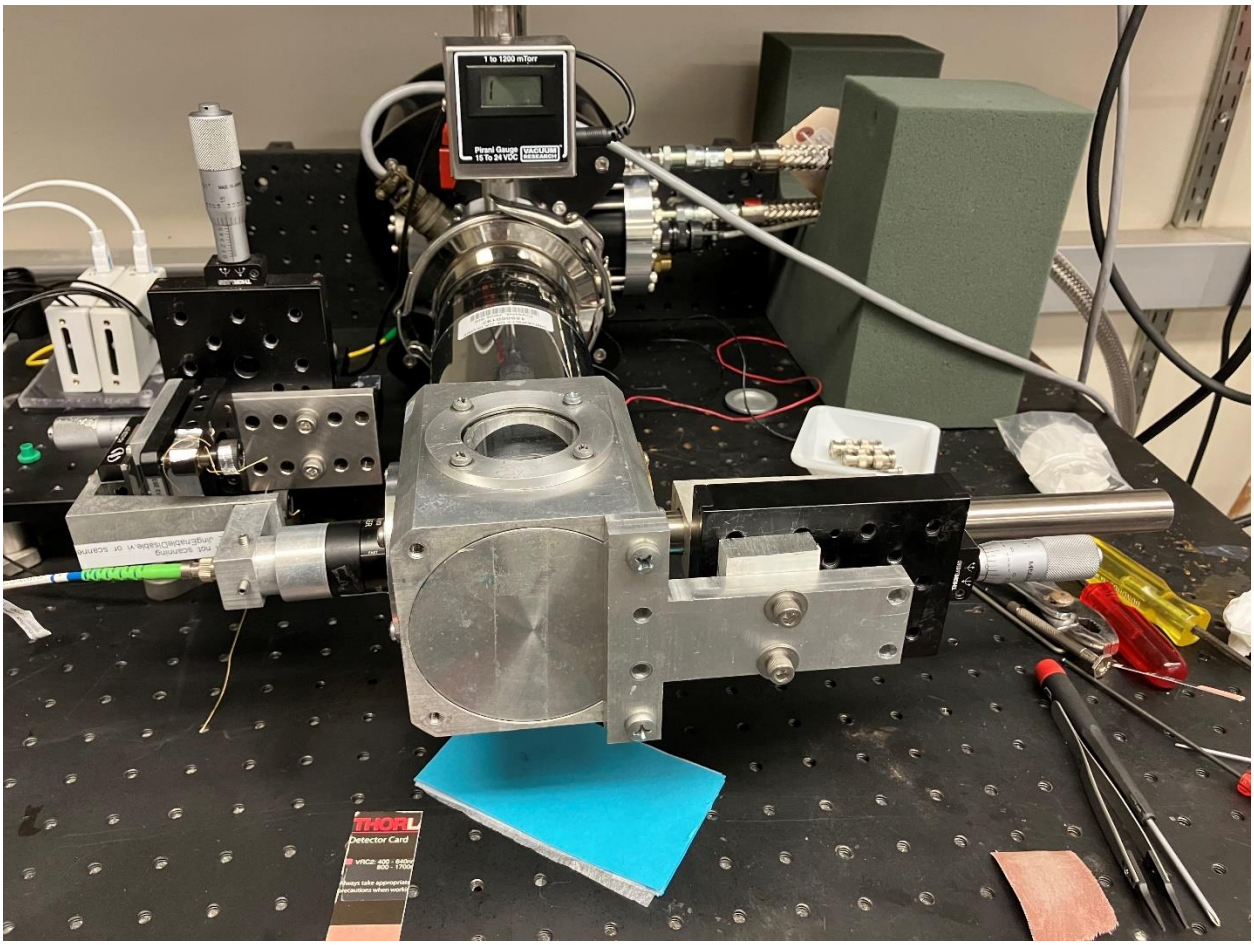

Fig. 5.2: Experimental setup for the ambient-optics setup, the optics are outside the cryostat, enabling large scanning range at low temperatures and giving stable background contributions because the optics are at constant temperature and not in field.

CsV_3Sb_5 crystals are very thin, soft plates. Like $NiBi_3$, it has a curvy surface so reflective areas are not easily accessible, and so scanning is needed to locate smooth areas for measurements. A picture of the UCSB sample used in this study is shown in Fig. 5.3.

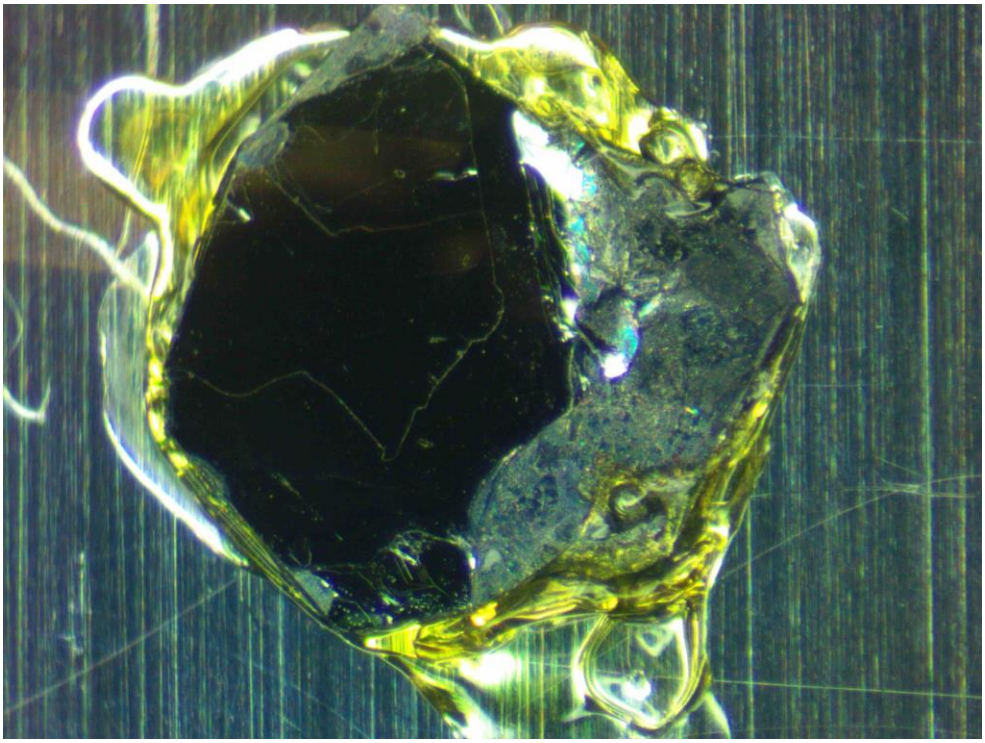

Fig. 5.3: Picture of the UCSB CsV_3Sb_5 sample used in this study. The smooth but curvy surface in the center of the black area is used for MOKE measurements.

5.3 Results and discussion

5.3.1 Measurements in magnetic field

We first conducted measurements in magnetic fields. The data are summarized in Fig. 5.4 for both UCSB sample and Kyoto sample, plotted as normalized Kerr signal (Kerr rotation divided by magnetic field) versus temperature. In the cryo-optics data, there is a large background contribution due to the Faraday effect from the optics in magnetic field, in the order of 100 μrad/T. This unwanted background is temperature dependent, making it not possible to precisely extract the temperature evolution of the Kerr signal in the sample when measured in external magnetic field. The thermal link between the cryo-optics and sample stage is relatively weak in the PPMS probe, so the temperature of the optics always deviates from the reading of the PPMS, which only measures the temperature of the sample stage. Such deviation depends on various parameters including the thermal history, thermal ramp rate and the helium pressure in the PPMS sample chamber, which strongly affects the thermal link between PPMS and the optics. Even when all these parameters are set to be the same, the temperature evolution of this Faraday background is still not repeatable, there will always be a few μrad/T difference between each identical run. Based on this, we make no quantitative analysis on the temperature dependent Kerr signal shown in Fig. 5.4, but rather focus on the anomaly at the CDW transition temperature. A consistent 5 μrad/T drop in the Kerr signal is observed in both samples at all fields, this could be caused by a reduction in the magnetization in the CDW phase, a change in the Kerr rotation to magnetization ratio due the reconstructed electronic band, or both. To the first order, we attribute this reduction in Kerr signal to the reduction of Pauli paramagnetic susceptibility in the CDW phase, which is caused by a decrease in the density of states at the Fermi level due the gap

opening, supported by the experimental evidence. The reduction in magnetic susceptibility is also observed in direct measurements [77] which serves as another support for our theory. Another feature in the field measurement data is that all curves roughly overlap with each other, if the small offset between each curve is neglected. This suggests there is no sign of magnetic hysteresis up to 9T in our measurements, agrees with the μSR results that detected no long-range order, a detailed interpretation will be given in the discussion.

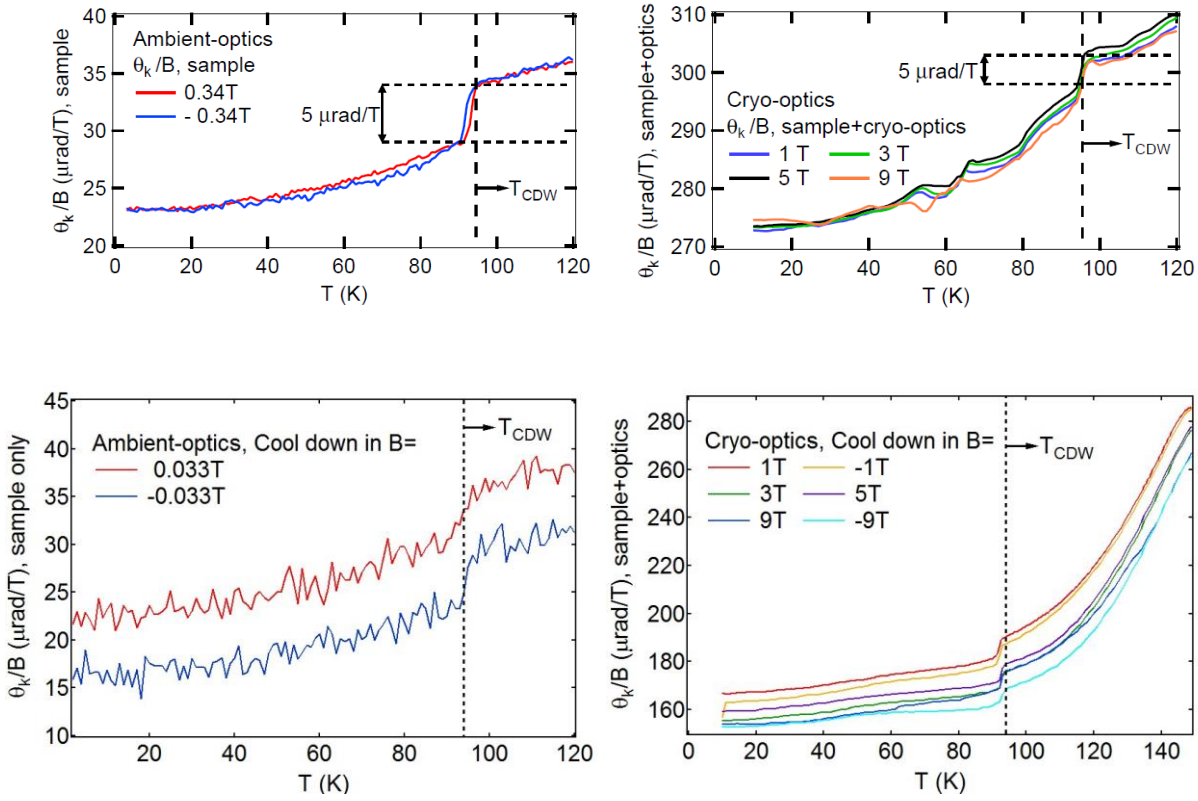

Fig. 5.4: Temperature dependence of Kerr rotation in magnetic field, measured with either ambient-optics (left) or cryo-optics (right) setup, for UCSB sample (top) and Kyoto sample (bottom). The Kerr rotations are scaled by external field applied, all curves overlap with each other, indicating no hysteresis up to 9T. A 5μrad/T drop is observed at CDW transition, which is attributed to the reduction in DOS at Fermi level due to gap opening.

5.3.2 Measurements in zero field with field training

Next, we performed field trained zero field warmup measurements on both samples to look for any onset of spontaneous Kerr signal in the CDW phase. All other MOKE measurements reported an onset of Kerr signal at the CDW transition, where for the μSR papers the onset temperature of TRSB signal can be at CDW transition or below CDW transition near 30K, and multiple transitions are reported in some of the μSR papers. For both samples, the highest trained field is 9T, which is the max we can do with the PPMS probe. The data are presented in Fig. 5.5, it is clear that no Kerr signal is resolved in all measurements, although some curve shows a drift in the order of ~ 200 nrad for the full temperature range of measurements, such as the black and purple curve (both +5T trained) in the UCSB sample data, the direction of drifting is random and not related to training field, so these drifting data do not represent a real Kerr signal but must be an artifact caused by the apparatus. If we compare our data to the Kyoto data presented in their paper, it is clear that our data has a lot more data points and a much better resolution even though our measurements are affected by the cryo-optics setup which introduces additional sources of noise. The high field trained data here rule out the possibility of the high-training-field induced spontaneous Kerr signal proposed by the Kyoto group. However, as they pointed out later to us, a recent theoretical study [101] could explain the discrepancy between our measurements. The theory showed that there may be two competing CDW orders in the system, the TRS invariant order is favorable in zero external field, while the TRSB order gets enhanced quickly when external field is turned on and can be the dominant CDW phase at even small external field. The Kyoto measurements are performed in an old cryostat which according to them sometimes gives a large remnant field in the order of a few tens of Gauss to 100 Gauss, while at UCI our cryostat does not have this problem, so the ‘zero-field’ measurements performed at Kyoto may actually

be ‘small-field’ measurements, where a TRSB order could be induced by the remnant field and causes the signal they observed. The magnitude of this ‘small’ external field to induce a TRSB order is unknow because it strongly depends on the parameters of the real materials, the authors of this theoretical work told me they think 1T would be a reasonable value to try in experiment, but they cannot make a definite statement. To test for the small-field induced spontaneous Kerr signal, we performed measurements using the ambient-optics setup with $\pm$ 330G applied to the sample, the data is included in Fig. 5.4. Like other measurements in field, the small field measurements showed reduction in Kerr signal below the transition, the magnitude of the drop scales well with any other higher field measurements, and no onset (increase) in Kerr signal is observed, thus we conclude that the small field induced spontaneous Kerr signal picture is also not supported by our measurements.

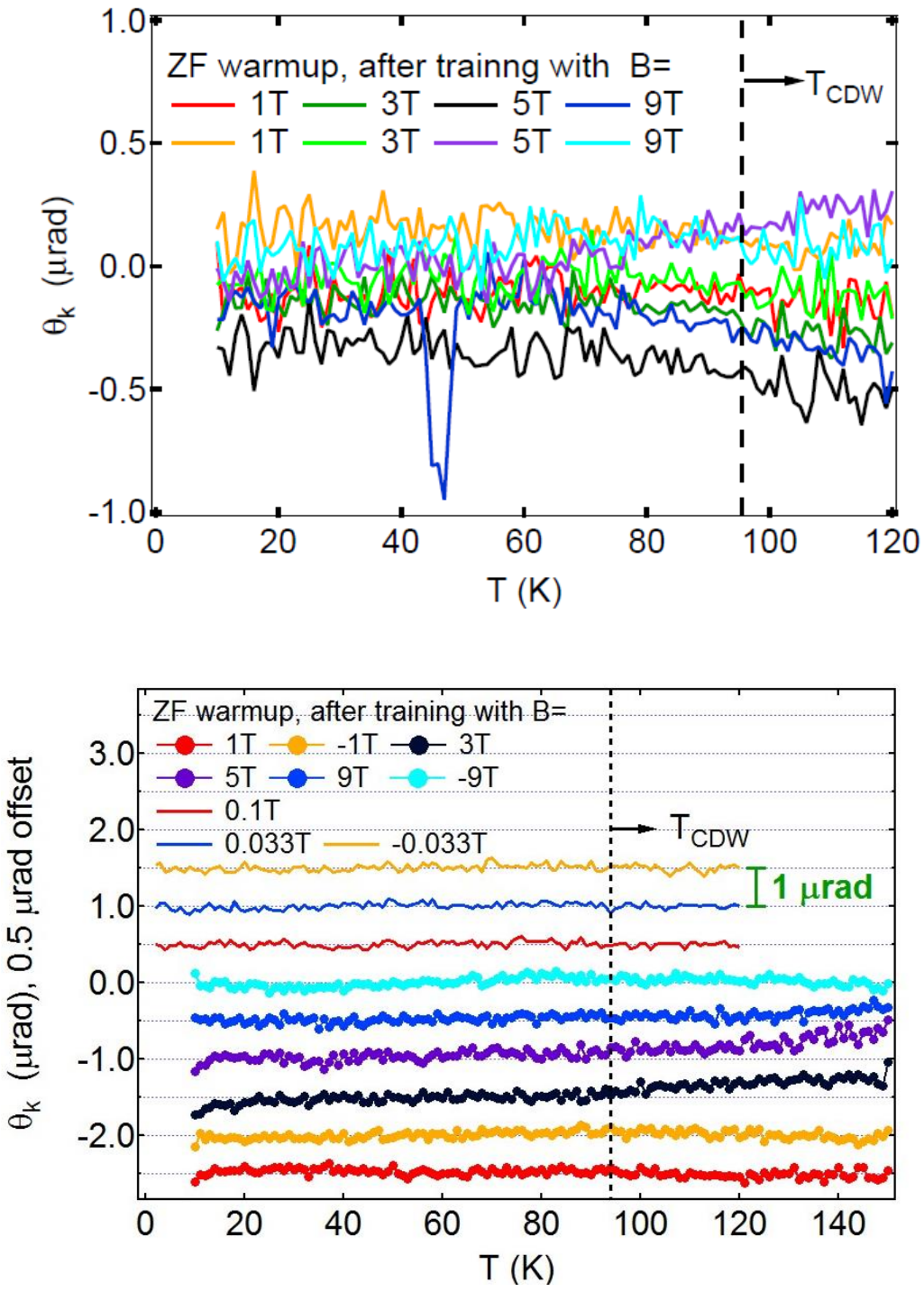

Fig. 5.5: Field-trained zero field warmup measurements, data obtained from UCSB sample (top) and Kyoto sample (bottom). No onset of spontaneous Kerr signal is observed within 100 nrad uncertainties, with training field up to 9T.

The slow warmup rate induced spontaneous Kerr signal theory has also been tested. Fig. 5.6 showed field trained zero field warm up measurements at various training fields with two warm up rates, 1K per minute and 0.3K per minute, as suggested by the Kyoto group. No difference is observed between measurements taken with different warm up rates; all measurements again give no onset of Kerr signal across the CDW transition with a resolution of 100 nrad.

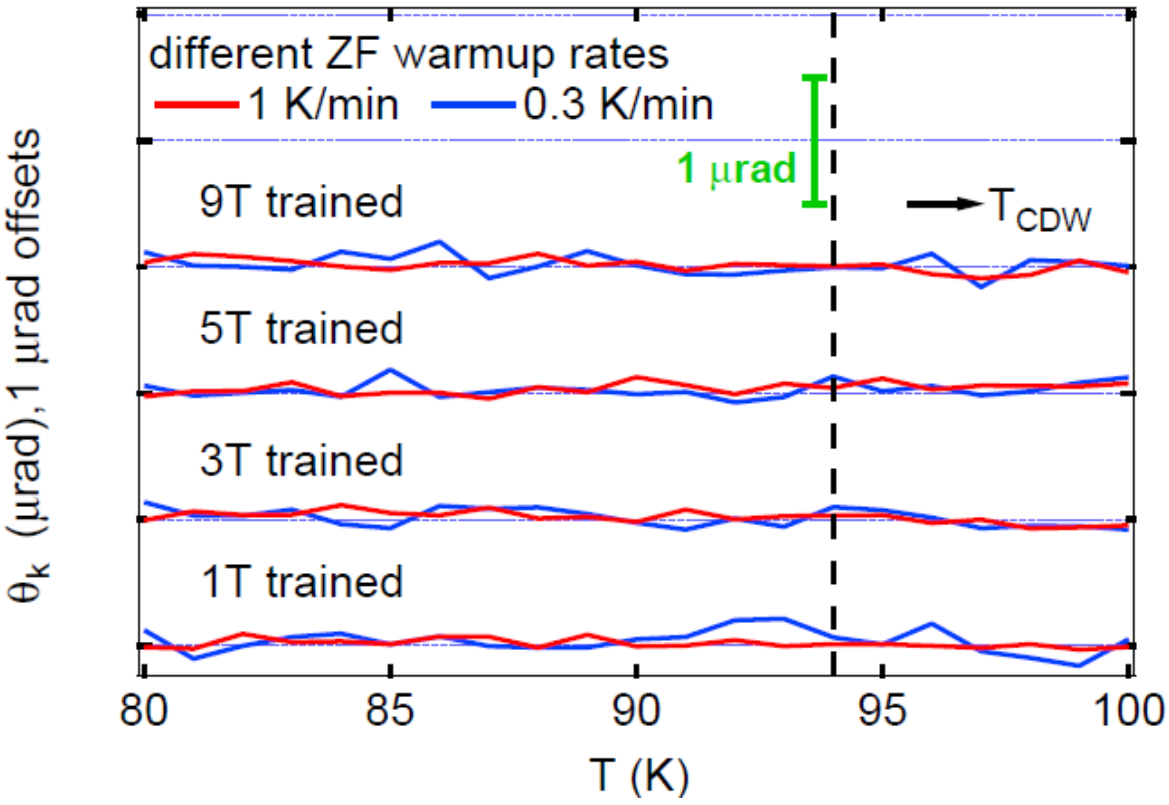

Fig 5.6: Field trained measurements with different warmup rates, up to 9T training field used. No difference is visible between the two sets of measurements, ruling out the thermal ramp rate induced TRSB scenario.

5.3.3 Spatial inhomogeneity

Finally, a test for spatial inhomogeneity has been made. A recent transport experiment [92] showed signatures of chiral transport that can be flipped by external field, the authors emphasized that low-strain environment is crucial to realize such chiral transport signature that evidence a TRSB charge order. They had to etch their crystal into 100 μm sized hall bar device using focused ion beam lithography and put the device on top of a conductive micro-spring stage to perform transport measurements at extremely low strain environment. They claim any small strain would kill the TRSB signature in their data, and they demonstrated that stain could shift the CDW transition temperature and causes different orders in the CDW phase. Inspired by this, high resolution Kerr scans have been made in zero field at 2K and 120K, on the Kyoto sample. The 2K scans are made after cooling the sample in $\pm$0.34T and turn off field at 2K, the scan images are presented in Fig. 5.7. Within the 100 nrad resolution, no change in the Kerr signal is observed on any spot in the 1mm×0.75mm scan image, demonstrating a homogeneous zero-Kerr surface of the sample with no TRSB domains. This ruled out the case where in the Kyoto measurements their light spot landed on a strain-free area with TRSB order, while for all other measurements made by UCI and Stanford the measured area is strain full and non-TRSB.

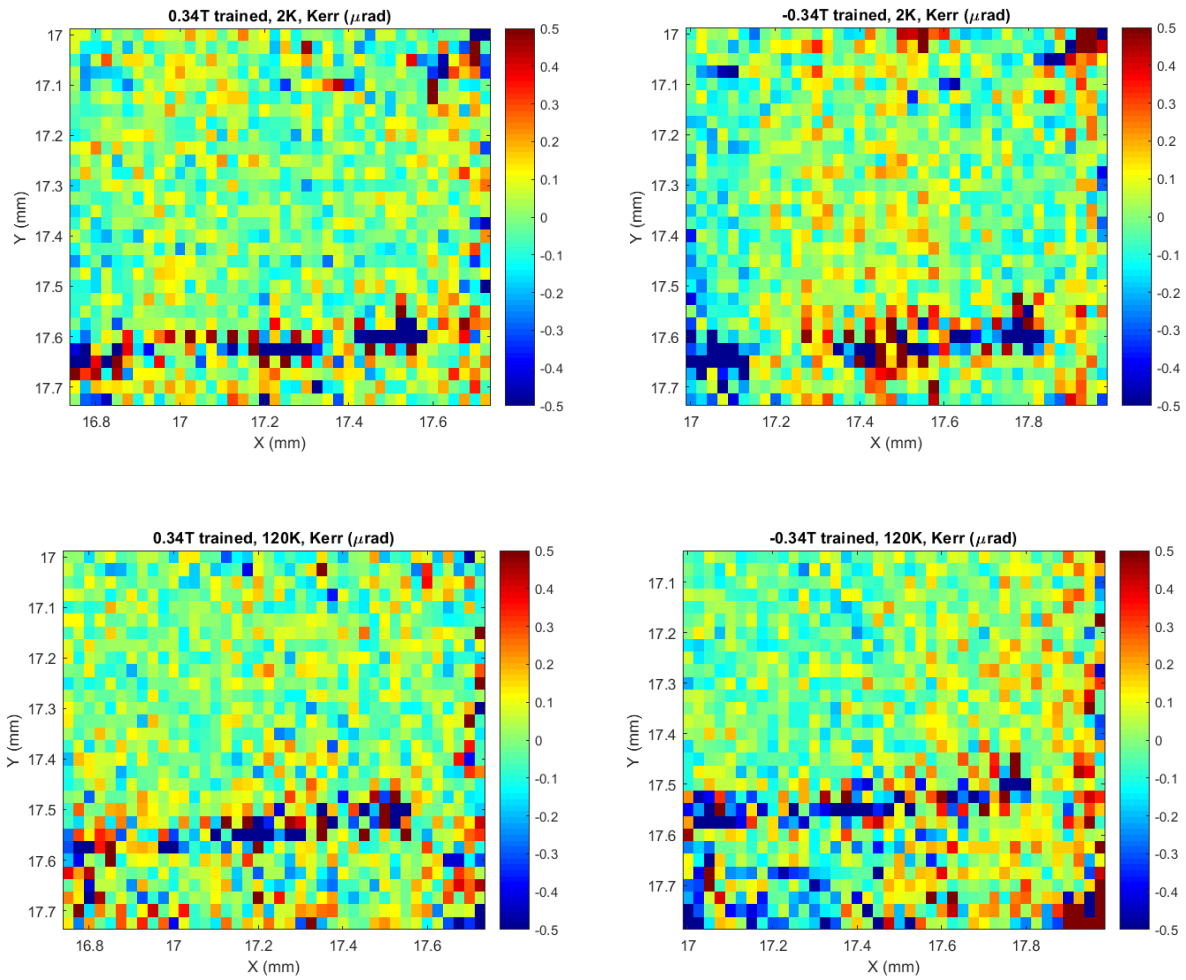

Fig. 5.7: Scanning Kerr image in zero field at 2K and 120K, after ±0.34T field training. Within the 100 nrad resolution, no change in the Kerr signal is observed on any spot, demonstrating a homogeneous zero-Kerr surface of the sample with no TRSB domains.

5.3.4 Discussion

TRSB in a CDW order is unconventional, CsV_3Sb_5 is not ferromagnetic, so the TRSB is likely due to orbital effect. Indeed, a chiral flux phase of CDW order is proposed [102], where loop current flows between lattices sites and the uneven magnitude of current breaks the original translational symmetry of the lattice and causes the charge modulation. In each layer of the CsV_3Sb_5, loop currents circulate in the ab plane, causing magnetic moment in the c direction of the crystal. Another possible competing CDW phase is a charge bound state, where different hopping strength between the lattice sites induced the CDW. The charge bond state does not break TRS but competes with the chiral flux phase because its energy is close to the chiral flux phase. There is a lot of experimental evidence for TRSB of the CDW phase, but the evidence is not fully consistent with each other. The μSR measurements report different onset temperatures of the TRSB order on CsV_3Sb_5, and two transitions are reported in some of the paper. For STM measurements, the signature of TRSB arises from a field-switchable chirality in the direction of counting from the lowest intensity CDW peak to the highest intensity peak in the Fourier transformed STM image. Such effect is observed in the defect free region of KV_3Sb_5 and RbV_3Sb_5 [90,91], although another STM study on KV_3Sb_5 [103] did not observe difference in the intensity of the CDW peaks, the intensity of the peaks also does not respond to external field. A STM study on CsV_3Sb_5 using spin-polarized tips [104] reports no sign of the chiral flux phase, making the interpretations of STM studies more complicated. Recent micro-transport study also found evidence for TRSB in the field-switchable chiral transport measurements, the authors stated that the TRSB phase is very sensitive to strain and can only be observed in low strain samples. This may explain the discrepancies in other measurements, where the TRSB order emerges at different temperatures and different regions in the samples.

Putting all this in mind, our measurements put some additional constraints on the properties of this presumably existed TRSB CDW. Our measurements detect the averaged Kerr signal in a volume at sample surface, its volume can be estimated by the area of the light spot times penetration depth of the light, usually in the order of cubic micron. This means that sample with no net magnetic moment will give zero Kerr signal, although TRSB is still possible in the system such as an antiferromagnet. There are two scenarios that can mediate the existence of chiral flux phase and the absence of Kerr effect:

1. In each layer, the net magnetic moment is zero, the clockwise loop current and counterclockwise loop current generate equal amount of magnetic moment and cancel each other out exactly in each layer. This is not very likely because as illustrated in Fig. 6.8, the area for the two types of current loops is not the same, to cancel out their moment the current needs to be precisely adjusted according to the effective loop area.
2. A non-zero net moment is generated by each layer, but the interlayer coupling is antiferromagnetic-like, so the maximum net moment in a macroscopic volume of measurement is provided by a single layer of the material, which is too small to be detected. In this scenario, the interlayer coupling must be very strong because up to 9T field applied along c axis, the moments are not flipped at all, otherwise we should observe some sign of hysteresis in our in-field measurements, but for both sample the in-field data scales linearly with respect to the external field up to 9T.

Finally, the discrepancy between other MOKE measurements using polarization rotation method should be explained. Polarization rotation measurements are performed at UCI at 1550 nm, surprising there is indeed an onset of large isotropic polarization rotation below the CDW transition, in the order of mrad [105]. However, this isotropic polarization rotation cannot be

detected by the Sagnac interferometer, and the sign of this polarization rotate cannot be flipped by external field but can be different between samples. The intuitive interpretation of this is that such polarization rotation is related to some novel effect that does not break TRS. But as explained in Chapter 2, the Sagnac interferometer is sensitive to antisymmetric off diagonal elements of the dielectric matrix, which can only happen when TRS is broken. A symmetric off diagonal term will also rotate the polarization of light but does not contribute to Kerr rotation, because they can always be reduced to zero when the coordinates are properly chosen, this also suggests that the polarization rotation caused by symmetric off diagonal terms must be angle dependent, which contradicts to what has been observed here. Nevertheless, such an effect could in principle explain why the polarization rotation method will detect a 'false' Kerr signal, although discrepancies still exist in the field response of this isotropic, 'non-TRSB' polarization rotation. Further investigations and additional careful measurements are needed for this discovery.

5.4 Conclusion

In conclusion, we performed a high-precision, comprehensive MOKE study on the Kagome metal CsV_3Sb_5, two samples from different sources have been tested, no different results are observed from the two samples. For the measurements in magnetic fields, a B-linear 5μrad/T drop in the Kerr signal is observed for all values of applied field, from 0.033T to 9T. The absence of magnetic hysteresis up to 9T indicates the absence of magnetic order in the system, or a very robust interlayer antiferromagnetic order that does not flip in 9T external field. For the zero field measurements, no spontaneous Kerr signal is observed in the CDW phase down to temperature above superconducting transition, with training field as large as 9T. Spatial inhomogeneity has also been tested, uniform zero Kerr signal is observed from a 1 mm×0.75

mm area on the field-trained sample, indicating no inhomogeneous TRSB domains within our resolution. An absence of spontaneous Kerr effect is a result of zero net magnetic moment but not a directly evidence of TRS invariance, it can be explained by the loop current picture where interlayer antiferromagnetically coupled orbital moments cancel each other out, leaving zero net moment and thus zero Kerr effect. We argue that our results do not rule out the theoretically proposed loop current phase but put strong constraints on the magnetic properties of this phase.

Bibliography

[1] J. S. Dodge, L. Klein, M. M. Fejer, and A. Kapitulnik, *Symmetry of the Magneto-Optic Response of the Sagnac Interferometer*, J. Appl. Phys. **79**, 6186 (1996).

[2] Z. Q. Qiu and S. D. Bader, *Surface Magneto-Optic Kerr Effect*, Review of Scientific Instruments **71**, 1243 (2000).

[3] *The Faraday Effect in Ferromagnetics*, Proc. R. Soc. Lond. A **135**, 237 (1932).

[4] P. N. Argyres, *Theory of the Faraday and Kerr Effects in Ferromagnetics*, Phys. Rev. **97**, 334 (1955).

[5] C. Kittel, *Domain Boundary Motion in Ferroelectric Crystals and the Dielectric Constant at High Frequency*, Phys. Rev. **83**, 458 (1951).

[6] J. Xia, P. T. Beyersdorf, M. M. Fejer, and A. Kapitulnik, *Modified Sagnac Interferometer for High-Sensitivity Magneto-Optic Measurements at Cryogenic Temperatures*, Appl. Phys. Lett. **89**, 062508 (2006).

[7] S. Spielman, K. Fesler, C. B. Eom, T. H. Geballe, M. M. Fejer, and A. Kapitulnik, *Test for Nonreciprocal Circular Birefringence in $YBa_2Cu_3O_7$ Thin Films as Evidence for Broken Time-Reversal Symmetry*, Phys. Rev. Lett. **65**, 123 (1990).

[8] S. Spielman, J. S. Dodge, L. W. Lombardo, C. B. Eom, M. M. Fejer, T. H. Geballe, and A. Kapitulnik, *Measurement of the Spontaneous Polar Kerr Effect in $YBa_2Cu_3O_7$ and $Bi_2Sr_2CaCu_2O_8$*, Phys. Rev. Lett. **68**, 3472 (1992).

[9] C. Nayak, S. H. Simon, A. Stern, M. Freedman, and S. Das Sarma, *Non-Abelian Anyons and Topological Quantum Computation*, Rev. Mod. Phys. **80**, 1083 (2008).

[10] J. S. Moodera and R. Meservey, *Superconducting Phases of Bi and Ga Induced by Deposition on a Ni Sublayer*, Phys. Rev. B **42**, 179 (1990).

[11] P. LeClair, J. S. Moodera, J. Philip, and D. Heiman, *Coexistence of Ferromagnetism and Superconductivity in Ni/Bi Bilayers*, Phys. Rev. Lett. **94**, 037006 (2005).

[12] X. Gong, M. Kargarian, A. Stern, D. Yue, H. Zhou, X. Jin, V. M. Galitski, V. M. Yakovenko, and J. Xia, *Time-Reversal Symmetry-Breaking Superconductivity in Epitaxial Bismuth/Nickel Bilayers*, Sci. Adv. **3**, e1602579 (2017).

[13] J. Wang et al., *Anomalous Magnetic Moments as Evidence of Chiral Superconductivity in a Bi/Ni Bilayer*, Phys. Rev. B **96**, 054519 (2017).

[14] P. Chauhan, F. Mahmood, D. Yue, P.-C. Xu, X. Jin, and N. P. Armitage, *Nodeless Bulk Superconductivity in the Time-Reversal Symmetry Breaking Bi/Ni Bilayer System*, Phys. Rev. Lett. **122**, 017002 (2019).

[15] G. J. Zhao, X. X. Gong, P. C. Xu, B. C. Li, Z. Y. Huang, X. F. Jin, X. D. Zhu, and T. Y. Chen, *Singlet Superconductivity in Single-Crystal $NiBi_3$ Superconductor*, (2018).

[16] J. Kumar, A. Kumar, A. Vajpayee, B. Gahtori, D. Sharma, P. K. Ahluwalia, S. Auluck, and V. P. S. Awana, *Physical Property and Electronic Structure Characterization of Bulk Superconducting Bi_3Ni*, Supercond. Sci. Technol. **24**, 085002 (2011).

[17] V. Siva, K. Senapati, B. Satpati, S. Prusty, D. K. Avasthi, D. Kanjilal, and P. K. Sahoo, *Spontaneous Formation of Superconducting $NiBi_3$ Phase in Ni-Bi Bilayer Films*, Journal of Applied Physics **117**, 083902 (2015).

[18] L. Y. Liu, Y. T. Xing, I. L. C. Merino, H. Micklitz, D. F. Franceschini, E. Baggio-Saitovitch, D. C. Bell, and I. G. Solórzano, *Superconductivity in Bi/Ni Bilayer System: Clear Role of Superconducting Phases Found at Bi/Ni Interface*, Phys. Rev. Materials **2**, 014601 (2018).

[20] S.-P. Chao, *Superconductivity in a Bi/Ni Bilayer*, Phys. Rev. B **99**, 064504 (2019).

[21] T. Herrmannsdörfer, R. Skrotzki, J. Wosnitza, D. Köhler, R. Boldt, and M. Ruck, *Structure-Induced Coexistence of Ferromagnetic and Superconducting States of Single-Phase Bi 3 Ni Seen via Magnetization and Resistance Measurements*, Phys. Rev. B **83**, 140501 (2011).

[22] X. Zhu, H. Lei, C. Petrovic, and Y. Zhang, *Surface-Induced Magnetic Fluctuations in a Single-Crystal $NiBi_3$ Superconductor*, Phys. Rev. B **86**, 024527 (2012).

[23] S. K. Chong et al., *Electrical Manipulation of Topological Phases in a Quantum Anomalous Hall Insulator*, Advanced Materials **35**, 2207622 (2023).

[24] B. Silva et al., *Superconductivity and Magnetism on Flux-Grown Single Crystals of $NiBi_3$*, Phys. Rev. B **88**, 184508 (2013).

[25] J. Xia, Y. Maeno, P. T. Beyersdorf, M. M. Fejer, and A. Kapitulnik, *High Resolution Polar Kerr Effect Measurements of Sr_2RuO_4: Evidence for Broken Time-Reversal Symmetry in the Superconducting State*, Phys. Rev. Lett. **97**, 167002 (2006).

[26] Y. Maeno, H. Hashimoto, K. Yoshida, S. Nishizaki, T. Fujita, J. G. Bednorz, and F. Lichtenberg, *Superconductivity in a Layered Perovskite without Copper*, Nature **372**, 532 (1994).

[27] J. Bardeen, L. N. Cooper, and J. R. Schrieffer, *Theory of Superconductivity*, Phys. Rev. **108**, 1175 (1957).

[28] N. P. Armitage, P. Fournier, and R. L. Greene, *Progress and Perspectives on Electron-Doped Cuprates*, Rev. Mod. Phys. **82**, 2421 (2010).

[29] D. A. Bonn, P. Dosanjh, R. Liang, and W. N. Hardy, *Evidence for Rapid Suppression of Quasiparticle Scattering below T_c in $YBa_2Cu_3O_{7-\delta}$*, Phys. Rev. Lett. **68**, 2390 (1992).

[30] A. Hosseini, R. Harris, S. Kamal, P. Dosanjh, J. Preston, R. Liang, W. N. Hardy, and D. A. Bonn, *Microwave Spectroscopy of Thermally Excited Quasiparticles in $YBa_2Cu_3O_{6.99}$*, Phys. Rev. B **60**, 1349 (1999).

[31] H.-Y. Choi, C. M. Varma, and X. Zhou, *Superconductivity in the Cuprates: Deduction of Mechanism for d-Wave Pairing through Analysis of ARPES*, Front. Phys. **6**, 440 (2011).

[32] A. P. Mackenzie, R. K. W. Haselwimmer, A. W. Tyler, G. G. Lonzarich, Y. Mori, S. Nishizaki, and Y. Maeno, *Extremely Strong Dependence of Superconductivity on Disorder in Sr_2RuO_4*, Phys. Rev. Lett. **80**, 161 (1998).

[33] P. W. Anderson, *Theory of Dirty Superconductors*, Journal of Physics and Chemistry of Solids **11**, 26 (1959).

[34] K. Ishida, H. Mukuda, Y. Kitaoka, K. Asayama, Z. Q. Mao, Y. Mori, and Y. Maeno, *Spin-Triplet Superconductivity in Sr_2RuO_4 Identified by ^{17}O Knight Shift*, Nature **396**, 658 (1998).

[35] J. A. Duffy, S. M. Hayden, Y. Maeno, Z. Mao, J. Kulda, and G. J. McIntyre, *Polarized-Neutron Scattering Study of the Cooper-Pair Moment in Sr_2RuO_4*, Phys. Rev. Lett. **85**, 5412 (2000).

[36] K. D. Nelson, Z. Q. Mao, Y. Maeno, and Y. Liu, *Odd-Parity Superconductivity in Sr_2RuO_4*, Science **306**, 1151 (2004).

[37] F. Kidwingira, J. D. Strand, D. J. Van Harlingen, and Y. Maeno, *Dynamical Superconducting Order Parameter Domains in Sr_2RuO_4*, Science **314**, 1267 (2006).

[38] K. Deguchi, M. A. Tanatar, Z. Mao, T. Ishiguro, and Y. Maeno, *Superconducting Double Transition and the Upper Critical Field Limit of Sr_2RuO_4 in Parallel Magnetic Fields*, J. Phys. Soc. Jpn. **71**, 2839 (2002).

[39] S. Yonezawa, T. Kajikawa, and Y. Maeno, *First-Order Superconducting Transition of Sr_2RuO_4*, Phys. Rev. Lett. **110**, 077003 (2013).

[40] G. M. Luke et al., *Time-Reversal Symmetry-Breaking Superconductivity in Sr_2RuO_4*, Nature **394**, 558 (1998).

[41] C. W. Hicks, J. R. Kirtley, T. M. Lippman, N. C. Koshnick, M. E. Huber, Y. Maeno, W. M. Yuhasz, M. B. Maple, and K. A. Moler, *Limits on Superconductivity-Related Magnetization in Sr_2RuO_4 and $PrOs_4Sb_{12}$ from Scanning SQUID Microscopy*, Phys. Rev. B **81**, 214501 (2010).

[42] J. R. Kirtley, C. Kallin, C. W. Hicks, E.-A. Kim, Y. Liu, K. A. Moler, Y. Maeno, and K. D. Nelson, *Upper Limit on Spontaneous Supercurrents in Sr_2RuO_4*, Phys. Rev. B **76**, 014526 (2007).

[43] P. J. Curran, S. J. Bending, W. M. Desoky, A. S. Gibbs, S. L. Lee, and A. P. Mackenzie, *Search for Spontaneous Edge Currents and Vortex Imaging in Sr_2RuO_4 Mesostructures*, Phys. Rev. B **89**, 144504 (2014).

[44] P. J. Curran, V. V. Khotkevych, S. J. Bending, A. S. Gibbs, S. L. Lee, and A. P. Mackenzie, *Vortex Imaging and Vortex Lattice Transitions in Superconducting Sr_2RuO_4 Single Crystals*, Phys. Rev. B **84**, 104507 (2011).

[45] C. W. Hicks et al., *Strong Increase of* T_c *of* Sr_2RuO_4 *Under Both Tensile and Compressive Strain*, Science **344**, 283 (2014).

[46] A. Steppke et al., *Strong Peak in* T_c *of* Sr_2RuO_4 *under Uniaxial Pressure*, Science **355**, eaaf9398 (2017).

[47] C. A. Watson, A. S. Gibbs, A. P. Mackenzie, C. W. Hicks, and K. A. Moler, *Micron-Scale Measurements of Low Anisotropic Strain Response of Local T c in* Sr_2RuO_4, Phys. Rev. B **98**, 094521 (2018).

[48] M. Sigrist, *Review on the Chiral* p -*Wave Phase of* Sr_2RuO_4, Prog. Theor. Phys. Suppl. **160**, 1 (2005).

[49] C. Kallin, *Chiral P-Wave Order in* Sr_2RuO_4, Rep. Prog. Phys. **75**, 042501 (2012).

[50] Y. Ueno, A. Yamakage, Y. Tanaka, and M. Sato, *Symmetry-Protected Majorana Fermions in Topological Crystalline Superconductors: Theory and Application to* Sr_2RuO_4, Phys. Rev. Lett. **111**, 087002 (2013).

[51] A. Pustogow et al., *Constraints on the Superconducting Order Parameter in* Sr_2RuO_4 *from Oxygen-17 Nuclear Magnetic Resonance*, Nature **574**, 72 (2019).

[52] K. Ishida, M. Manago, K. Kinjo, and Y. Maeno, *Reduction of the* ^{17}O *Knight Shift in the Superconducting State and the Heat-up Effect by NMR Pulses on* Sr_2 RuO_4, J. Phys. Soc. Jpn. **89**, 034712 (2020).

[53] A. N. Petsch, M. Zhu, M. Enderle, Z. Q. Mao, Y. Maeno, I. I. Mazin, and S. M. Hayden, *Reduction of the Spin Susceptibility in the Superconducting State of* Sr_2RuO_4 *Observed by Polarized Neutron Scattering*, Phys. Rev. Lett. **125**, 217004 (2020).

[54] S. Benhabib et al., *Ultrasound Evidence for a Two-Component Superconducting Order Parameter in* Sr_2RuO_4, Nat. Phys. **17**, 194 (2021).

[55] S. Ghosh, A. Shekhter, F. Jerzembeck, N. Kikugawa, D. A. Sokolov, M. Brando, A. P. Mackenzie, C. W. Hicks, and B. J. Ramshaw, *Thermodynamic Evidence for a Two-Component Superconducting Order Parameter in* Sr_2RuO_4, Nat. Phys. **17**, 199 (2021).

[56] V. Grinenko et al., *Split Superconducting and Time-Reversal Symmetry-Breaking Transitions in* Sr_2RuO_4 *under Stress*, Nat. Phys. **17**, 748 (2021).

[57] S. A. Kivelson, A. C. Yuan, B. Ramshaw, and R. Thomale, *A Proposal for Reconciling Diverse Experiments on the Superconducting State in* Sr_2RuO_4, Npj Quantum Mater. **5**, 43 (2020).

[58] A. T. Rømer, D. D. Scherer, I. M. Eremin, P. J. Hirschfeld, and B. M. Andersen, *Knight Shift and Leading Superconducting Instability from Spin Fluctuations in* Sr_2RuO_4, Phys. Rev. Lett. **123**, 247001 (2019).

[59] V. Grinenko, D. Das, R. Gupta, B. Zinkl, N. Kikugawa, Y. Maeno, C. W. Hicks, H.-H. Klauss, M. Sigrist, and R. Khasanov, *Unsplit Superconducting and Time Reversal Symmetry*

Breaking Transitions in Sr_2RuO_4 under Hydrostatic Pressure and Disorder, Nat Commun **12**, 3920 (2021).

[60] H. Kaneyasu, Y. Enokida, T. Nomura, Y. Hasegawa, T. Sakai, and M. Sigrist, *Properties of the H−T Phase Diagram of the 3−K Phase in Eutectic Sr_2RuO_4-Ru: Evidence for Chiral Superconductivity*, Phys. Rev. B **100**, 214501 (2019).

[61] H. Yaguchi, K. Takizawa, M. Kawamura, N. Kikugawa, Y. Maeno, T. Meno, T. Akazaki, K. Semba, and H. Takayanagi, *Spectroscopy of Sr_2RuO_4/Ru Junctions in Eutectic*, in *AIP Conference Proceedings*, Vol. 850 (AIP, Orlando, Florida (USA), 2006), pp. 543–544.

[62] Z. Q. Mao, K. D. Nelson, R. Jin, Y. Liu, and Y. Maeno, *Observation of Andreev Surface Bound States in the 3-K Phase Region of Sr_2RuO_4*, Phys. Rev. Lett. **87**, 037003 (2001).

[63] M. Kawamura, H. Yaguchi, N. Kikugawa, Y. Maeno, and H. Takayanagi, *Tunneling Properties at the Interface between Superconducting Sr_2RuO_4 and a Ru Microinclusion*, J. Phys. Soc. Jpn. **74**, 531 (2005).

[64] C. W. Hicks, M. E. Barber, S. D. Edkins, D. O. Brodsky, and A. P. Mackenzie, *Piezoelectric-Based Apparatus for Strain Tuning*, Review of Scientific Instruments **85**, 065003 (2014).

[65] D. Stricker, J. Mravlje, C. Berthod, R. Fittipaldi, A. Vecchione, A. Georges, and D. Van Der Marel, *Optical Response of Sr_2RuO_4 Reveals Universal Fermi-Liquid Scaling and Quasiparticles Beyond Landau Theory*, Phys. Rev. Lett. **113**, 087404 (2014).

[66] K. A. Kress and G. J. Lapeyre, *Optical Properties of Molybdenum and Ruthenium**, J. Opt. Soc. Am. **60**, 1681 (1970).

[67] Y. A. Ying, N. E. Staley, Y. Xin, K. Sun, X. Cai, D. Fobes, T. J. Liu, Z. Q. Mao, and Y. Liu, *Enhanced Spin-Triplet Superconductivity near Dislocations in Sr_2RuO_4*, Nat Commun **4**, 2596 (2013).

[68] K. Kinjo, M. Manago, S. Kitagawa, Z. Q. Mao, S. Yonezawa, Y. Maeno, and K. Ishida, *Superconducting Spin Smecticity Evidencing the Fulde-Ferrell-Larkin-Ovchinnikov State in Sr_2RuO_4*, Science **376**, 397 (2022).

[69] M. D. Johannes and I. I. Mazin, *Fermi Surface Nesting and the Origin of Charge Density Waves in Metals*, Phys. Rev. B **77**, 165135 (2008).

[70] R. E. Peierls, *Quantum Theory of Solids* (Oxford University, 1995).

[71] E. J. Woll and W. Kohn, *Images of the Fermi Surface in Phonon Spectra of Metals*, Phys. Rev. **126**, 1693 (1962).

[72] M. Calandra, I. I. Mazin, and F. Mauri, *Effect of Dimensionality on the Charge-Density Wave in Few-Layer 2H-$NbSe_2$*, Phys. Rev. B **80**, 241108 (2009).

[73] F. Weber, S. Rosenkranz, J.-P. Castellan, R. Osborn, R. Hott, R. Heid, K.-P. Bohnen, T. Egami, A. H. Said, and D. Reznik, *Extended Phonon Collapse and the Origin of the Charge-Density Wave in 2H−$NbSe_2$*, Phys. Rev. Lett. **107**, 107403 (2011).

[74] K. Fujita et al., *Direct Phase-Sensitive Identification of a* d *-Form Factor Density Wave in Underdoped Cuprates*, Proc. Natl. Acad. Sci. U.S.A. **111**, (2014).

[75] J.-X. Yin et al., *Quantum-Limit Chern Topological Magnetism in $TbMn_6Sn_6$*, Nature **583**, 533 (2020).

[76] B. R. Ortiz et al., *New Kagome Prototype Materials: Discovery of KV_3Sb_5, RbV_3Sb_5, and CsV_3Sb_5*, Phys. Rev. Materials **3**, 094407 (2019).

[77] B. R. Ortiz et al., *CsV_3Sb_5: A Z 2 Topological Kagome Metal with a Superconducting Ground State*, Phys. Rev. Lett. **125**, 247002 (2020).

[83] F. H. Yu, D. H. Ma, W. Z. Zhuo, S. Q. Liu, X. K. Wen, B. Lei, J. J. Ying, and X. H. Chen, *Unusual Competition of Superconductivity and Charge-Density-Wave State in a Compressed Topological Kagome Metal*, Nat Commun **12**, 3645 (2021).

[84] L. Zheng et al., *Emergent Charge Order in Pressurized Kagome Superconductor CsV_3Sb_5*, Nature **611**, 682 (2022).

[85] F. Du, S. Luo, B. R. Ortiz, Y. Chen, W. Duan, D. Zhang, X. Lu, S. D. Wilson, Y. Song, and H. Yuan, *Pressure-Induced Double Superconducting Domes and Charge Instability in the Kagome Metal KV_3Sb_5*, Phys. Rev. B **103**, L220504 (2021).

[86] N. N. Wang et al., *Competition between Charge-Density-Wave and Superconductivity in the Kagome Metal RbV_3Sb_5*, Phys. Rev. Research **3**, 043018 (2021).

[87] R. Khasanov et al., *Time-Reversal Symmetry Broken by Charge Order in CsV_3Sb_5*, Phys. Rev. Research **4**, 023244 (2022).

[88] C. Mielke et al., *Time-Reversal Symmetry-Breaking Charge Order in a Kagome Superconductor*, Nature **602**, 245 (2022).

[89] Z. Shan et al., *Muon Spin Relaxation Study of the Layered Kagome Superconductor CsV_3Sb_5*, Phys. Rev. Research **4**, 033145 (2022).

[90] Y.-X. Jiang et al., *Unconventional Chiral Charge Order in Kagome Superconductor KV_3Sb_5*, Nat. Mater. **20**, 1353 (2021).

[91] Z. Guguchia et al., *Tunable Unconventional Kagome Superconductivity in Charge Ordered RbV_3Sb_5 and KV_3Sb_5*, Nat Commun **14**, 153 (2023).

[92] C. Guo et al., *Switchable Chiral Transport in Charge-Ordered Kagome Metal CsV_3Sb_5*, Nature **611**, 461 (2022).

[94] Q. Wu et al., *Simultaneous Formation of Two-Fold Rotation Symmetry with Charge Order in the Kagome Superconductor CsV_3Sb_5 by Optical Polarization Rotation Measurement*, Phys. Rev. B **106**, 205109 (2022).

[96] C. M. Varma, *Non-Fermi-Liquid States and Pairing Instability of a General Model of Copper Oxide Metals*, Phys. Rev. B **55**, 14554 (1997).

[97] M. Kang et al., *Twofold van Hove Singularity and Origin of Charge Order in Topological Kagome Superconductor CsV_3Sb_5*, Nat. Phys. **18**, 301 (2022).

[99] H. Tan, Y. Liu, Z. Wang, and B. Yan, *Charge Density Waves and Electronic Properties of Superconducting Kagome Metals*, Phys. Rev. Lett. **127**, 046401 (2021).

[100] H. Luo et al., *Electronic Nature of Charge Density Wave and Electron-Phonon Coupling in Kagome Superconductor KV_3Sb_5*, Nat Commun **13**, 273 (2022).

[101] R. Tazai, Y. Yamakawa, and H. Kontani, *Drastic Magnetic-Field-Induced Chiral Current Order and Emergent Current-Bond-Field Interplay in Kagome Metal AV_3Sb_5 (A=Cs,Rb,K)*, (2023).

[102] X. Feng, K. Jiang, Z. Wang, and J. Hu, *Chiral Flux Phase in the Kagome Superconductor AV_3Sb_5*, Science Bulletin **66**, 1384 (2021).

[103] H. Li, H. Zhao, B. R. Ortiz, T. Park, M. Ye, L. Balents, Z. Wang, S. D. Wilson, and I. Zeljkovic, *Rotation Symmetry Breaking in the Normal State of a Kagome Superconductor KV_3Sb_5*, Nat. Phys. **18**, 265 (2022).

[104] H. Li, S. Wan, H. Li, Q. Li, Q. Gu, H. Yang, Y. Li, Z. Wang, Y. Yao, and H.-H. Wen, *No Observation of Chiral Flux Current in the Topological Kagome Metal CsV_3Sb_5*, Phys. Rev. B **105**, 045102 (2022).

[105] C. Farhang, J. Wang, B. R. Ortiz, S. D. Wilson, and J. Xia, *Unconventional Optical Rotation in the Charge Ordered State of Kagome Metal CsV_3Sb_5*, (2023).